

# FORMATION AND EVOLUTION OF MASSIVE EARLY-TYPE GALAXIES

---

## Dissertation

PhD thesis

zur Erlangung der Doktorwürde

for the degree of Doctor of natural science

an der Fakultät für Physik

at the Faculty for Physics

der Ludwig-Maximilians-Universität (LMU), München

of the Ludwig-Maximilians-University (LMU) of Munich

vorgelegt von

presented by

**Dipl.-Phys. Ludwig Oser**

aus Darmstadt, Deutschland

from Darmstadt, Germany

München, February 8, 2012



# LUDWIG MAXIMILIANS UNIVERSITY OF MUNICH



Erster Gutachter: Prof. Dr. Andreas Burkert (USM, LMU)  
First advisor

Zweiter Gutachter: Prof. Dr. Jochen Weller (USM, LMU)  
Second advisor

Tag der mündlichen Prüfung: 30.01.2012  
Day of oral exam



*"There is a theory which states that if ever anybody discovers exactly what the Universe is for and why it is here, it will instantly disappear and be replaced by something even more bizarre and inexplicable. There is another theory which states that this has already happened."*

**Douglas Adams**



---

# Zusammenfassung

In dieser Arbeit untersuchen wir, wie massive elliptische Galaxien aus primordialen Dichtefluktuationen entstehen und sich bis zur Gegenwart entwickeln. Hierfür verwenden wir das größte Set an kosmologischen Simulation individueller Galaxien, das bisher berechnet wurde. Die Simulationen beinhalten eine selbstkonsistente Beschreibung der hydrodynamischen Kräfte sowie Kühlung und Heizen durch Strahlung, Sternentstehung und Feedback durch Supernovae. Mit diesem Simulationsaufbau sind wir in der Lage Galaxien mit realistischen Eigenschaften zu erzeugen und es gelingt uns beobachtete Tendenzen der Strukturparameter in lokalen und fernen Galaxien zu reproduzieren.

Wir stellen fest, daß Galaxienentstehung in 2 Phasen abläuft. In einer frühen dissipativen Phase wachsen Galaxien durch in situ Sternentstehung im Zentrum, später gelingt der Aufbau von stellarer Masse primär durch Akkretion kleinerer Systeme. Im Allgemeinen finden wir, daß der Bruchteil der Sterne die in situ in der Galaxie entstanden sind mit zunehmender Gesamtmasse der Galaxie abnimmt und für die räumliche Größe des Systems am heutigen Tag bestimmend ist. Während die dissipative Sternentstehung aus kalten Gasströmen bei hohen Rotverschiebungen zu kompakten Strukturen führt legen sich die später akkretierten Sterne wie eine Hülle um den kompakten Kern und haben einen signifikant größeren Halbmassenradius. Wir beobachten in den Simulationen auch das Phänomen, das von Beobachtern üblicherweise als 'archaeological downsizing' bezeichnet wird. Hierbei haben die massereichsten Galaxien die ältesten Sternpopulationen. Dies ist allerdings nicht im Widerspruch zur  $\Lambda$ CDM Theorie, nachder sich kleine Strukturen zuerst bilden. Denn obwohl die Sterne in den massereichen Galaxien sehr alt sind werden sie erst spät akkretiert und die massiven Galaxien bilden sich tatsächlich als Letztes.

Die Entwicklung der Galaxiengrößen und stellaren Geschwindigkeitsdispersionen kann durch die häufige Verschmelzung mit relativ kleinen Galaxien erklärt werden. Wir beobachten, daß die simulierten Galaxien zunächst ein sehr kleines Ausmaß haben und hohe Geschwindigkeitsdispersionen aufweisen. Das Anwachsen der Halbmassenradien und die Abnahme der stellaren Geschwindigkeitsdispersion - bis beides den heute beobachteten lokalen Relationen folgt - gelingt durch die Akkretion kleiner Strukturen. Die akkretierten Sterne sammeln sich vor allem in den äußeren Regionen der Galaxien an und verursachen so das beobachtete starke Anwachsen der Halbmassenradien. Das Anwachsen der Galaxiengrößen sowie der Abfall der stellare Geschwindigkeitsdispersion folgen den Vorhersagen für kollisionsfreie Galaxienverschmelzungen. Wir stellen fest, daß die stellare Masse typischerweise durch Galaxienverschmelzungen mit einem Massenverhältnis von 1 zu 5 anwächst. Ein maßgeblicher Teil der simulierten Galaxien erlebt keine 'große' ( $> 1 : 5$ ) Galaxienverschmelzung im Zeitraum zwischen einer Rotverschiebung von 2 und dem heutigen Tag, was uns die oft erwähnte Bedeutung von sogenannten 'major merger' für die Entwicklung von elliptischen Galaxien anzweifeln lässt.

Zusätzlich präsentieren wir die erste detaillierte kinematische Analyse kosmologischer Simulation von elliptischen Galaxien. Wir konstruieren 2-dimensionale Abbilder

der stellaren Geschwindigkeiten, der Geschwindigkeitsdispersionen sowie für höhere Momente der Gauss-Hermite Polynome. Wir belegen die aktuelle Beobachtungen, daß elliptische Galaxien oft eine bedeutende Menge an Rotation zeigen. Wir finden dieselbe Vielfalt an kinematischen Eigenschaften wie in den Beobachtungen in den Simulationen wieder, z.B. langsam und schnell rotierende Systeme sowie verstellte oder gegenläufige Rotation. Der Anteil an schnell rotierenden Galaxien nimmt mit zunehmender Galaxienmasse ab. Entgegen den Ergebnissen von idealisierten Simulationen von Galaxienverschmelzungen finden wir keinen Hinweis darauf, daß Galaxienverschmelzungen mit besonders hohen Massenverhältnissen nötig sind um langsam rotierende elliptische Galaxien zu erzeugen. Wir führen ein Beispiel einer langsam rotierenden Galaxie an, die nur aus Galaxienverschmelzungen mit Massenverhältnissen von 1 zu 4 oder kleiner entstanden ist.

Die hier untersuchten Simulationen bilden - wenn man sie mit Halo-Verteilungsmodellen vergleicht - um dem Faktor 2 zu viele Sterne. Dieses Problem wird gewöhnlich als 'overcooling' bezeichnet und ist allgegenwärtig in Simulationen von Galaxienentstehung. Wir planen als nächsten Schritt das hier verwendete Feedback-Modell zu verbessern, sowie weitere Prozesse (z.B. Feedback von superschweren schwarzen Löchern) in die Simulationen einzubauen um diesem Problem entgegenzuwirken.

---

## Summary

In this thesis we study the formation and evolution of massive early-type galaxies out of primordial density fluctuations up to the present day. To accomplish this task we use the largest set of cosmological simulations of individual galaxies performed so far, including a self-consistent treatment of hydrodynamics as well as radiative cooling and heating, star formation and supernovae feedback. With this setup we are able to create galaxies with realistic properties, reproducing trends of structural parameters observed in local and distant galaxies.

We find that galaxy formation is a two-phase process: in an early dissipative phase stellar mass is built up by in situ star formation, later the growth is dominated by the accretion of smaller systems. In general the ratio of accreted to in situ created stars at the present day is increasing with increasing stellar mass and is responsible for the final spatial extend of the system. While the dissipative formation of stars out of cold gaseous streams at high redshifts tend to create compact systems the later accreted stars are forming an envelope around these stellar cores with much larger half-mass radii. We recover the observational phenomenon usually referred to as 'archaeological downsizing' where the most massive galaxies are made out of the oldest stellar populations. This is not in contradiction to the bottom-up formation scenario of  $\Lambda$ CDM since although the stars themselves form early they are accreted late and the most massive galaxies indeed assemble at last.

The evolution of galaxy sizes and stellar velocity dispersions is the result of frequent minor mergers. We find that the simulated galaxies initially are all rather compact with high velocity dispersions. The increase in size and decrease in velocity dispersions - until both follow observed present-day relations - is accomplished by the accretion of smaller systems. The accreted stars settle in the outer regions of the galaxies leading to the strong observed size increase and the evolution of sizes and velocity dispersion follow the predictions for collisionless mergers. We find that stellar mass is accreted on average in minor mergers with a mass fraction of 1:5. A significant amount of the simulated galaxies have no major merger between redshift 2 and the present day which degrades the often discussed importance of major mergers for the evolution of early-type galaxies.

In addition, we present the first detailed kinematically analysis of cosmological simulations of early-type galaxies. We construct two-dimensional maps of the stellar velocities, velocity dispersion as well as higher order Gauss-Hermite moments for all the galaxies presented in this work. We support the recent observation that a large fraction of the early-type galaxies show a significant amount of rotation. We recover the diversity of observed kinematic properties in the simulations with slow and fast rotators as well as misaligned and even retrograde rotation. The fraction of fast rotating galaxies is decreasing with increasing galaxy mass. Contrary to the results obtained from idealized merger simulations we find no evidence for major mergers being necessary for the development of a slowly rotating system. In fact we give an example for a galaxy with diminishing rotational support at the present day that has no major

(> 1 : 4) merger since redshift 2.

The simulations presented here still suffer from the ubiquitous problem of over-cooling and produce stellar masses of galaxies that are roughly too high by a factor of 2 when compared to halo-occupation-distribution models. As a next step, we are planning to improve upon the current feedback prescription as well as the implementation of further feedback processes (e.g. active galactic nuclei) to alleviate this problem.





# Contents

<b>1</b>	<b>Motivation</b>	<b>1</b>
<b>2</b>	<b>Introduction</b>	<b>3</b>
2.1	The Early Universe . . . . .	3
2.2	Dark Matter . . . . .	5
2.3	Structure formation . . . . .	5
<b>3</b>	<b>Theory of Structure Formation</b>	<b>7</b>
3.1	Cosmology . . . . .	7
3.1.1	Friedmann equations . . . . .	7
3.1.2	Hubble constant . . . . .	9
3.1.3	Redshift . . . . .	9
3.2	$\Lambda$ CDM model . . . . .	10
3.3	Jeans Limit . . . . .	11
3.4	Growth of density fluctuations . . . . .	16
3.5	Zeldovich approximation . . . . .	19
3.6	Top-Hat spherical collapse . . . . .	20
<b>4</b>	<b>Numerical Methods</b>	<b>23</b>
4.1	Gravitational N-body Problem . . . . .	23
4.2	Gravitational Softening . . . . .	24
4.3	Tree Codes . . . . .	25
4.4	Smoothed Particle Hydrodynamics . . . . .	26
4.5	Additional Physics . . . . .	28
4.6	Simulations . . . . .	30
4.6.1	The large-scale dark matter simulation . . . . .	30
4.6.2	Refined Simulations . . . . .	32
4.6.3	The baryonic mass budget . . . . .	33

---

<b>5</b>	<b>The Two Phases of Galaxy Formation</b>	<b>37</b>
5.1	The two phases of galaxy formation . . . . .	41
5.2	Galaxy sizes . . . . .	55
5.3	Summary and Discussion . . . . .	55
<b>6</b>	<b>Size and Velocity Dispersion Evolution of massive early-type Galaxies</b>	<b>59</b>
6.1	High resolution simulations of individual galaxy halos . . . . .	62
6.2	Redshift evolution of sizes . . . . .	62
6.3	Redshift evolution of velocity dispersions . . . . .	67
6.4	Stellar Merger histories . . . . .	69
6.5	Conclusion & Discussion . . . . .	73
<b>7</b>	<b>Stellar Kinematics</b>	<b>77</b>
7.1	High-resolution simulations of individual galaxy halos . . . . .	81
7.2	Construction of kinematic maps . . . . .	86
7.3	Fast and slow rotators . . . . .	88
7.4	Conclusions and Discussion . . . . .	95
<b>8</b>	<b>Conclusions &amp; Outlook</b>	<b>101</b>
<b>A</b>	<b>Kinematic maps</b>	<b>105</b>
	<b>Bibliography</b>	<b>115</b>
	<b>Acknowledgements</b>	<b>137</b>
	<b>Erklärung</b>	<b>139</b>

# List of Figures

2.1	Cosmic Microwave Background . . . . .	4
3.1	Cosmological composition . . . . .	12
3.2	Density fluctuations . . . . .	18
4.1	Dark matter mass function . . . . .	31
4.2	Spin parameter distribution . . . . .	32
4.3	Initial Conditions . . . . .	34
4.4	Baryon conversion efficiency . . . . .	35
5.1	Stellar origin diagram for M0125 . . . . .	41
5.2	Stellar origin diagram for M1646 . . . . .	43
5.3	Stacked stellar origin diagrams . . . . .	44
5.4	Stellar mass assembly histories . . . . .	45
5.5	Cold mode accretion . . . . .	46
5.6	Star formation histories . . . . .	47
5.7	Dependencies on fraction of in-situ created stars . . . . .	48
5.8	Mean stellar ages . . . . .	51
5.9	Assembly time . . . . .	52
5.10	Galaxy sizes . . . . .	54
6.1	Size evolution . . . . .	63
6.2	Size dependence on fraction of in-situ created stars . . . . .	64
6.3	Stellar mass profiles . . . . .	65
6.4	Velocity dispersion evolution . . . . .	68
6.5	Size growth since $z=2$ . . . . .	70
6.6	Merger ratios . . . . .	71
7.1	Merger Tree comparison . . . . .	79
7.2	Kinematic maps . . . . .	82
7.3	$\lambda_R$ profiles . . . . .	89
7.4	Stellar mass vs. $\lambda_R$ . . . . .	91

---

7.5	Ellipticities vs. $\lambda_R$ . . . . .	92
7.6	Dependence of $\lambda_R$ on the fraction of in situ created stars . . . . .	93
7.7	Spin parameter of the dark matter halo vs. $\lambda_R$ . . . . .	94
7.8	Maximum merger ratio vs. $\lambda_R$ . . . . .	96
7.9	Evolution of the specific angular momentum of M0175 . . . . .	97
7.10	Evolution of the specific angular momentum of M0408 . . . . .	98
8.1	Metal map of M0329 . . . . .	104
A.1	Kinematic maps: M0040 - M0125 . . . . .	106
A.2	Kinematic maps: M0162 - M0209 . . . . .	107
A.3	Kinematic maps: M0215 - M0300 . . . . .	108
A.4	Kinematic maps: M0329 - M0549 . . . . .	109
A.5	Kinematic maps: M0616 - M0908 . . . . .	110
A.6	Kinematic maps: M0948 - M1071 . . . . .	111
A.7	Kinematic maps: M1091 - M1646 . . . . .	112
A.8	Kinematic maps: M1859 - M2665 . . . . .	113

## MOTIVATION

The cover page shows the arguably most famous picture in modern astronomy: The Hubble Deep Field (Williams et al. 1996). It was assembled out of pictures taken over 10 consecutive days with 4 different broadband filters. The Hubble Space Telescope was pointed at a blank of the sky in Ursa Major and revealed approximately 3000 galaxies which are typically 5 to 10 billion light years away. But it does not matter in which direction one is looking. More recent observations (York et al. 2000; Colless et al. 2001) have shown that on these very large scales our Universe is rather homogeneous and that space is full of these bright objects. But they only represent the luminous tip of the iceberg in a Universe that is primarily made of some unknown 'dark matter' and an even less understood form of 'dark energy'. Galaxies are believed to form in the high-density peaks of the overall mass distribution. They are the localities in which stars are born and evolving and contain most of the visible stars in the Universe rendering the number density of stars within galaxies about  $10^7$  times higher than the mean number density of stars in the Universe. Therefore they are visible over such large distances allowing us to study our Universe over cosmological scales, which is why understanding how galaxies come into existence and how they are evolving are important, yet challenging issues in modern cosmology. Even the shortest timescales involved in galaxy formation and evolution are much longer than a human lifetime making these processes impossible to be observed directly. However, due to the finiteness of the speed of light we observe our Universe at different stages of development depending on the distance of the objects that are detected.

In comparing the properties of galaxies at different distances and therefore different ages of the Universe astronomers are trying to infer how galaxies form and evolve at least in a statistical sense. Although galaxies are unique in the sense that no two are alike, they follow some intriguingly tight scaling relations leaving some constraints on galaxy evolution models that they must be able to reproduce in order to be successful. For obvious reasons it is difficult to test those models empirically which sets astronomy apart from most other areas of experimental physics. One successful method to study the evolution of galaxies are numerical simulations where galaxies form as the conse-

quence of (relatively) well-known physics out of cosmological initial conditions. This, however, is a problem of formidable complexity since the physical processes involved cover some 23 orders of magnitude from the scale of the Universe itself down to the scale of individual stars. Therefore some simplifications and numerical techniques have to be taken into account to simulate the evolution of galaxies in reasonable computation time. With increasingly powerful computers at our hand ever more accurate simulations are being performed and numerical simulations have been proven useful in answering open questions in modern astronomy, and some of them we are trying to tackle within this work:

- How do massive galaxies accumulate their stellar mass? How does the fraction of in-situ star formation to accreted stellar mass vary? Why do the most massive galaxies have the oldest mean stellar ages in a hierarchical Universe?
- How do the structural properties of massive galaxies evolve with time, and why? What is the dominant mode of accretion for stellar mass growth?
- What are the kinematical properties of massive galaxies at the present day? In what way are they set by the formation history?

To investigate these questions we performed the largest set of cosmological zoom-in simulations performed so far.

This work is organized as follows: we start with an introduction in chapter 2. In chapter 3 we give an overview over the theory of structure formation. The simulation code used to carry out the calculations as well as the initial conditions are explained in chapter 4. In chapter 5 we discuss the two phases of galaxy formation. The evolution of structural properties of massive galaxies is presented in chapter 6 followed by a detailed study of the kinematics in chapter 7. We summarize and discuss our findings in chapter 8 and give an outlook to future work.

# INTRODUCTION

## 2.1 The Early Universe

It is commonly assumed that 13.7 billion years ago our Universe developed out of a tremendously hot and dense state called the *Big Bang* (Spergel et al. 2007). It is believed, that the Universe experienced an epoch of accelerated expansion  $10^{-35}s$  shortly after the Big Bang. During this so called *Inflation period* it expanded by a factor of  $10^{50}$  within  $10^{-33}s$ , smoothing out any irregularities and thereby creating a flat and homogeneous Universe (Guth 1981). Additionally, random quantum fluctuations were blown-up by inflation into macroscopic inhomogeneities in the Universe. These primeval density perturbations would be the seed for structure formation and eventually evolve into the structures that are seen today like galaxies and clusters. The rapid expansion caused an extreme drop of temperature, however the Universe is expected to be re-heated back to a temperature of  $T \sim 10^{28}K$  due to the conversion of the energy of the inflaton field into heat.

After inflation the Universe continued to expand at a normal rate. It eventually became cold enough for baryons to form, with a slight asymmetry in numbers of baryon and antibaryons. After the annihilation of the baryon-antibaryon pairs we are left with a Universe composed mainly of non-baryonic dark matter (see ch. 2.2) and baryonic matter (protons, neutrons, electrons, positrons<sup>1</sup>) in thermal equilibrium with the radiation (neutrinos and photons) through scattering reactions. 10 seconds after the Big Bang when the electron-positron pairs are annihilated the energy content of the Universe is dominated by the density of photons and neutrinos. The density of radiation scales as  $\rho_{\text{rad}} \propto a^{-4}$  where  $a$  is the cosmological scale factor whereas the density of matter scales as  $\rho_{\text{mat}} \propto a^{-3}$ . The additional factor of  $a^{-1}$  is due to the *cosmological redshift* causing the wavelength of the photons to increase and therefore lowering their energy. At a redshift of  $z_{\text{eq}} \sim 3500$  which corresponds to  $t_{\text{eq}} \sim 100\,000$  yrs the density of radiation and matter become comparable and the Universe enters the matter

---

<sup>1</sup>Although electrons and leptons are leptons it is common practice to include them to the baryonic matter in astrophysics

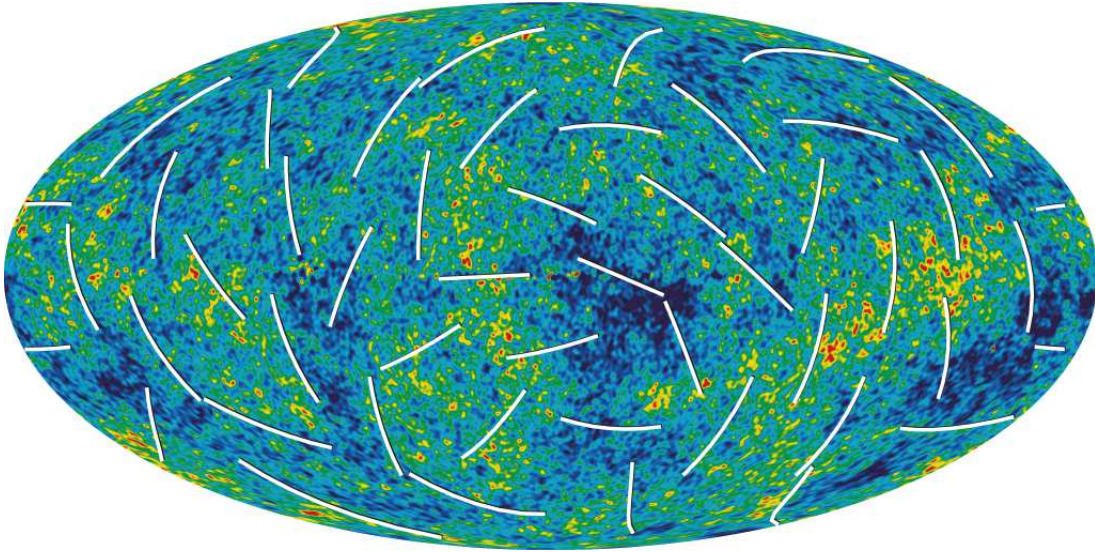


**Figure 2.1:** The cosmic microwave background as observed by the WMAP mission (Spergel et al. 2003, 2007; Komatsu et al. 2011). Colors indicate warmer (red) and cooler (blue) areas, the white bars show the polarization direction of the photons. The CMB provides us with information about the temperature fluctuations at  $z \sim 1100$  that are of the order of  $\Delta T/T \sim 10^{-5}$ . Today the observed spectrum of the CMB resembles that of a black body with a characteristic temperature of  $T = 2.725 \pm 0.002$  K (source NASA).

dominated era.

As the Universe continued to expand the temperature kept decreasing as well, and at a redshift of  $z_{dec} \sim 1100$  or  $t_{dec} \sim 380\,000$  yrs the Universe was for the very first time cold enough for protons and electrons to recombine (actually they have never been combined before, still this is oddly called *recombination*). At a temperature of  $T \sim 4000$  K the neutral fraction was sufficiently high for the photons to decouple from the matter at the so called *epoch of last-scattering*. The photons emitted during this recombination can still be seen today as the *cosmic microwave background* (CMB) providing us with a snapshot of the temperature variations of the Universe at  $z \sim 1100$  (see Fig. 2.1). The spectrum of the CMB today coincides with extreme precision to a black-body spectrum with a characteristic temperature of  $T = 2.725 \pm 0.002$  K, with very small fluctuations of the order of few parts in  $\Delta T/T \sim 10^{-5}$ . The variations in the temperature are closely linked to fluctuations in density at  $z \sim 1100$ , therefore the CMB provides us with valuable information about the early structure of our universe.

## 2.2 Dark Matter

Nearly everything we know about our surrounding universe we have learned from observing electromagnetic radiation. In the beginning of observational astronomy we relied on optical photons we received from stars or galaxies, but in the last century we started to detect radio waves from cold neutral hydrogen gas as well as X-ray photons from hot ionized gas and so forth. Alas, there is no reason why every type of matter should emit radiation in some way. This matter would in fact be invisible to our current observational instruments. “Thus we use the term **Dark Matter** to denote any form of matter whose existence is inferred solely from its gravitational effects.” (Binney & Tremaine 1987)

The existence of Dark Matter is commonly accepted, the question remains what form it takes. Dark Matter could consist of ordinary matter that does not emit light, e.g. stars that do not reach the mass limit for hydrogen burning. But it is more probably, that it is made of a still unknown elementary particle, that does not interact electromagnetically and is therefore unable to radiate photons of any kind. These particles could be non-relativistic **w**eakly **i**nteracting **m**assive **p**articles (WIMPs). The predictions of primordial nucleosynthesis disprove the former theory, that baryonic matter could make up for the missing mass, but a promising candidate for the latter one has not been found yet, either. Particle Physics and especially Supersymmetry are predicting new yet undiscovered particles which could be the origin for dark matter, e.g. the neutralino or the axion (see e.g. Peacock 1999).

Nonetheless, Dark Matter remains a crucial aspect in present cosmological models and it is needed to describe observed properties of galaxies and galaxy clusters, and even if one cannot definitely say what Dark Matter is made of, the evidence for its existence is compelling. For example the first evidence of dark matter was found by the Swiss astronomer Fritz Zwicky in 1933. Zwicky had been measuring radial velocities of seven galaxies belonging to the Coma cluster. He interpreted the dispersion of radial velocities as a measure of the kinetic energy per unit mass, together with a rough estimate of the cluster radius he could calculate the total mass of the cluster using the virial theorem. When he compared the mass-to-light ratio measured in this way to those yielded by rotation curves of nearby spirals, he found that the former exceeded the latter by a factor of a least 400. He inferred from this result, that nearly all of the cluster mass takes the form of some invisible or dark matter that can solely interact with ordinary, baryonic matter through gravity. Today, Zwicky’s proposition remains the common explanation for the observed flatness of rotation curves at large radii and the existence of dark matter is nowadays hardly ever doubted.

## 2.3 Structure formation

In the currently most successful theories, all structure in the Universe is forming out of tiny primordial inhomogeneities created by quantum fluctuations that have been blown up during an rapid phase of exponential expansion, called inflation (Mo et al.

2010). The overdense regions will grow as a result of gravitational attraction: at first the collapse of dark matter will take place, later on the baryonic mass condensates in the potential wells created by dark matter. Self-gravity causes then overdense regions to collapse until at some point virial equilibrium is reached. The *Jeans mass* (see section 3.3) represents the limiting mass for regions able to collapse. Before matter-radiation equality the Jeans Mass for baryonic density fluctuations was very large ( $\sim 10^{16}M_{\odot}$ ) which in turn inhibited structure formation. This was due to the major contribution to the pressure by Thomson scattering of photons with free electrons, therefore baryonic structure formation could only begin after recombination at  $z \sim 1100$  when the Temperature of Universe had dropped to  $T \sim 10^4 K$ . However, we will see in section 3.4 that the density contrast observed in the CMB is too small to explain the present day large overdensities. This means we need to include *non-baryonic dark matter* in our model so that structure formation can begin right after matter-radiation equality, which is another strong indication for the existence of non-baryonic dark matter (see section 2.2). The dark matter would not interact with the photons and could therefore begin to collapse before recombination, baryonic matter could then subsequently fall into the density enhancements created by dark matter.

In contrast to the Hot-Dark-Matter model, the standard CDM model predicts the first structures to collapse in low mass halos with low virial temperatures ( $T \lesssim 10^4 K$ ). Therefore it favors *hierarchical* structure formation where structure forms *bottom-up*, i.e. small structures form first and large structures form by merging.

Besides baryonic and dark matter there is a third energy component in the Universe. This component is due to the cosmological constant  $\Lambda$  and can be thought of the energy density of the vacuum itself. Since there is no real understanding of the source of this form of energy so far, it is commonly called *dark energy*. Unlike matter densities the dark energy will not get diluted by cosmic expansion ( $\rho_{\Lambda} \propto a^0$ ) and will as a result become the dominant form of energy in the late time of our Universe. This happened for our universe at  $z \sim 0.7$  which was about 5 billion years ago and dark energy is currently re-accelerating the expansion of the Universe. In turn the contribution of the cosmological constant will increase even more leading to an even faster accelerated expansion in the future.

# THEORY OF STRUCTURE FORMATION

In this chapter we will summarize the most important aspects of theoretical structure formation in a  $\Lambda$ CDM (see Section 2.3 and 3.2) universe. For a more complete description we refer the reader to the literature (e.g. Peacock 1999). Modern cosmology is based on the cosmic principle, which states that the Universe is spatially homogeneous and isotropic on large scales and Einstein's theory of general relativity which relates the structure of space-time to the mass distribution in the Universe. In a perfectly homogeneous universe structure formation would be impossible. The inhomogeneities needed, are assumed to arise from quantum fluctuations at a very early epoch when general relativity breaks down due to the Universe being hot and dense enough for quantum effects to be important. We are currently unable to predict the initial conditions for galaxy formation from first principles and the parameters determining structure formation have to be set by observations, e.g. the fluctuations in the microwave background and the present-day clustering of galaxies. Under the influence of gravity small overdensities will grow in mass and size until  $\delta\rho/\rho \sim 1$ , when the evolution will decouple from the expansion of the Universe. At that moment, called turn-around, the structure will have its largest spatial extent and will start the non-linear collapse, which in general not be described analytically.

## 3.1 Cosmology

### 3.1.1 Friedmann equations

Albert Einstein laid the foundation for modern cosmology in 1915 in presenting his *theory of General Relativity* which describes how space-time is distorted by the presence of matter and how matter moves along trajectories in curved space-time. General Relativity relates the stress-energy tensor to the geometrical properties by *Einstein's equation*:

$$R_{\mu\nu} - \frac{1}{2}g_{\mu\nu}R = \frac{8\pi GT_{\mu\nu}}{c^4} + \Lambda g_{\mu\nu}, \quad (3.1)$$

where

- $R_{\mu\nu}$  is the Ricci tensor, a contraction of the Riemann curvature tensor by the metric tensor  $g_{\mu\nu}$
- $R = g^{\mu\nu}R_{\mu\nu}$  is the Ricci scalar
- $T_{\mu\nu}$  is the stress-energy tensor, responsible for space-time curvature
- $\Lambda$  is a universal cosmological constant, originally introduced by Einstein to allow for a static solution

Assuming that the Universe is a perfect fluid (*homogeneous* on large scales, *isotropic* and with *no shear stress*) the Friedmann-Robertson-Walker metric provides an exact solution to the Einstein field equations of general relativity. It is the most general space-time metric that describes an expanding Universe filled with isotropic and homogeneous matter:

$$ds^2 = -c^2 dt^2 + a^2(t) \left[ \frac{dr^2}{1 - kr^2} + r^2 d\theta^2 + r^2 \sin^2 \theta d\phi^2 \right] \quad (3.2)$$

where  $a(t)$  is the scale factor of the Universe relating proper distance  $l$  to comoving distance  $r$  via

$$l = a(t)r \quad (3.3)$$

and the free parameter  $k$  is describing the global curvature of the Universe. For a vanishing cosmological constant  $\Lambda$  the global curvature can either be positive (closed)  $k = +1$ , (flat)  $k = 0$  or negative (open)  $k = -1$ . The assumptions of isotropy and homogeneity result in enormous simplifications of Einstein's field equations leading to the *Friedmann equations*

$$\frac{\ddot{a}}{a} = -\frac{4\pi G}{3}(\rho + 3\frac{p}{c^2}) + \frac{\Lambda}{3}, \quad (3.4)$$

$$\left(\frac{\dot{a}}{a}\right)^2 = \frac{8\pi G}{3}\rho - k\frac{c^2}{a^2} + \frac{\Lambda}{3} \quad (3.5)$$

that govern the expansion of space. If we combine all contributions to  $\rho$ , i.e. those of matter as well as vacuum, we obtain a direct connection between the density of the Universe and its global geometry:

$$\frac{kc^2}{a^2} = \frac{\dot{a}^2}{a^2} \left[ \frac{\rho}{3H^2/8\pi G} - 1 \right], \quad (3.6)$$

where  $H$  is the Hubble constant and  $G$  is the gravitational constant. We define a critical density as

$$\rho_c \equiv \frac{3H^2}{8\pi G}; \quad \Omega \equiv \frac{\rho}{\rho_c} = \frac{8\pi G\rho}{3H^2}; \quad (3.7)$$

$$\rho_c(z = 0) = 1.88 \times 10^{-26} h^2 \text{ kg m}^{-3}. \quad (3.8)$$

Inserting this into equation (3.6) yields

$$\frac{kc^2}{a^2} = H^2(\Omega - 1) \quad (3.9)$$

$$\text{for } \rho = \rho_c \rightarrow \Omega = \Omega_{\text{matter}} + \Omega_{\Lambda} = 1 \Rightarrow k = 0 \quad (3.10)$$

We see if the density of the Universe is equal to the *critical density* then the Universe is flat. For larger densities ( $\Omega > 1$ ) it would be *spatially closed*, whereas for lower densities ( $\Omega < 1$ ) it would be *spatially open*.

### 3.1.2 Hubble constant

The expansion of our Universe was discovered by Hubble in 1929. He observed that galaxies in all directions were receding from the Milky Way, with increasingly larger velocities for larger distances. The famous *Hubble law* is the result of that observations:

$$v = Hl, \quad (3.11)$$

where  $v$  is the recession velocity,  $l$  is the proper distance to the object and  $H$  is the Hubble constant. Its present day value is conveniently parametrized with the dimensionless parameter  $h$ .

$$H_0 = 100 h \text{ kms}^{-1} \text{ Mpc}^{-1} \quad (3.12)$$

Using (3.3) we can relate the Hubble constant to the expansion factor  $a(t)$

$$v(t) = \frac{dl}{dt} = r\dot{a}(t) = \frac{\dot{a}}{a}l \Rightarrow H(t) = \frac{\dot{a}(t)}{a(t)} \quad (3.13)$$

Note that unlike what the name is implying the Hubble constant is time-dependent. The dependence of  $H$  on the expansion factor in a matter-dominated, flat universe is given by

$$H^2(a) = H_0^2[\Omega_{\Lambda} + \Omega_m a^{-3} + \Omega_r a^{-4} - (\Omega - 1)a^{-2}] \quad (3.14)$$

where  $\Omega_{\Lambda}$ ,  $\Omega_m$  and  $\Omega_r$  are the contributions to the overall energy density  $\Omega$  due to the cosmological constant, matter and radiation. In the matter dominated phase we neglect the contribution of radiation, and for a flat universe  $\Omega - 1 = 0$ . The present day best fit value for the Hubble constant is  $h = 0.73_{-0.03}^{+0.03}$  (Spergel et al. 2007).

### 3.1.3 Redshift

The redshift of an object is defined as

$$z \equiv \frac{\lambda_0 - \lambda_e}{\lambda_e} \quad (3.15)$$

where  $\lambda_0$  is the observed wavelength at a time  $t_0$  and  $\lambda_e$  is the emitted wavelength at some earlier time  $t_e$ . This redshift is not due to a Doppler shift, like Hubble interpreted, but is a result of cosmic expansion. The relation between expansion factor  $a(t)$  and redshift  $z$  will be derived in the following.

Consider a wave package of frequency  $\nu_e$  emitted between cosmic times  $t_e$  and  $t_e + \Delta t_e$ . This package is received by the observer in the interval  $t_0$  to  $t_0 + \Delta t_0$ . Radiation travels along a null geodesic from the source to the observer, i.e.  $ds^2 = 0$ . If we further consider radial propagation ( $d\Theta = 0$ ,  $d\Phi = 0$ ) integration of (3.2) yields:

$$\int_{t_e}^{t_0} \frac{cdt}{a(t)} = \int_0^r \frac{dr}{\sqrt{1 - kr^2}} \quad (3.16)$$

The end of the wave package must travel the same distance in units of comoving distance

$$\int_{t_e + \Delta t_e}^{t_0 + \Delta t_0} \frac{cdt}{a(t)} = \int_0^r \frac{dr}{\sqrt{1 - kr^2}}. \quad (3.17)$$

For small  $\Delta t_e$  and  $\Delta t_0$  we can combine the left hand sides of the last two equations to

$$\int_{t_e}^{t_0} \frac{cdt}{a(t)} + \frac{c\Delta t_0}{a(t_0)} - \frac{c\Delta t_e}{a(t_e)} = \int_{t_e}^{t_0} \frac{cdt}{a(t)}. \quad (3.18)$$

Since  $a(t_0) = 1$ , we find that

$$\Delta t_0 = \frac{\Delta t_e}{a(t_e)}. \quad (3.19)$$

Using  $\Delta t_e = \nu_e^{-1}$ ,  $\Delta t_0 = \nu_0^{-1}$  and equation (3.15) we arrive finally at

$$a(t) = \frac{1}{1 + z}. \quad (3.20)$$

Thus the redshift of a galaxy tells us directly how much the Universe has expanded since the light we now observe was emitted.

## 3.2 $\Lambda$ CDM model

Throughout this work we assume the  $\Lambda$ -Cold Dark Matter concordance model to describe a flat  $\Lambda$ -dominated universe seeded by nearly scale-invariant adiabatic Gaussian fluctuations. It is described by six primary parameters:

- **Hubble Constant  $H_0$**

Like mentioned in section (3.1.2) the Hubble constant measures the local expansion rate of the Universe. Recent measurements of standard candles (e.g. SNIa) predict an increasing expansion rate (Riess et al. 1998; Perlmutter et al. 1999).

- **matter density**  $\Omega_m h^2$   
The matter density indicates the contribution of matter, dark matter as well as baryonic, to the overall energy density of the Universe.
- **baryon density**  $\Omega_b h^2$   
Baryon density quantifies the part of the matter density that is due to baryonic matter  $\Omega_m = \Omega_b + \Omega_{dm}$ .
- **amplitude of fluctuations**  $\sigma_8$   
The  $\sigma_8$  parameter represents the amplitude of fluctuations within spheres of  $8 h^{-1}\text{Mpc}$  radius as predicted by linear theory when extrapolated to the present day. The actual value of  $\sigma_8$  is of significant interest since it corresponds to the mass fluctuations from which a rich cluster forms.
- **optical depths**  $\tau$   
This parameter specifies the optical depth to electron scattering to the last scattering surface, it provides information about the reionization history of the Universe.
- **slope for the scalar perturbation spectrum**  $n_s$   
The parameter  $n_s$  stands for the slope of the power spectrum of density fluctuations. A value of  $n_s = 1.0$  would mean that the fluctuations are totally scale-invariant. The observations of the CMB (Spergel et al. 2003, 2007; Komatsu et al. 2010) validate the predictions of inflationary models that  $n_s$  is close to but not exactly 1.0.

The values for these parameters are obtained through the combination of the results of various astronomical surveys. E.g. The large-scale measurements of the Cosmic Microwave Background by the *Wilkinson Microwave Anisotropy Probe* (WMAP) (Spergel et al. 2003, 2007; Komatsu et al. 2010), small-scale CMB measurements, analysis of large-scale galaxy clustering, large samples of high redshift supernovae, analysis of weak lensing data, number counts of galaxy clusters, small-scale clustering of Ly $\alpha$  forest and measurements of the local expansion rate conducted by the *Hubble Space Telescope* (HST). The present day composition of the Universe as well as the contributions of the different forms of matter at the epoch of recombination are depicted in Fig. 3.1.

### 3.3 Jeans Limit

In the following section we want to discuss the properties of density fluctuations that can grow by gravitational attraction. Therefore we examine the evolution of adiabatic perturbations in the linear regime, i.e. the amplitude of the density fluctuations are smaller or at most comparable to the mean density, for a flat Universe with a dominant non-relativistic CDM contribution. The cosmological constant  $\Lambda$  is neglected in the following. For a detailed analysis see e.g. Peacock (1999).

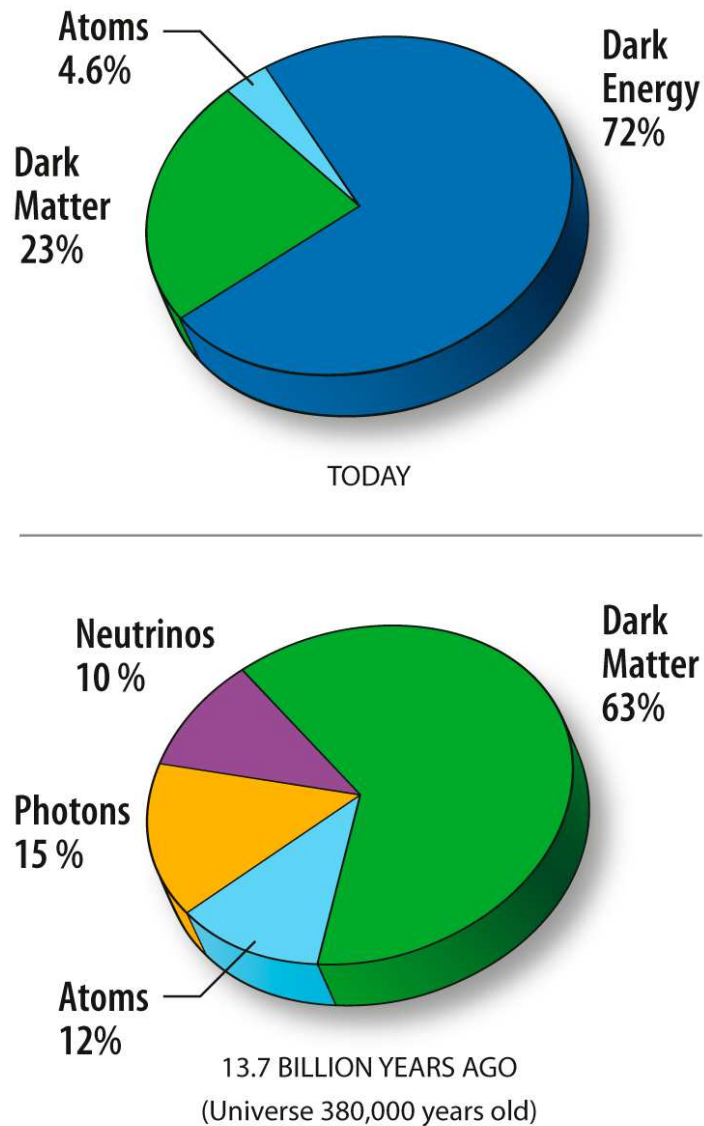


**Figure 3.1:** Illustrating the contributions to the energy density of the Universe as predicted by the  $\Lambda$ CDM concordance model at the present day (top panel) and at the epoch of last scattering (bottom panel). The different energy densities add up to be equal to the critical density making the global geometry of the Universe flat (Source: NASA)

We start with the Euler-Lagrange equations of hydrodynamics:

$$\text{Euler equation} \quad \frac{D\tilde{v}}{Dt} = -\frac{\vec{\nabla}p}{\rho} - \vec{\nabla}\Phi, \quad (3.21)$$

$$\text{Equation of continuity} \quad \frac{D\rho}{Dt} = -\rho\vec{\nabla}\cdot\vec{v}, \quad (3.22)$$

$$\text{Poisson equation} \quad \nabla^2\Phi = 4\pi G\rho, \quad (3.23)$$

where  $D/Dt = \partial/\partial t + \vec{v}\cdot\vec{\nabla}$  is the usual convective derivative,  $\rho(x, t)$  is the density,  $\vec{v}(x, t)$  is the velocity field,  $p(x, t)$  is the pressure and  $\Phi(x, t)$  is the gravitational potential.

We assume that we know the equilibrium solution for the perfect homogeneous case (subscript 0)

$$\frac{d\rho_0}{dt} = -\rho_0(\vec{\nabla}\vec{v}_0), \quad \frac{d\vec{v}_0}{dt} = -\frac{1}{\rho_0}\vec{\nabla}p_0 - \vec{\nabla}\Phi_0, \quad \nabla^2\Phi_0 = 4\pi G\rho_0.$$

This equilibrium solution is now perturbed by small quantities in all variables

$$\vec{v} = \vec{v}_0 + \delta\vec{v}, \quad \rho = \rho_0 + \delta\rho, \quad p = p_0 + \delta p, \quad \Phi = \Phi_0 + \delta\Phi.$$

For sufficiently small perturbations we can neglect terms containing products of perturbations, thus we get after inserting into the hydrodynamic equations and subtracting the equilibrium solution:

$$\frac{d}{dt}\delta\vec{v} = -\frac{\vec{\nabla}\delta p}{\rho_0} - \vec{\nabla}\delta\Phi - (\delta\vec{v}\cdot\vec{\nabla})\vec{v}_0, \quad (3.24)$$

$$\frac{d}{dt}\delta = -\vec{\nabla}\cdot\delta\vec{v}, \quad (3.25)$$

$$\nabla^2\delta\Phi = 4\pi G\rho_0\delta, \quad (3.26)$$

$$\text{assuming that } \vec{\nabla}\rho_0 = 0 \text{ and } \vec{\nabla}p_0 = 0,$$

where

$$\delta \equiv \frac{\delta\rho}{\rho_0} \quad \text{and}$$

$$\frac{d}{dt} \equiv \frac{\partial}{\partial t} + \vec{v}_0\cdot\vec{\nabla}$$

the time derivative for an observer comoving with the unperturbed expansion of the universe

As the universe is expanding the equilibrium solution is time dependent. The relation between proper distance  $x$  and comoving distance  $r$  is

$$\vec{x}(t) = a(t) \cdot \vec{r}(t)$$

. Therefore we get

$$\vec{v} = \frac{\delta \vec{x}}{\delta t} = \dot{a}(t)\vec{r}(t) + a(t)\dot{\vec{r}}(t) = \frac{\dot{a}(t)}{a(t)}\vec{x}(t) + a(t)\vec{u}(t) = H\vec{x} + \delta\vec{v} \quad (3.27)$$

where the term  $\frac{\dot{a}(t)}{a(t)}\vec{x}(t)$  is representing the Hubble expansion and the term  $a(t)\vec{u}(t)$  is the peculiar velocity. Inserting into the Euler equation yields

$$\frac{d(a\vec{u})}{t} = -\frac{\vec{\nabla}\delta p}{\rho_0} - \vec{\nabla}\delta\Phi - (a\vec{u}\vec{\nabla}) \cdot a\vec{r} \quad (3.28)$$

With

$$\nabla_x = \frac{\partial}{\partial x} = \left( \frac{\delta}{a\delta r + r\delta a} \right)_{t=const} = \frac{1}{a} \frac{\delta}{\delta r} = \frac{1}{a} \nabla_r$$

the last term becomes

$$(a\vec{u}\vec{\nabla})\dot{a}\vec{r} = (a\vec{u}\frac{1}{a}\vec{\nabla}_r)\dot{a}\vec{u} = \vec{u}\vec{r}\vec{\nabla}_r\dot{a} + \vec{u}\dot{a}\vec{\nabla}_r\vec{r} = \vec{u}\dot{a}$$

We thereby receive Euler's equation in comoving coordinates

$$a\frac{d\vec{u}}{dt} + 2\dot{a}\vec{u} = -\frac{1}{a\rho_0}\vec{\nabla}_r\delta p - \frac{1}{a}\vec{\nabla}_r\delta\Phi. \quad (3.29)$$

Using

$$\vec{\nabla}\delta\vec{v} = \frac{1}{a}\vec{\nabla}_r(a\vec{u}) = \vec{\nabla}_r\vec{u}$$

we obtain the continuity equation in comoving coordinates

$$\frac{d}{dt}\delta = -\vec{\nabla}_r\vec{u}. \quad (3.30)$$

To eliminate the peculiar velocities we take the comoving divergence of Euler's equation and the time derivative of the continuity equation

$$\vec{\nabla}_r\dot{\vec{u}} + 2\frac{\dot{a}}{a}\vec{\nabla}_r\vec{u} = -\frac{1}{a^2\rho_0}\nabla_r^2\delta p - \frac{1}{a^2}\nabla^2\delta\Phi, \quad (3.31)$$

$$\frac{d^2}{dt^2}\delta = -\vec{\nabla}_r\dot{\vec{u}} \quad (3.32)$$

Furthermore, we assumed that the perturbations are adiabatic, i.e. perturbations in pressure and density are related via the sound speed:

$$\delta p = c_s^2\delta\rho \quad (3.33)$$

together with (3.26) we then obtain a wave equation for the density fluctuations

$$\boxed{\frac{d^2\delta}{dt^2} + 2\frac{\dot{a}}{a}\frac{d\delta}{dt} = \frac{c_s^2}{a^2}\nabla_r^2\delta + 4\pi G\rho_0\delta} \quad (3.34)$$

This equation describes the evolution of small density fluctuations in a perfect fluid in an expanding (or contracting) universe without a cosmological constant. Any solution can be expressed by its Fourier transform, i.e. by a superposition of plane waves:

$$\delta(r, t) = \sum_k \delta_k(t) e^{ik_r r}, \quad (3.35)$$

with the inverse

$$\delta_k(t) = \frac{1}{V} \int \delta(r, t) e^{-ik_r r} d^3r. \quad (3.36)$$

In the linear regime of fluctuations, each wave-component evolves independently and thus we can write:

$$\frac{d^2\delta_k}{dt^2} + 2\frac{\dot{a}}{a}\frac{d\delta_k}{dt} = (4\pi G\rho_0 - c_s^2 k^2)\delta_k \quad \text{with } k_r^2 = a^2 k^2. \quad (3.37)$$

For a non-expanding universe ( $\dot{a} = 0$ ) we can solve this immediately with the Ansatz

$$\delta_k(t) = \delta_{\kappa,0} e^{-i\omega t} \quad (3.38)$$

and obtain the dispersion relation

$$\omega^2 = c_s^2 k^2 - 4\pi G\rho_0. \quad (3.39)$$

This means we have an oscillating solution if the right hand side is positive and an exponentially growing (or decaying) solution if it's negative. For the latter case, the gravitational attraction is stronger than the pressure when

$$4\pi G\rho_0 > c_s^2 k^2 \quad (\text{Jeans criterion}). \quad (3.40)$$

We can describe this as well in terms of a critical length scale, the so called *Jeans length*

$$\lambda > \lambda_j = \frac{2\pi}{k_j} = c_s \left( \frac{\pi}{G\rho_0} \right)^{1/2}. \quad (3.41)$$

This length defines the limit between standing sound waves that have a shorter wavelength than  $\lambda_j$  and the long-wavelength fluctuations that can grow through gravitational attraction. In an expanding universe the Jeans-length is time-dependent, though, i.e. a given perturbation may switch between periods of growth and stasis.

The corresponding *Jeans Mass* of a fluctuations able to collapse is

$$M_J = \frac{4\pi}{3}\rho_0\lambda_j^3 = \frac{4\pi^{5/2}}{3G^{3/2}}\frac{c_s^3}{\rho_0^{1/2}}. \quad (3.42)$$

### 3.4 Growth of density fluctuations

In this section we want to discuss how primeval density fluctuations could form structures through gravitational attraction in an expanding universe. From observation of the CMB we know that the Universe at  $z \sim 1100$  is rather homogeneous ( $\Delta T/T \sim 10^{-5}$ ), so how could superclusters, clusters and galaxies that correspond to overdensities ranging from 10 for superclusters to  $10^6$  for galaxies develop?

As we are only interested in structures that actually grow we just regard fluctuations that are much larger than the Jeans length, i.e.  $4\pi G\rho_0 \gg c_s^2 k^2$ . Equation (3.34) then simplifies to:

$$\frac{d^2\delta_k}{dt^2} + 2\frac{\dot{a}}{a}\frac{d\delta_k}{dt} = 4\pi G\rho_0\delta_k. \quad (3.43)$$

We want to solve this for a matter dominated universe for two limiting cases. Where  $a(t)$  is given by the solution of the Friedmann equations:

$$\begin{array}{llll} \text{case 1:} & \Omega_m = 1 & \Lambda = 0 : & a = \left(\frac{3}{2}H_0t\right)^{2/3} \\ \text{case 2:} & \Omega_m \rightarrow 0 & \Lambda = 0 : & a = H_0t. \end{array}$$

Together with the scaling relation  $t \propto a^{2/3}$  for the matter-dominated phase we obtain the following wave equation for case 1:

$$\frac{d^2\delta_k}{dt^2} + \frac{4}{3t}\frac{d\delta_k}{dt} - \frac{2}{3t^2}\delta_k = 0 \quad (\Omega = 1, \Lambda = 0) \quad (3.44)$$

and for case 2:

$$\frac{d^2\delta_k}{dt^2} + \frac{2}{t}\frac{d\delta_k}{dt} = 0 \quad (\Omega \rightarrow 0, \Lambda = 0). \quad (3.45)$$

This two equations can both be solved with the Ansatz  $\delta_k = at^n$ , the growing mode solutions are

$$\boxed{\begin{array}{ll} \delta_k^+ \propto t^{2/3} \propto a \propto (1+z)^{-1} & (\Omega = 1, \Lambda = 0) \\ \delta_k^+ = \text{const.} & (\Omega \rightarrow 0, \Lambda = 0) \end{array}} \quad (3.46)$$

We see that in an expanding matter-dominated universe the density doesn't grow exponentially, as in a static medium, but just linearly, or if the density is much lower than the critical density, it doesn't grow at all.

We assume that the temperature fluctuations in the cosmic microwave background are adiabatic and that photons and baryons are coupled before recombination via Thomson scattering. The temperature fluctuations are then related to the density fluctuations at that time through:

$$\frac{\delta T}{T} = \frac{\delta\rho_\gamma}{\rho_{0,\gamma}} = \frac{\delta\rho_B}{\rho_{0,B}}.$$

From the CMB measurements we know:

$$\frac{\Delta T}{T} \simeq 10^{-5} \Rightarrow \delta_B < 5 \cdot 10^{-5}.$$

Since these fluctuations can at best grow by a factor of  $(z + 1) \sim 1100$ , we would expect

$$\delta_B(t = t_0) < 0.1.$$

This means, in a purely baryonic universe we cannot explain how galaxies and clusters could have formed until today. Once again dark matter solves this problem. As long as our universe has been radiation dominated the rapid expansion prevented the growth of structure. After matter-radiation equality ( $a_{eq}, t_{eq}$ ) perturbations with  $\lambda > \lambda_J$  started to grow as seen in equation (3.46) with a rate of  $\delta \propto a$ .

$$\delta_{DM} \propto \begin{cases} \text{constant} & (t < t_{eq}) \\ a & (t > t_{eq}) \end{cases} \quad (3.47)$$

This is only valid for dark matter since the baryons and photons remain tightly coupled to each other via Thomson scattering until the time of decoupling  $t_{dec}$  at  $z_{dec} \sim 1100$ . During this period the sound speed is approximately that of a photon gas:

$$c_s = \sqrt{\frac{\partial p}{\partial \rho}} \quad \text{with} \quad p = \frac{1}{3}\rho c^2 \\ \Rightarrow c_s = \frac{c}{\sqrt{3}}.$$

This high sound speed prevented all fluctuations with  $M < M_J(t < t_{dec}) \sim 10^{14} M_\odot$  from growing, i.e. fluctuations of smaller sizes were just oscillating. After the decoupling of the baryons from the photons the sound speed is just the velocity dispersion of a gaseous mixture of hydrogen and helium and the Jeans mass drops by a factor of  $\sim 10^{-9}$  and the perturbations can grow with the usual matter-dominated growth rate of  $\delta \propto a$

$$\delta_B \propto \begin{cases} \text{constant} & (t < t_{eq}) \\ \text{constant} & (t_{eq} < t < t_{dec}) \\ a & (t > t_{dec}) \end{cases} \quad (3.48)$$

During the time from  $t_{eq}$  to  $t_{dec}$  the perturbations in dark matter would have grown by a factor of  $\sim 3$  and after the decoupling from the photons the baryons will experience the perturbed gravitational potential of the dark matter and 'fall into' the potential wells created by dark matter. Hence  $\delta_B$  will encounter a phase of increased growth after decoupling until reaching the value of  $\delta_{DM}$ , from that point on both components will grow as  $\delta \propto a$  (see Fig. (3.2)).

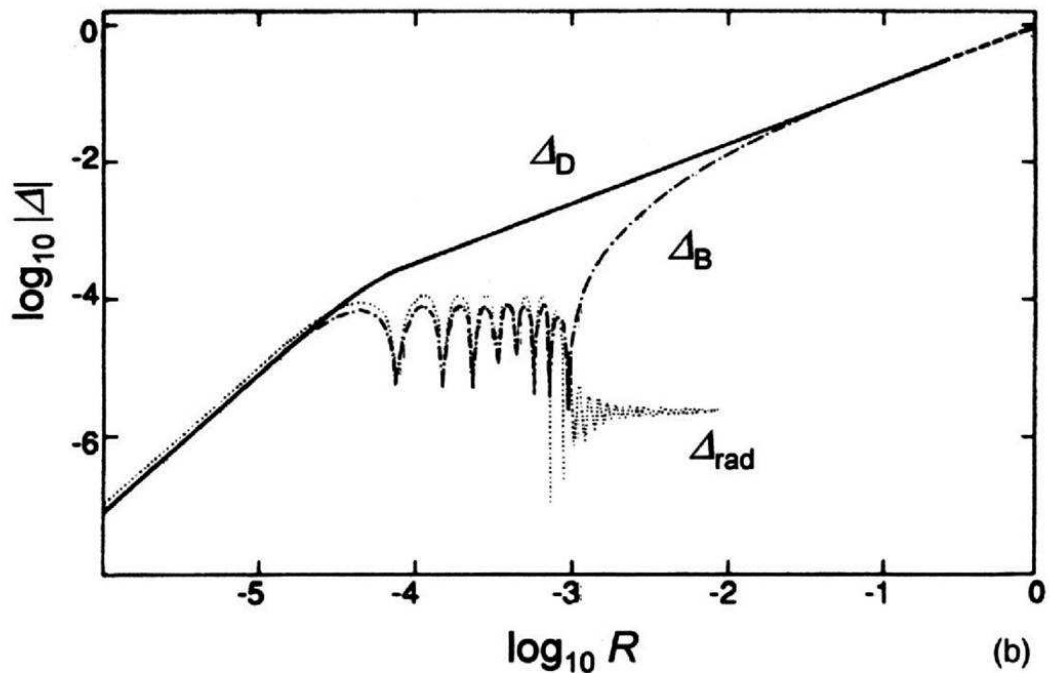


**Figure 3.2:** Evolution of density fluctuations (Longair 1998): This picture shows the amplitude of density fluctuations  $\delta(= \Delta)$  plotted against the expansion factor  $a(= R)$ . Between the time of matter-radiation equality and the time of recombination the baryon fluctuations are just oscillating ( $\Delta_B$ , dashed-dotted line) whereas the dark matter fluctuations are still growing ( $\Delta_{DM}$ , solid line). After recombination the baryonic fluctuations experience an epoch of increased growth until they are similar to the dark matter fluctuations

### 3.5 Zeldovich approximation

To follow the development of gravitational instabilities in the non-linear epochs ( $\delta > 1$ ), one has to rely on numerical simulations. There are some useful special cases and approximations, though, e.g. *The Zeldovich Approximation* (Zel'Dovich 1970) and *The Top-Hat spherical collapse* that will be described here.

The Zeldovich approximation is a first-order Lagrangian perturbation theory using a kinematical approach to the formation of structure. In this approach, at first the initial displacement of particles is worked out, the particles are then assumed to move on this initial direction. The proper coordinate of a given particle can then be written as

$$\mathbf{x}(t) = a(t)\mathbf{q} + b(t)\mathbf{f}(\mathbf{q}), \quad (3.49)$$

where  $\mathbf{x}$  is the comoving Eulerian position,  $\mathbf{q}$  is the Lagrangian position pointing at the original position of the particle and  $b(t)$  is a function scaling the time-independent displacement field  $\mathbf{f}(\mathbf{q})$ . The Eulerian density can be obtained using the Jacobian of the transformation between  $\mathbf{x}$  and  $\mathbf{q}$ , this yields

$$\frac{\rho}{\rho_0} = \left[ \left(1 - \frac{b}{a}\alpha\right) \left(1 - \frac{b}{a}\beta\right) \left(1 - \frac{b}{a}\gamma\right) \right]^{-1}, \quad (3.50)$$

where  $(-\alpha, -\beta, -\gamma)$  are the eigenvalues of the strain tensor  $\partial f_i / \partial q_j$ . This expression describes the deformation of an infinitesimal cuboid, where collapse takes place first in the direction of the axis specified by the largest negative eigenvalue, this corresponds to the shortest axis. This means Gravity aggravates spherical asymmetry, leading to flattened structures known as pancakes.

The main advantage of this first-order Lagrangian perturbation theory is that it yields results that are comparable in accuracy to Eulerian theory with higher-order terms included. The Zeldovich approximation works so well mainly because the scheme for extrapolating peculiar velocities is exact in one dimension. Like mentioned before structures tend to first collapse into sheet-like structures, the so called pancakes. This means that the final stages of the collapse are nearly one dimensional and are therefore well described by the Zeldovich approach.

The Zeldovich approximation is commonly used for creating quasi-linear initial conditions for cosmological N-body simulations (Efstathiou et al. 1985). All the initial conditions used for simulations for this thesis have been created this way.

As the Zeldovich approach is describing a collapse of structure where asphericity is accentuated it works least well in situations of exact spherical symmetry. This case is described in the following section.

### 3.6 Top-Hat spherical collapse

The collapse of an overdense sphere in a matter-dominated Universe is a very useful nonlinear model, as it behaves exactly like a closed  $k = +1$  Friedmann universe. The perturbation doesn't need to be a uniform sphere, but spherically symmetric. The time evolution of a shell of the sphere will be the same as if the sphere inside the shell would be uniform with the same amount of mass. Therefore, in the following density refers to the mean density inside a given sphere. The equations of motion are the same as for the scale factor and can be obtained by standard techniques from

$$\ddot{r} = -\frac{GM}{r^2}$$

For a matter-dominated Universe we find the following parametric cycloid solution for the proper radius and time

$$r = A(1 - \cos\Theta) \quad (3.51)$$

$$t = B(\Theta - \sin\Theta) \quad (3.52)$$

with  $A^3 = GMB^2$  and  $\Theta$  being the development angle. From this we can derive an expression for the overdensity for the collapsing sphere as a function of  $\Theta$  ( $\Theta \neq 2\pi$ ) (see e.g. Padmanabhan (2000))

$$\delta = \frac{9(\Theta - \sin\Theta)^2}{2(1 - \cos\Theta)^3} \quad (3.53)$$

Expanding these relations up to order  $\Theta^5$  for small  $t$ , we recover the matter-dominated linear growth law  $\delta \propto t^{2/3}$  just like in section (3.4).

$$\delta \approx \frac{3}{20}\Theta^2; \quad t \approx \frac{B}{6}\Theta^3 \quad (3.54)$$

$$\Rightarrow \delta \approx \frac{3}{20} \left(\frac{6t}{B}\right)^{2/3} \quad (3.55)$$

We take a closer look at three interesting stages in the evolution of the spherical collapse model:

1. **Turnaround:** At  $\Theta = \pi$ ,  $t = \pi B$  the overdense sphere is separating from the general expansion of the Universe and reaches its maximum radius. The overdensity at that point is  $\delta = 5.55$  from equation (3.53), in contrast to the prediction of linear theory which is just  $\delta_{lin} \approx 1.06$  from equation (3.55).
2. **Collapse:** If gravity would be the only active force, the sphere would collapse to a singularity at  $\Theta = 2\pi$ ,  $t = 2\pi B$  corresponding to a linear overdensity of  $\delta_{lin} = 1.69$ .

3. **Virialization:** Obviously, collapse to a singularity won't happen in reality. Phase mixing of particle orbits will convert kinetic energy into random motions and the collapse will come to a halt. Once the sphere has collapsed by a factor of two, the kinetic energy  $K$  is related to the potential energy by  $V = -2K$ , the condition for equilibrium, according to the *virial theorem*. This occurs at  $\Theta = 3\pi/2$  in a non-dissipative collapse, resulting in an overdensity of  $\delta \approx 147$  and  $\delta_{lin} \approx 1.58$ , respectively. Commonly this virialized state is assumed to be eventually achieved only at the collapse time of  $\Theta = 2\pi$  where the overdensity is  $\delta \approx 178$ . Often this number for the required overdensity for virialization is approximated by a value of  $\delta_{vir} = 200$ .

In general, linear theory is assumed to be valid until  $\delta_{lin}$  is equal to some  $\delta_c$  a little greater than unity. For values greater than that virialization is deemed to have occurred.



# NUMERICAL METHODS

All the simulations for this work have been performed with the help of the cosmological Tree-SPH (smoothed particle hydrodynamics) code GADGET2. In this chapter, we will summarize the most important numerical details and physical modules used for our simulations. See Springel & Hernquist (2002) and Springel (2005) for a complete discussion of the numerical methods used in the code.

## 4.1 Gravitational N-body Problem

If the spatial extend of a set of gravitational interacting objects is small compared to the mean distance of the objects the system may be treated as a simple gravitational N-body system. This is true for many structures in astronomy, e.g. the motion of galaxies in a cluster or the motion of single stars in a galaxy or star cluster. The trajectory of each member of the system is then set by the sum of the gravitational forces exerted by all other objects. The acceleration  $a_i$  of particle  $i$  is then given by Newton's law:

$$\mathbf{a}_i = - \sum_{j \neq i} \frac{Gm_j}{r_{ij}^3} (\mathbf{r}_i - \mathbf{r}_j), \quad (4.1)$$

where  $G$  is the gravitational constant,  $m_j$  is the mass of particle  $j$ ,  $\mathbf{r}_i$  and  $\mathbf{r}_j$  are the positions of particles  $i$  and  $j$ , respectively, which are separated by a distance  $r_{ij} = |\mathbf{r}_j - \mathbf{r}_i|$ .

The corresponding equations of motion are given by 3  $N$  first-order ordinary differential equations:

$$\frac{d\mathbf{r}_i}{dt} = \mathbf{v}_i, \quad (4.2)$$

$$\frac{d\mathbf{v}_i}{dt} = \mathbf{a}_i, \quad (4.3)$$

where  $\mathbf{v}_i$  and  $\mathbf{r}_i$  are the velocity and the position of particle  $i$ , and the acceleration  $\mathbf{a}_i$  is given by Eq. 4.1.

Unlike, e.g. the electromagnetic force which can be balanced by opposite charges so that the net effect over large distances is nullified, the range of the gravitational force is infinite. This implies a high dynamic range to the problems and the equations of motions are highly non-linear where analytical solutions only exist to some very contrived problems (see section 3.6). In most cases the only way to study the evolution of such systems is with the help of numerical simulations, where the first-order differential Eqs. 4.3 and 4.3 are replaced by linear differential equations and the positions  $\mathbf{r}_i$  and velocities  $\mathbf{v}_i$  are only re-evaluated at discrete time intervals. GADGET utilizes the commonly used "leapfrog" integration scheme in the "kick-drift-kick" (KDK) form (see Quinn et al. 1997) to advance particle positions and velocities in time:

$$\mathbf{r}_i^{n+1/2} = \mathbf{r}_i^n + \frac{1}{2}\mathbf{v}_i^n \Delta t_i^n \quad (4.4)$$

$$\mathbf{v}_i^{n+1} = \mathbf{v}_i^n + \mathbf{a}_i^{n+1/2} \Delta t_i^n \quad (4.5)$$

$$\mathbf{r}_i^{n+1} = \mathbf{r}_i^{n+1/2} + \frac{1}{2}\mathbf{v}_i^{n+1} \Delta t_i^n, \quad (4.6)$$

where  $\Delta t_i^n$  is the particle's time step from  $n$  to  $n+1$ . The gravitational accelerations are calculated at the beginning of each time-step and constitute the most time-consuming part in any modern  $N$ -body simulation code.

In order to reduce computational time while preserving accuracy GADGET uses individual timesteps for the particles. The frequency at which a the gravitational forces on a particle is updated is indirectly proportional to the gravitational acceleration itself:

$$\Delta t_i = \min \left( \Delta t_{\max}, \left( \frac{2\eta\epsilon_i}{|\mathbf{a}_i|} \right)^{1/2} \right), \quad (4.7)$$

where  $\eta$  is an accuracy parameter (throughout this work we adopted a value of  $\eta = 0.02$ ),  $\epsilon_i$  is the gravitational softening length of the particle (see Section 4.2), and  $\Delta t_{\max}$  is the maximal allowed timestep as given by the user (see Springel 2005).

## 4.2 Gravitational Softening

In simulations of galaxy formation it is and will be in the foreseeable future impossible to simulate the motion of single stars in massive galaxies in a reasonable amount of time. Additionally, we want to simulate the evolution of the smoothly distributed gaseous and dark-matter component of galaxies under the influence of gravity. Therefore we use tracer particles which are rather massive in the simulations that are assumed to be a Monte-Carlo representation of the underlying, smoother mass distribution. To avoid the singularities in the gravitational potential that arise at the particle positions, simulation codes in general use some kind of *softening* to mimic their actual spatial extend. This helps to prevent the forces from diverging which would result in unfeasible short timesteps and unphysical behavior. The gravitational potential  $\Phi$  at the position

$\mathbf{r}$  is can be approximated e.g. by Plummer softening (Aarseth 1963)

$$\Phi(\mathbf{r}) = -G \sum_j \frac{m_j}{(|\mathbf{r} - \mathbf{r}_j|^2 + \epsilon^2)^{1/2}}, \quad (4.8)$$

whith a *softening length*  $\epsilon$  or spline softening (Monaghan & Lattanzio 1985)

$$\Phi(\mathbf{r}) = -G \sum_j m_j g(|\mathbf{r} - \mathbf{r}_j|), \quad (4.9)$$

where  $g(r) = -\frac{1}{h}W_2(r, h)$  with *softening length*  $h$ . For example in GADGET  $W_2$  is given by

$$W(r, h) = \frac{8}{\pi h^3} \begin{cases} 1 - 6 \left(\frac{r}{h}\right)^2 + 6 \left(\frac{r}{h}\right)^3, & 0 \leq \frac{r}{h} \leq \frac{1}{2}, \\ 2 \left(1 - \frac{r}{h}\right)^3, & \frac{1}{2} < \frac{r}{h} \leq 1, \\ 0, & \frac{r}{h} > 1. \end{cases} \quad (4.10)$$

The advantage of the spline softening is, that the forces become exactly Newtonian for  $r > h$ , while the Plummer softening is only slowly converging towards Newton's law. In cosmological simulation it is common to use a comoving softening length  $\epsilon_{com}$ , the physical softening length is then growing with the scale factor  $a$  as  $\epsilon_{phys} = a\epsilon_{com}$ .

To find an optimal value for the softening length is a non-trivial problem and there is plenty of literature about this issue (e.g Merritt 1996; Athanassoula et al. 2000; Dehnen 2001). The problem is that too large a value result in a loss of spatial resolution whereas a softening length that is choosen too small will lead to small scale fluctuations in the forces due to the finite representation of the actually smooth density distribution.

### 4.3 Tree Codes

The most naive, yet the most exact way, to calculate the gravitational forces would be the summation of Eqn. 4.1 over all particles in the system ("direct  $N$ -body method"). However, modern simulations like the upcoming Millenium XXL simulation (Angulo & White 2011) use more than  $10^{11}$  particles and since the computation time of this method scales with  $\sim N^2$  this would yield unfeasible long computation times even on the most powerful computer clusters available today.

A solution to this problem is in using so called "hierarchical tree-codes" (Barnes & Hut 1986; Dehnen 2000). The idea is to use direct summation of the gravitational forces only for the particles in close proximity while for particles farer away only a low-order multipole expansion (or in the case of GADGET just the monopole expansion) of the combined gravitational potential of a group of particles is used. This results in scaling of the computation time of merely  $\sim N \log(N)$ . To achieve quick access during the force calculation to single particles or group of particles they are sorted into a hierarchical structure called a tree.

The most commonly used methods for this hierarchical structuring are the so called "binary-trees" and the "oct-trees". Since GADGET uses the latter method we refer to

the literature for a description of the former (see e.g. Makino 1990 and references therein). In an "oct-tree" the whole simulation volume (root-cell) is divided into 8 equally large cubes, the first 8 nodes of the tree. Each of these cubes is itself divided into 8 sub-cells or nodes and so on until a cube only contains a single or no particle at all. To decide whether for the calculation of the gravitational force onto a particle the combined gravitational potential of a branch of the tree is used or whether the "tree walk" has to continue to the sub-branches we need an opening criterion. In GADGET this is given by:

$$\frac{GM_j}{r_{ij}^2} \left( \frac{l_j}{r_{ij}} \right)^2 \leq \alpha |\mathbf{a}_i^{\text{old}}|, \quad (4.11)$$

where  $M_j$  and  $l_j$  are the mass and spatial extent of the tree node under consideration,  $r_{ij}$  is the distance of the particle  $i$  to the node  $j$ ,  $\mathbf{a}_i^{\text{old}}$  the acceleration of the particle in the last time step and  $\alpha$  is an accuracy parameter. The benefit of this definition is, that it is adaptive to the local dynamics allowing for better force accuracy in regions where the gravitational forces are strong.

Although the sorting of the particles in this way produces some overhead the overall decrease in computation time is quite significant, since compared to the direct summation approach the scaling of the number of needed calculations drops from  $\mathcal{O}(N^2)$  to  $\mathcal{O}(N \log N)$ .

## 4.4 Smoothed Particle Hydrodynamics

In the presence of baryonic matter we have to consider the hydrodynamic forces in addition to the gravitational attraction. This is usually accomplished either with a grid based method where the hydrodynamic equations are solved for the bounding faces of the grid cubes or with the help of smoothed particle hydrodynamics (SPH, see e.g. Lucy 1977; Gingold & Monaghan 1977; Monaghan 1992) which uses tracer particles to represent the continuous density distribution similar to the method used to calculate the gravitational forces which is why this method can make use of the "oct-tree" that was already built for the gravity calculations (see Section 4.3). GADGET uses the latter method, therefore again we refer to other work for a description of grid codes (Berger & Olinger 1984; Khokhlov 1998).

The particles used for SPH are - similar to the gravitational force calculations - best be thought of discrete fluid particles with a position  $\mathbf{r}_i$ , velocity  $\mathbf{v}_i$  and mass  $m_i$  "smeared out" over some finite volume. The thermodynamic quantities are then determined by interpolating over nearby particles. The smoothing kernel used is the same one as used for the gravity calculations (see Eqn 4.10) but whereas the softening length for the gravitational forces is fixed in GADGET for a certain particle type the smoothing length for SPH is given by the distance in which a certain number of neighbouring particles (we use  $40 \pm 5$ ) can be found. Thus SPH is inherently an adaptive method where high-density regions are treated with the highest level of accuracy and only a

small fraction of the computational time is spent for the low-density regions. In the case of freely adapting smoothing lengths, this implementation of SPH in GADGET is strictly entropy and energy conserving (see Springel & Hernquist 2002; Springel 2005).

In the conventional implementation of SPH (Monaghan 1992), the density estimate for particle  $i$  is obtained by computing the weighted sum over all  $N$  neighboring particles:

$$\rho_i = \sum_{j=1}^N m_j W(|\mathbf{r}_{ij}|, h_i), \quad (4.12)$$

where  $\mathbf{r}_{ij} \equiv \mathbf{r}_i - \mathbf{r}_j$ ,  $h_i$  is the adaptive smoothing length of particle  $i$  and  $W(r, h)$  is the SPH kernel as defined by Eqn. 4.10.

The pressure  $P_i$  is related to the density using the equation of state of an ideal gas,

$$P_i = A_i \rho_i^\gamma, \quad (4.13)$$

where  $\gamma = 5/3$  is the adiabatic gas index and  $A \equiv P/\rho^\gamma$  is the "entropic function". GADGET uses the entropy or to be precise  $A = A(S)$  instead of the thermal energy as the independent thermodynamical variable in order to achieve both entropy and energy conservation (see full discussion in Springel & Hernquist 2002). The internal energy per unit mass related to  $A$  via

$$u = \frac{A}{\gamma - 1} \rho^{\gamma-1} \quad (4.14)$$

The discretized form of the equations of motion of the SPH particles - without the effects of gravity is given by

$$\frac{dv_i}{dt} = - \sum_{j=1}^N m_j \left[ f_i \frac{P_i}{\rho_i^2} \nabla_i W_{ij}(h_i) + f_j \frac{P_j}{\rho_j^2} \nabla_i W_{ij}(h_j) \right], \quad (4.15)$$

where the coefficients  $f_i$  are defined by

$$f_i = \left[ 1 + \frac{h_i}{3\rho_i} \frac{\partial \rho_i}{\partial h_i} \right]^{-1}, \quad (4.16)$$

and the abbreviation  $W_{ij}(h)$  is a short notation for  $W(|\mathbf{r}_i - \mathbf{r}_j|, h)$ . The above equations fully define reversible fluid dynamics, where without external heat sources the entropy of each particle stays constant. However, to account for dissipative effects, which convert kinetic energy into heat (e.g. shocks) and thereby increase the entropy of the system an additional viscous force is introduced. In GADGET it has the following form:

$$\left. \frac{d\vec{v}_i}{dt} \right|_{\text{visc}} = - \sum_{j=1}^N m_j \Pi_{ij} \nabla_i \bar{W}_{ij}, \quad (4.17)$$

with  $\overline{W}_{ij}$  being the arithmetic mean of the two kernels  $W_{ij}(h_i)$  and  $W_{ij}(h_j)$ . The viscosity is given by

$$\Pi_{ij} = -\frac{\alpha [c_i + c_j - 3w_{ij}] w_{ij}}{2 \rho_{ij}}, \quad (4.18)$$

where  $c_i$  and  $c_j$  are the sound speed of particle  $i$  and  $j$ , respectively, and  $w_{ij} = \mathbf{v}_{ij} \cdot \mathbf{r}_{ij} / |\mathbf{r}_{ij}|$  is the relative velocity of the two particles projected onto the separation vector. Viscosity only acts on converging particles, i.e. in the case of  $\mathbf{v}_{ij} \cdot \mathbf{r}_{ij} > 0$  the viscous force is set to 0. For the artificial bulk viscosity constant  $\alpha$  we chose a value of 0.75.

The signal-velocity approach imposes another time step criterion onto the SPH particles. It ensures that information is not propagated further than a fraction  $C$  of a particle's smoothing length during one time step (Courant et al. 1928). The longest allowed timestep that fulfills the Courant condition is given by

$$\Delta t_i^{(\text{hyd})} = \frac{C_{\text{courant}} h_i}{\max_j (c_i + c_j - 3w_{ij})} \quad (4.19)$$

where the maximum  $\max_j$  of the signal velocities  $v_{ij}^{\text{sig}} = c_i + c_j - 3w_{ij}$  (Monaghan 1997, see also Eq. 4.18) is determined with respect to all neighboring particles. Throughout this work we adopted a value of  $C_{\text{courant}} = 0.15$ . The timestep used for an SPH particles is then finally determined as the minimum over the timestep criterion imposed by the gravity computation as defined in Eq. 4.7 and the Courant condition.

Additionally a viscosity limiter is used to prevent the spurious transport of angular momentum in shear flows (Balsara 1995; Steinmetz 1996). This is accomplished by multiplying the viscous tensor with  $(f_i + f_j)/2$ , where

$$f_i = \frac{|\nabla \times \vec{v}|_i}{|\nabla \cdot \vec{v}|_i + |\nabla \times \vec{v}|_i} \quad (4.20)$$

is a simple estimate for the relative amount of shear in the flow around particle  $i$  (Monaghan 1992).

## 4.5 Additional Physics

On top of the self-consistent implementation of the gravitational and hydrodynamic forces there is a variety of modules by several authors for the treatment of different physical processes that are relevant for galaxy formation. We will give an overview of the models used in the simulations that are presented in this thesis.

The code implements radiative cooling, following Katz et al. (1996), for a primordial composition of hydrogen and helium, where the cooling rates are computed under the assumption that the gas is optically thin and in ionization equilibrium. Additionally, the simulations include a spatially uniform redshift-dependent UV background

radiation field, which is assumed to arise from active galactic nuclei and star-forming galaxies, with a modified Haardt & Madau 1996 spectrum, where reionization takes place at  $z \approx 6$  (Davé et al. 1999) and the UV background radiation field peaks at  $z \approx 2 - 3$ . For a recent detailed investigation on the effects of varying the background radiation field on the evolution of galaxies, see e.g. (Hambrick et al. 2011).

For the star formation and feedback prescription we use the self-regulated, sub-grid supernova feedback model of Springel & Hernquist 2003. This model treats the interstellar medium (ISM) as a two-phase medium (McKee & Ostriker 1977; Johansson & Efstathiou 2006) where clouds of cold gas are embedded in the hot gas phase at pressure equilibrium. Stars are allowed to form out of the cold gas phase and the associated supernovae feedback is assumed to effectively heat and pressurize the surrounding ISM. This model attempts to describe star formation on scales that are not resolved in the simulation. Following McKee & Ostriker (1977), the gas is assumed to develop a run-away cooling instability once the gas density exceeds a certain density threshold,  $\rho > \rho_{th}$ . Stars will then form on a characteristic timescale  $t_*$  out of the cold gas, whereas the massive short-lived stars are supposed to instantaneously explode as supernovae of type II (SNII). This will lead to evaporation of the cold gas clouds and immediately returns a fraction of the stellar mass to back to the ISM. In this work we assumed a Salpeter initial mass function (IMF, Salpeter 1955), where a mass fraction of  $\beta = 0.1$  of the newly formed stars exceed the mass limit ( $M_* > 8M_\odot$ ) for SNII. For the energy released to the ISM we adopt the canonical value of  $10^{51}$  erg per supernova explosion. The star formation rate (SFR) is given by

$$\frac{d\rho_*}{dt} = \frac{\rho_c}{t_*} - \beta \frac{\rho_c}{t_*} = (1 - \beta) \frac{\rho_c}{t_*} \quad (4.21)$$

where  $\rho_*$  and  $\rho_c$  are the densities of stars and cold gas, respectively, and  $t_*$  is the star formation time scale for which we assume a value of  $t_* = 2.1$  Gyr chosen to recover the observed Kennicutt-Schmid relation (Kennicutt 1998; Springel & Hernquist 2003).

The constant mass and energy transfer between the two phases leads to self-regulated star formation. The ambient hot gas feeds the cold gas clouds by radiative cooling. Star formation and the associated supernovae feedback will lead to the evaporation of the cold gas, reducing the cold gas density which will result in lower star formation rate. The mass transfer between the phases is represented by the respective rate equations

$$\frac{d\rho_c}{dt} = -\frac{\rho_c}{t_*} - A\beta\frac{\rho_c}{t_*} + \frac{1-f}{u_h - u_c}\Lambda_{\text{net}}(\rho_h, u_h), \text{ and} \quad (4.22)$$

$$\frac{d\rho_h}{dt} = \beta\frac{\rho_c}{t_*} + A\beta\frac{\rho_c}{t_*} - \frac{1-f}{u_h - u_c}\Lambda_{\text{net}}(\rho_h, u_h), \quad (4.23)$$

where  $\rho_h$  is the density of the hot gas and  $A \propto A_0\rho^{-4/5}$  describes the cloud evaporation. The first term on the right hand side in each of these equations describes star formation and feedback, the second cloud evaporation, and the third the growth of clouds due to radiative cooling of the gas, where  $u_c$  and  $u_h$  are the thermal energy per unit mass of the hot and cold component, and the net cooling function in the presence of an

external UV radiation field is given by  $\Lambda_{\text{net}}(\rho, u)$ . The thermal instability that leads to the growth of the cold clouds is assumed to be operating ( $f = 0$ ) in regions where the gas density surpasses the density threshold  $\rho_{th}$  otherwise  $f$  is set to 1.

The supernovae feedback description will act as an additional source of pressure resulting in an effective equation of state of the form

$$P_{\text{eff}} = (\gamma - 1)(\rho_h u_h + \rho_c u_c). \quad (4.24)$$

This equation of state provides pressure support from the sub-grid model and leads to the self-regulation of star-formation.

With the temperature of the cold gas fixed at  $T_{\text{cold}} = 1000$  K, a supernovae 'temperature' of  $T_{SN} = 10^8$  K and the cloud evaporation  $A = 1000$  the number density threshold for star formation is set by the code to  $n_{th} = 0.227$  to ensure that the equation of state is continuous at the onset of star formation.

## 4.6 Simulations

To study the formation and evolution of galaxies we performed more than 60 cosmological 'zoom-in' simulations with all the physical modules included that are explained in section 4.5. In order to prevent spurious star formation at high redshift the cosmological simulations additionally to the physical density threshold require a local over-density of  $\Delta > 55.7$  for star formation to set in. The regions of interest for resimulation are identified using a dark-matter-only simulation described in section 4.6.1. In section 4.6.2 we explain the zoom-in resimulations.

### 4.6.1 The large-scale dark matter simulation

To find candidate dark matter halos for later refinement we performed a dark matter only simulation of a cosmological volume with a comoving side length of  $72\text{Mpc } h^{-1}$  including  $512^3$  dark matter particles with individual masses of  $m_p = 2 \times 10^8 M_{\odot} h^{-1}$ . The box is large enough to provide a representative piece of the universe and the mass resolution fine enough to allow us to reliably find dark matter halos with  $\sim 10^3$  particles being more massive than  $\sim 10^{11} M_{\odot} h^{-1}$ . The initial conditions were created using GRAFIC1 and LINGERS (Bertschinger 1995), assuming a  $\Lambda\text{CDM}$  cosmology with nearly scale-invariant initial adiabatic fluctuations. This software package uses the Zeldovich approach (see section 3.5) to produce the initial conditions. The cosmological parameters are based on the 3-year results from WMAP (Spergel et al. 2007) with  $\sigma_8=0.77$ ,  $\Omega_m=0.26$ ,  $\Omega_{\Lambda}=0.74$ ,  $h = 0.72$  ( $\equiv H_0=100h \text{ kms}^{-1}\text{Mpc}^{-1}$ ) and the initial slope of the power spectrum is  $n_s=0.95$ . The initial conditions were then evolved from a redshift of  $z \sim 43$  to  $z = 0$  using GADGET-2 (Springel 2005) with a fixed comoving gravitational softening length of  $2.52\text{kpc } h^{-1}$ . The simulation data was stored in 95 snapshots separated by  $\Delta a = 0.01$  beginning at a cosmological expansion factor of  $a=0.06$  ( $z \approx 43$ ).

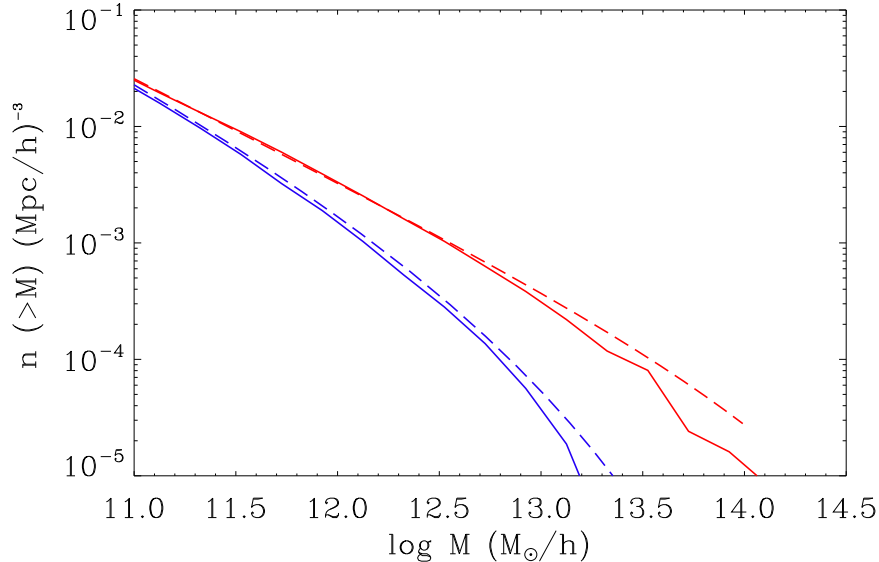


**Figure 4.1:** Dark matter mass Function (solid) of the  $(72h^{-1}Mpc)^3$  box at  $z=0$  (red) and  $z=2$  (blue). The dashed lines show the prediction of Sheth et al. (2001).

At  $z=0$  we identify halos with a friends-of-friends algorithm and determine their centers using the shrinking sphere technique (Power et al. 2003). We then use the radius where the mean density drops below 200 times the critical density of the universe ( $r_{vir} \equiv r_{200}$ ) to measure the halo mass therein ( $m_{vir} \equiv m_{200}$ ). This results in a complete halo catalogue ( $n_{halos} = 41313$ ) for halos more massive than  $2 \times 10^{10} M_{\odot} h^{-1}$  which have properties typical for this kind of simulation (see Moster et al. 2010 for additional analysis of this simulation). In brief, we show the dark matter halo mass function at  $z=0$  and  $z=2$  in Fig. 4.1 along with the analytical prediction from Sheth et al. (2001) where we find small variations at the high mass end due to the limited boxsize. The corresponding distribution of the dimensionless spin parameter

$$\lambda' \equiv \frac{J}{\sqrt{2}m_{vir}V_c r_{vir}}, \quad (4.25)$$

defined by Bullock et al. (2001), is shown in Fig. 4.2. Here  $J$  is the total angular momentum within  $r_{vir}$  and  $V_c$  is the halo circular velocity  $V_c^2 = Gm_{vir}/r_{vir}$ . The distribution of angular momenta is consistent with previous simulations (Bullock et al. 2001; Vitvitska et al. 2002) and can be fitted with a log-normal distribution

$$P(\lambda') = \frac{0.01}{\lambda' \sqrt{2\pi}\sigma} \exp\left(-\frac{\ln^2(\lambda'/\lambda'_0)}{2\sigma^2}\right) \quad (4.26)$$

with best-fit values  $\lambda'_0 = 0.038$  and  $\sigma = 0.58$ .

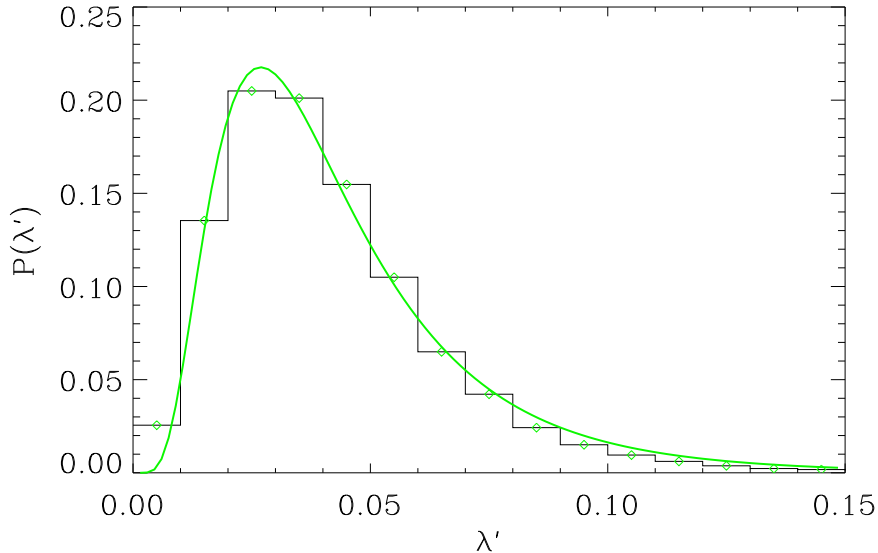


**Figure 4.2:** Spin parameter distribution for the dark matter box. The green line shows the log-normal-fit with best fit values  $\lambda'_0 = 0.038$  and  $\sigma = 0.58$ .

#### 4.6.2 Refined Simulations

For the higher resolution re-simulations of individual halos we trace all dark matter particles that are closer than  $2 \times r_{200}$  to the center of the halo at  $z=0$ . Following the halo back in time we include all particles in the tracing process which are within  $2 \times r_{200}$  of the halo center at any given snapshot. This ensures that halo encounters during the assembly of the halo of interest are always resolved. We found this to be an efficient mechanism to reduce contamination with massive boundary particles. The traced particles define the region for which we have to generate higher resolution initial conditions. For the cuboid enclosing this region we compute the short wavelength modes of the perturbation spectrum using GRAFIC2 (Bertschinger 2001). Based on the new spectrum we replace the low resolution dark matter particles with dark matter as well as gas particles at higher resolution ( $\Omega_b=0.044$ ,  $\Omega_{dm}=0.216$ ). We only consider coherent regions within the cuboid that actually contain traced particles. Other regions as well as a 'safety margin' of  $1\text{Mpc h}^{-1}$  around the high-resolution cuboid are populated with particles from the original initial conditions. To approximate the long range tidal forces, particles from the original simulation being further away from the center are merged, with the particle masses increasing as the square of the distance from the region of interest. This and the inclusion of periodic boundaries ensures that tidal forces from distant regions are accurately included in the computations.

We obtain amoeba shaped initial conditions (see Fig. 4.3) for which, on average, approximately 30% of the high resolution dark matter particles end up inside the virial radius at redshift  $z = 0$  (see Power et al. 2003 and in particular Jenkins 2010 for

alternative ways of creating high resolution initial conditions). The particle number in the boundary region is kept low enough to perform the simulations in a reasonable time. For example the most massive halo #0040 which has a total mass  $m_{200}$  of  $2.7 \times 10^{13} M_{\odot} h^{-1}$  at  $z = 0$  took  $\sim 23000$  CPU-hours to evolve ( $3.8 \times 10^6$  high-resolution particles in dark matter and gas each). In the re-simulations the particles in the high resolution regions have a gas and star mass of  $m_{*,gas} = 4.2 \times 10^6 M_{\odot} h^{-1}$  (we spawn one star per gas particle) and a dark matter mass of  $m_{dm} = 2.5 \times 10^7 M_{\odot} h^{-1}$  which is 8 smaller than in the original simulation. The comoving gravitational softening length for the gas and star particles is  $400 \text{pc} h^{-1}$  and  $890 \text{pc} h^{-1}$  for the high resolution dark matter particles, scaled with the square root of the mass ratio (Dehnen 2001). Compared to some other recent cosmological zoom simulations (Scannapieco et al. 2009; Governato et al. 2009; Piontek & Steinmetz 2009; Feldmann et al. 2010) the resolution level of our simulations at  $M_{halo} \approx 10^{12} M_{\odot}$  is slightly lower. But while these simulations are limited to a few halos in a small mass range we performed a significantly larger number of re-simulations of halos spanning a mass range of almost two orders of magnitude. The present-day properties of our re-simulated galaxies can be found in Table 5.1. Finally, we also performed a number of re-simulations at higher resolution, i.e. with particle masses 8 times lower and half the softening length. While increasing resolution can slightly change the individual accretion histories of the galaxies, the global trends found in this work remain unchanged.

### 4.6.3 The baryonic mass budget

Using similar parameters for zoom simulations has been shown to result in galaxies with reasonable present day properties (Naab et al. 2007, 2009; Johansson et al. 2009b). However, the employed star formation prescription favors efficient star formation at early times resulting in preferentially spheroidal systems with old stellar populations, due to the strongly self-regulated feedback which does not produce the supernova driven winds that are often observed in star-forming galaxies. Fig. 4.4 shows the conversion efficiency of the simulated galaxies at the present day  $f_* = m_*/(f_b * m_{vir,dark})$  where  $m_*$  is the stellar mass within 10 % of the virial radius,  $f_b = \Omega_b/\Omega_{dm} = 0.20$  is the cosmic baryon fraction and  $m_{vir,dark}$  is the dark matter mass within the virial radius of the galaxy. Therefore  $f_b * m_{vir,dark}$  is the amount of total baryonic matter available in each halo and  $f_*$  the fraction thereof that is converted into stars in the central galaxy. This fraction declines in a roughly linear fashion with the logarithm of the halo mass from  $f_* \approx 0.5$  for the smallest halos ( $\approx 10^{11.9} M_{\odot}$ ) to  $f_* \approx 0.15$  for high mass halos ( $\gtrsim 10^{13} M_{\odot}$ ), still over-predicting by a factor of 2 the estimation from recent models (see however Shankar et al. (2006) who find higher efficiencies for high mass galaxies) that are tested by matching observed luminosity functions to simulated halo mass functions (Moster et al. 2010; Guo et al. 2010b; Conroy & Wechsler 2009; Behroozi et al. 2010) or weak lensing observations (Mandelbaum et al. 2006). Note that a Salpeter initial mass function would increase the 'observed' conversion efficiency by approximately a factor of two (van Dokkum & Conroy 2010).

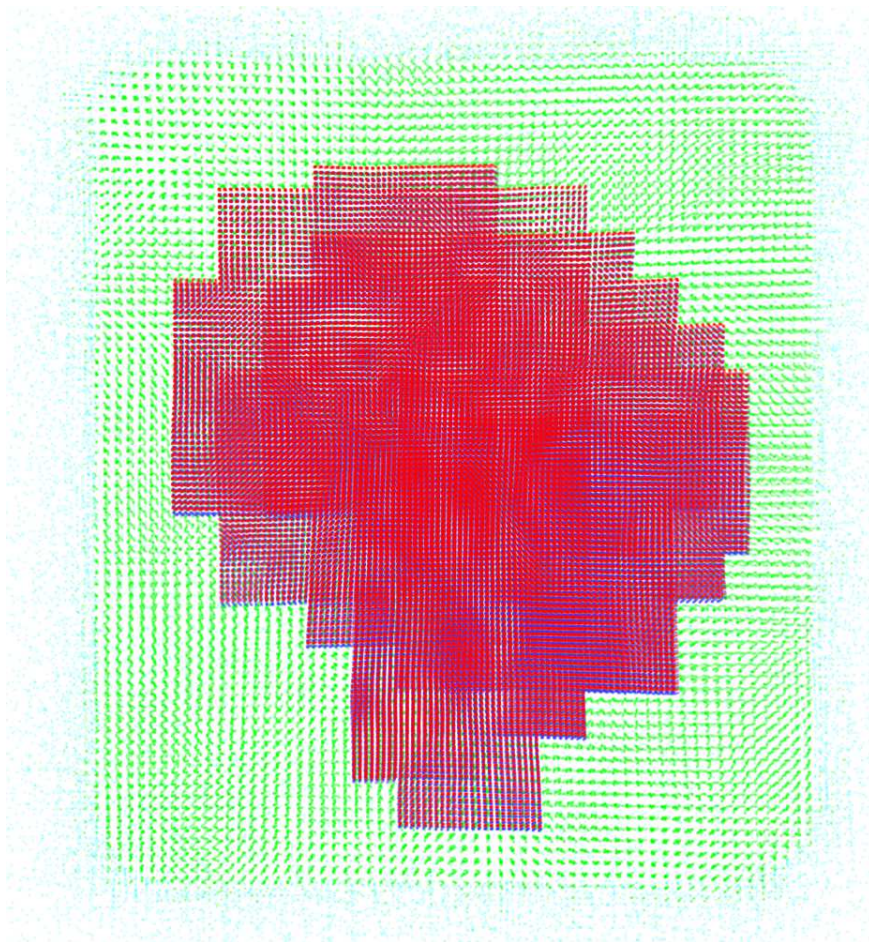


**Figure 4.3:** Central region of the initial conditions for halo #0408 at  $z=43$ . The innermost region consists of the high-resolution gas and dark matter particles (red and blue). The green particles are dark matter particles taken from the original dark-matter-only run. The outermost dark matter particles have increasing mass depending on the distance, with sufficient resolution to represent the long range tidal forces.

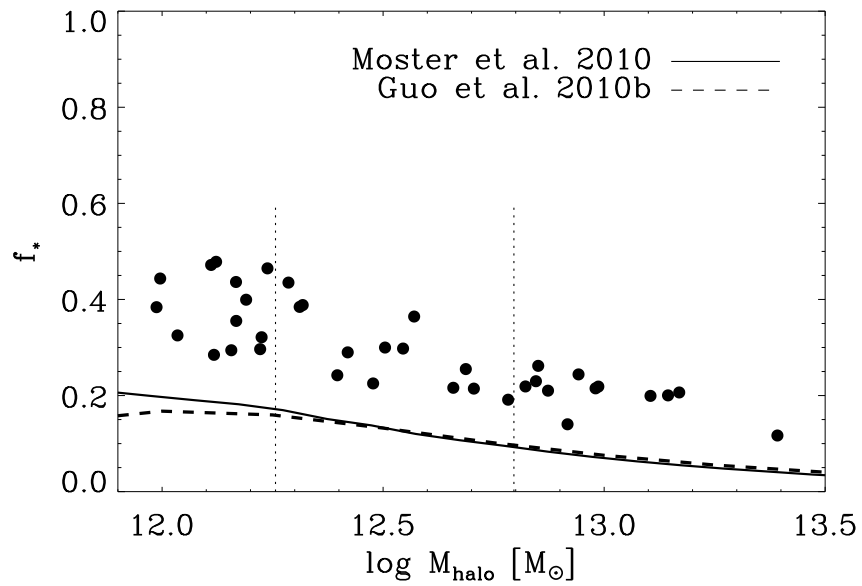


**Figure 4.4:** Fraction of baryons that is converted into stars at redshift zero. The vertical dotted lines indicate the separation into the different mass bins. The solid black line shows the results of Guo et al. (2010b), the dashed line those of Moster et al. (2010).

---

The physical processes probably responsible for this discrepancy are well studied and it has been argued that feedback from SNII is important for low mass systems (e.g. Larson 1974; Dekel & Silk 1986; Guo et al. 2010a) and feedback from supermassive black holes dominates for high mass systems (Croton et al. 2006; Di Matteo et al. 2008). Although this issue is relatively well understood and many idealized calculations have shown how these feedback processes can expel the baryons from galaxies, there have been only a few high resolution galaxy formation calculations, using cosmological initial conditions, beginning to master the physics well enough to match either the winds seen in forming galaxies or the final metal distribution between galaxies and the IGM (Scannapieco et al. 2008; Sawala et al. 2010). Some other calculations do successfully allow for winds and for the consequences these winds have on the galaxies and the surrounding ISM (Springel & Hernquist 2003; Oppenheimer & Davé 2008; Oppenheimer et al. 2010a; Cen & Chisari 2010; Wiersma et al. 2010a; McCarthy et al. 2010a). Our computations do not generate significant winds at high redshift (e.g. Steidel et al. 2010) and thus overestimate, by roughly a factor of two, the condensed baryon fraction of massive galaxies (Guo et al. 2010b; Moster et al. 2010). This becomes worse if we extend the sample to lower masses where the halo occupation models predict a sharp drop off the conversion efficiency  $f_*$ . This is probably due to the fact that ejective supernovae wind feedback, which is not included in the present study, is most effective in this regime. We are currently working to implement physically valid feedback implementations to address this problem.

# THE TWO PHASES OF GALAXY FORMATION

Cosmological simulations of galaxy formation appear to show a 'two-phase' character with a rapid early phase at  $z \gtrsim 2$  during which 'in-situ' stars are formed within the galaxy from infalling cold gas followed by an extended phase since  $z \lesssim 3$  during which 'ex-situ' stars are primarily accreted. In the latter phase massive systems grow considerably in mass and radius by accretion of smaller satellite stellar systems formed at quite early times ( $z > 3$ ) outside of the virial radius of the forming central galaxy. The importance of stellar accretion increases with galaxy mass and towards lower redshift. In our simulations lower mass galaxies ( $M_* \lesssim 9 \times 10^{10} M_\odot h^{-1}$ ) accrete about 60 per cent of their present-day stellar mass. High mass galaxy ( $M_* \gtrsim 1.7 \times 10^{11} M_\odot h^{-1}$ ) assembly is dominated by accretion and merging with about 80 per cent of the stars added by the present-day. In general the simulated galaxies approximately double their mass since  $z=1$ . For massive systems this mass growth is not accompanied by significant star formation. The majority of the in-situ created stars is formed at  $z > 2$ , primarily out of cold gas flows. We recover the observational result of 'archaeological downsizing', where the most massive galaxies harbor the oldest stars. We find that this is not in contradiction with hierarchical structure formation. Most stars in the massive galaxies are formed early on in smaller structures, the galaxies themselves are assembled late. The results presented in this chapter have been published in Oser et al. (2010).

Our understanding of galaxy formation has made great advances in the last two decades driven - primarily - by technological progress. Both ground and sky based measurements have allowed direct observation of various phases of galaxy formation and evolution over cosmic time with some detailed information now available at redshifts  $z > 2$  (e.g. Steidel et al. 1999; Pettini et al. 2001; Genzel et al. 2006; Förster Schreiber et al. 2006; Trujillo et al. 2007; Kriek et al. 2008; van Dokkum et al. 2008; Marchesini et al. 2009; Förster Schreiber et al. 2009). Simultaneously with a quite definite cosmological model ( $\Lambda$ CDM, e.g. Spergel et al. 2007, Komatsu et al. 2010) having gained wide acceptance, we can, with increasing accuracy, simulate the evolution of galaxies from realistic initial conditions, with numerical resolution (in mass, space, and time) and physical modeling approaching the necessary degree of refinement (e.g. Sommer-Larsen et al. 2003; Springel & Hernquist 2003; Springel 2005; Nagamine et al. 2005; Naab et al. 2007; Governato et al. 2007; Piontek & Steinmetz 2009; Scannapieco et al. 2009; Sawala et al. 2010; Agertz et al. 2010; Schaye et al. 2010)

The overall results are reassuring, with simulations and observations agreeing - in gross outline - as to the time evolution of star/galaxy formation (e.g. Nagamine et al. 2006; Schaye et al. 2009) as well as the global attributes of the galaxies such as luminosity distribution and spatial organization (e.g. Cen & Ostriker 1999; Kauffmann et al. 1999; Somerville & Primack 1999; Springel et al. 2005b; Kereš et al. 2009a; Guo et al. 2010a). Understanding the development of the internal structures of galaxies has been far more difficult to achieve with respect to the galactic stellar mass fractions (e.g. Kereš et al. 2009a; Guo et al. 2010b) as well as kinematics and morphologies (e.g. Abadi et al. 2003; Governato et al. 2010; Feldmann et al. 2010).

The terms with which we might usefully describe such development are still controversial (e.g. Meza et al. 2003; Naab et al. 2007; Governato et al. 2007; Piontek & Steinmetz 2009). In a hierarchically organized universe it has been natural to focus on overdense 'lumps' of dark matter gas or stars and to follow the merger history of these lumps. A recent paper by Hopkins et al. (2009a) shows how useful this picture can be. But this is not the only description of galaxy formation. For example Kereš et al. (2005, 2009b) and Dekel et al. (2009b) have focused on how convergent cold streams of gas lead to early star bursts and the formation of the cores of massive galaxies. Naab et al. (2007, 2009), Joung et al. (2009) and others have used high resolution hydro simulations to explore this phase in greater detail (see also Meza et al. (2005) for the accretion histories of stellar halos of disk galaxies).

One fundamental and useful distinction is to examine if a given star in the final galaxy was made (from gas) close to the center of the final system or, alternatively, near the center of some other, distant system and accreted in stellar form to the final galaxy. This distinction is useful, e.g. for understanding the size evolution of massive galaxies (Khochfar & Silk 2006a; Naab et al. 2007, 2009; Bezanson et al. 2009; Nipoti et al. 2009a; Hopkins et al. 2010b; Feldmann et al. 2010). In the simulations presented here we find that most stellar particles in massive galaxies are formed at high redshift either far inside the virial radius ( $\lesssim 3$  kpc) near the forming galaxy center or, alternatively in small systems outside the virial radius of the galaxy at a given cosmic time. We

---

characterize the first category of stars as made 'in-situ' and the second as accreted or formed 'ex-situ'. In-situ stars are made (by definition) near to the galactic center over an extended time period. They are made from dissipative gas and, for massive systems, probably have relatively high metallicity (Zolotov et al. 2010). The peak rate of star formation for this category may be relatively early and in fact is very early ( $z \approx 4$ ) for the most massive systems.

On the contrary, the accreted stars are typically made at quite early times as well, outside the virial radius, but added to the parent galaxy late in its evolution. They are added typically at radii larger than the effective radius,  $r > r_{\text{eff}}$ , and are expected to be metal poor, since they originated in lower mass, lower metallicity systems (Naab et al. 2009). The ex-situ stars accrete via an energetically conservative process and their final binding energy is transferred to other phases (gas, stars, and dark matter) rather than simply radiated away (Johansson et al. 2009b).

This alternative way of envisioning galaxy formation has many corollaries and makes many observed facts easier to understand. In massive systems we expect considerable growth in mass and radius at late times but little star formation, with the late forming stellar envelopes comprised of stars which are typically older than the stars in the bulk of the galaxy. Further we find systematic trends with galaxy mass. As one considers systems of lower mass, the in-situ component becomes increasingly dominant and the period of in-situ star formation is stretched out from being a small fraction of the Hubble time to a large fraction thereof.

This chapter is organized as follows. In section 5.1 we examine the dependence of the ratio of in-situ formed to accreted stars on the galaxy stellar mass along with its implications. We go on to analyze the half-mass radii of the different stellar components of our simulated galaxies in section 5.2. Finally, in section 5.3 we summarize our findings.

Table 5.1. Central Galaxies

ID	$m_{200}^1$	$r_{200}^2$	$m_*^3$	$m_{gas}^4$	$m_{ins}/m_*^5$	$t_*^6$	$t_{ins}^7$	$t_{acc}^8$	$t_{50}^9$	$n_{gas}^{10}$	$n_*^{11}$	$n_{halo}^{12}$
0040	2676	486	36.0	4.13	0.231	10.8	9.90	11.1	2.73	579933	440633	2096930
0069	1775	424	35.6	3.13	0.218	10.8	8.66	11.4	6.37	354378	306742	1378352
0089	1064	358	37.7	2.58	0.163	11.0	9.91	11.2	4.75	214528	182465	826895
0094	1004	351	34.5	3.46	0.258	10.9	9.10	11.6	7.67	210596	164402	780411
0125	917	340	31.2	2.94	0.224	11.1	9.59	11.6	8.31	200865	146889	716832
0162	630	300	26.2	2.64	0.129	10.8	8.49	11.2	2.58	134454	106554	494315
0163	689	309	25.3	1.73	0.150	10.5	9.11	10.8	4.75	139297	119486	536504
0175	699	311	26.5	1.29	0.270	11.3	9.74	11.8	9.56	127745	117170	530274
0190	511	280	22.7	1.71	0.146	10.3	8.39	10.6	3.81	103075	98844	405894
0204	538	285	19.3	1.42	0.156	10.8	8.77	11.2	8.31	102722	99548	419003
0209	595	295	14.4	0.656	0.337	10.9	9.71	11.5	9.26	118459	97601	457580
0215	505	279	19.9	1.14	0.352	11.0	9.93	11.5	8.15	100251	87072	391385
0224	478	274	17.9	2.06	0.200	10.3	7.69	11.0	6.20	89336	91799	373489
0259	437	266	14.3	1.23	0.262	10.9	8.98	11.6	9.72	83945	81751	341491
0300	365	250	13.4	1.63	0.201	10.4	8.64	10.8	5.88	72180	64276	283964
0329	350	247	15.4	0.696	0.341	10.9	9.55	11.6	9.10	65296	63583	270652
0380	328	242	12.3	0.634	0.491	10.9	10.0	11.8	10.6	58842	56464	249316
0408	253	221	12.8	1.90	0.300	10.1	7.09	11.3	8.31	49561	50348	200794
0443	268	226	16.6	1.91	0.277	10.3	6.55	11.7	8.31	50289	52800	210493
0501	230	215	11.7	0.93	0.361	10.8	10.0	11.2	8.79	48521	40463	181178
0549	216	210	8.38	0.450	0.262	10.7	8.71	11.4	9.41	39034	39605	165346
0616	189	201	9.38	0.455	0.367	10.6	9.88	11.0	9.72	34520	37188	147962
0664	179	197	7.48	0.558	0.343	10.7	9.06	11.6	9.41	34393	30862	138039
0721	147	185	9.63	0.629	0.536	8.88	7.07	11.0	6.69	22910	34776	116680

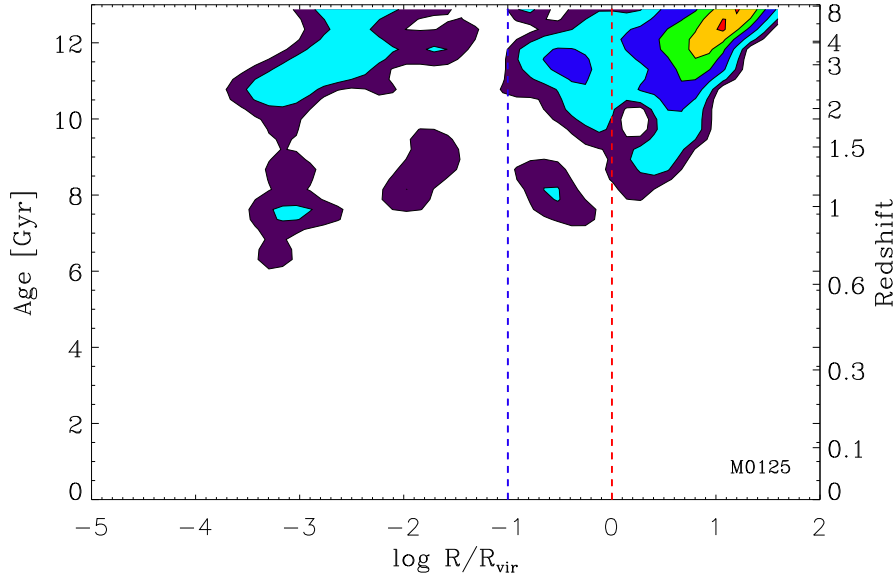


**Figure 5.1:** Stellar origin diagram for all stars within  $r_{10}$  at  $z = 0$  in galaxy M0125. Every grey dot indicates the time when a stellar particle was born and the distance, in units of the virial radius of the main galaxy at that time, where it was born. The contours enclose 90% (purple), 80% (turquoise), 60% (blue), 40% (green), 25% (orange) and 10% (red) of the stars, respectively. The blue and red vertical lines show the virial radius and 10% of the virial radius, respectively. There is a clear distinction between stars initially formed in the galaxy and those formed outside the galaxy and are accreted later on (78 percent of all stars).

## 5.1 The two phases of galaxy formation

The stellar particles ending up in the simulated galaxies at  $z = 0$  are of two different origins. Some fraction of the stars are made in-situ, within the galaxies, from accreted gas and some fraction of the stars are made ex-situ outside the galaxies and are accreted later on (Naab et al. 2007; Johansson et al. 2009b). The relative amount of in-situ and ex-situ stars is found to vary systematically with galaxy mass. Two typical stellar origin diagrams indicating this behavior are shown in Fig. 5.1 and Fig. 5.2.

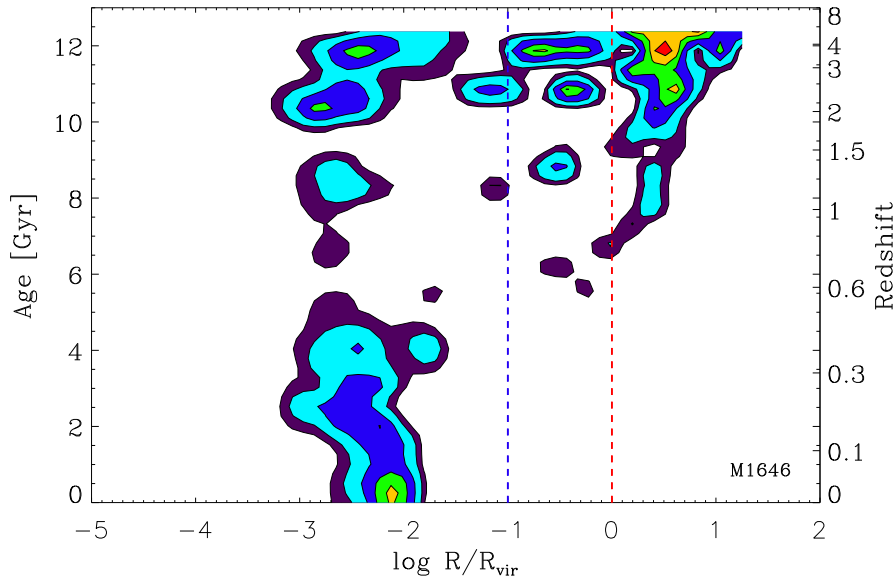
To construct these diagrams we follow every star that ends up within 10% of the present-day virial radius of a simulated galaxy back in time. We use 10% of the virial radius,  $r_{10}$ , as a fiducial value for the extent of the stellar component of a simulated final galaxy inside its dark matter halo. Then we mark the time when a star was born as well as its distance from the galaxy center in units of the virial radius (at this time) with a grey dot. The values are discrete in time representing the discrete snapshots. The contours in these plots encompass the smallest number of bins that include 10, 25, 40, 60, 80 and 90 per cent of the stars, respectively. In Fig. 5.1 we show the stellar origin

Table 5.1—Continued

ID	$m_{200}^1$	$r_{200}^2$	$m_*^3$	$m_{gas}^4$	$m_{ins}/m_*^5$	$t_*^6$	$t_{ins}^7$	$t_{acc}^8$	$t_{50}^9$	$n_{gas}^{10}$	$n_*^{11}$	$n_{halo}^{12}$
0763	150	186	9.85	0.177	0.197	10.4	9.19	10.8	6.37	25283	34151	119180
0858	139	181	10.3	0.790	0.355	8.92	5.49	10.8	6.69	21022	33759	110365
0908	125	175	9.67	0.708	0.458	8.84	6.55	10.8	7.50	19927	33080	102025
0948	121	173	6.64	0.442	0.308	10.6	9.38	11.2	9.56	22627	23147	94475
0959	120	173	6.05	0.399	0.371	10.1	9.46	10.5	9.41	23591	23027	94670
0977	94.4	159	4.55	0.464	0.496	9.10	7.21	11.0	8.63	16592	20916	75143
1017	106	166	6.39	0.736	0.584	10.0	8.92	11.5	9.87	21049	20634	83999
1061	103	164	5.18	0.439	0.335	9.98	8.72	10.6	8.15	19196	20400	81076
1071	106	166	7.79	0.610	0.317	9.66	7.06	10.9	8.15	18696	24045	84818
1091	112	169	7.53	0.416	0.280	9.24	5.37	10.7	6.20	18487	26210	89119
1167	93.0	159	7.37	0.659	0.331	9.32	5.88	11.0	6.85	15966	22371	75141
1192	78.0	150	4.36	0.157	0.442	10.4	9.54	11.0	9.56	13041	15792	60404
1196	95.4	160	7.73	0.99	0.490	9.23	6.96	11.4	7.67	16839	20987	75883
1646	71.3	145	5.38	0.509	0.480	8.90	6.23	11.4	8.31	11143	16557	56264
1859	70.0	144	4.52	0.340	0.429	9.82	7.86	11.3	9.56	12355	16458	56488

Note. — all masses in units of  $10^{10}h^{-1}M_{\odot}$ , timescales in Gyr.  $v_{10}$  in kpc/h,  $m_{*}$  stellar mass inside  $r_{10}$ ,  $m_{gas}$  gas mass inside  $r_{10}$ ,  $m_{ins}/m_*$  ratio of in-situ to ex-situ created stars,  $t_*$  mean stellar age,  $t_{ins}$  mean stellar age of in-situ created stars,  $t_{acc}$  mean stellar age of ex-situ created stars,  $t_{50}$  lookback time where 50 per cent of the final stellar mass is in place,  $n_{gas}$  number of gas particles inside  $r_{200}$ ,  $n_*$  number of star particles inside  $r_{200}$ ,  $n_{halo}$  total number of particles inside  $r_{200}$ .

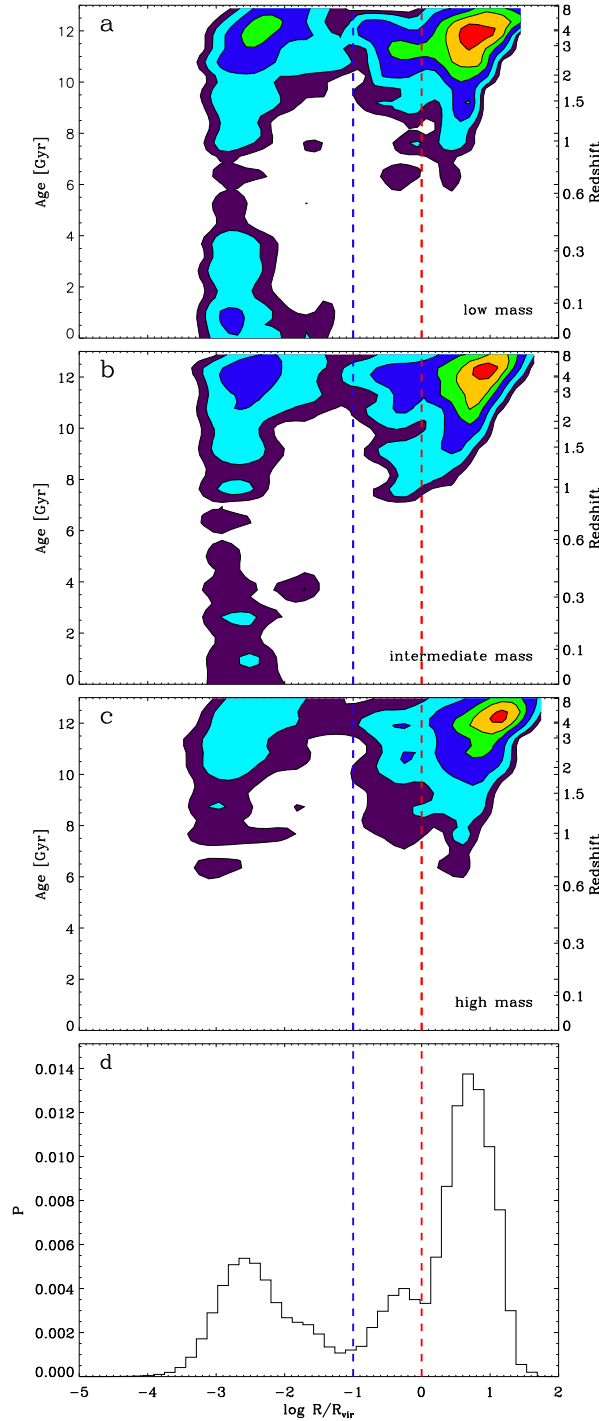
The horizontal bars indicate the separation into small, intermediate and high mass galaxies used throughout this chapter



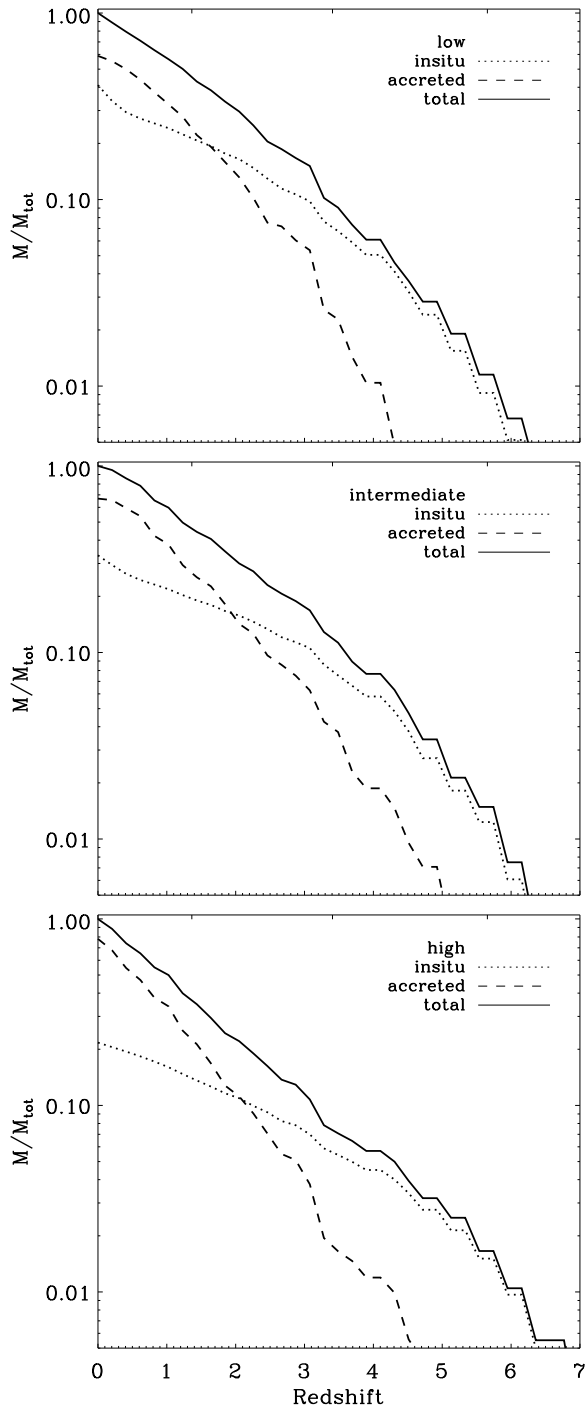
**Figure 5.2:** Same as Fig. 5.1 but for the low mass galaxy M1646. There is significant in-situ star formation at the center even at low redshift and significantly less accretion of stars. In this case only 52 per cent of the stars are accreted.

diagram for a massive system with a halo mass of  $\sim 10^{13} M_{\odot} h^{-1}$ . At redshifts  $z > 2$  there are two separate peaks of star formation: one inside  $r_{10}$ , which is in-situ star formation and another one outside the virial radius of the system at that time. This indicates that a significant fraction of the stars in the present-day galaxy was made outside the galaxy and has been accreted later on. For this system the in-situ star formation decreases towards lower redshifts. Although there is ongoing star formation until  $z=0$  the contribution to the final galaxy is negligible, since the contoured regions include 90 per cent of all stars in the galaxy. For a lower mass system with a halo mass of  $7.1 \times 10^{11} M_{\odot} h^{-1}$  the same analysis is shown in Fig. 5.2. In this case the fraction of stars forming ex-situ is lower and the contoured regions extend up to the present day, i.e. in-situ star formation continues at a significant level towards lower redshift.

In Fig. 5.3, we have stacked all simulated galaxies of our sample into three mass bins (indicated by the horizontal bars in table 5.1) with the same number of objects (13), every star particle is weighted according to the total number of stars in its host galaxy, so that every galaxy has an equal weight. The low mass bin contains galaxies with halo masses in the range  $7.0 \times 10^{11} - 1.3 \times 10^{12} M_{\odot} h^{-1}$  (panel a), intermediate mass galaxies have  $1.3 \times 10^{12} - 4.5 \times 10^{12} M_{\odot} h^{-1}$  (panel b) and high mass galaxies have  $4.5 \times 10^{12} - 2.7 \times 10^{13} M_{\odot} h^{-1}$  (panel c). These plots again demonstrate in a more statistical sense that the stars ending up in the final galaxies form in two distinct phases, namely in-situ in the galaxy and ex-situ outside the virial radii of the galaxies



**Figure 5.3:** Same as Fig. 5.1 but for all galaxies in low mass halos in the mass range  $7.0 \times 10^{11} - 1.3 \times 10^{12} h^{-1} M_{\odot}$  (panel a), for intermediate halo masses in the range  $1.3 \times 10^{12} - 4.5 \times 10^{12} h^{-1} M_{\odot}$  (panel b), and for all high mass halos with  $4.5 \times 10^{12} - 2.7 \times 10^{13} h^{-1} M_{\odot}$  (panel c). The contours show the same percentiles as in Figs. 5.1 and 5.2. The stars form in two phases, either inside  $r_{10}$  or outside  $r_{\text{vir}}$  as can be seen in panel d. Galaxies in low mass halos have ongoing in-situ star formation (see Fig. 5.6) at relatively high specific rates until the present day, whereas in the highest mass group most star formation is complete by  $z=2$ .



**Figure 5.4:** Stellar mass assembly histories (solid lines) for low mass (top), intermediate mass (middle) and high mass (bottom) galaxies. The assembly is separated into in-situ stars (dotted line) and ex-situ stars that are accreted onto the galaxy later on (dashed line). The assembly of higher mass galaxies is more dominated by in-situ formation at high redshift, however, the total fraction of accreted stars by  $z=0$  is higher ( $\approx 80\%$ ) for massive systems than for low mass systems ( $\approx 60\%$ ).

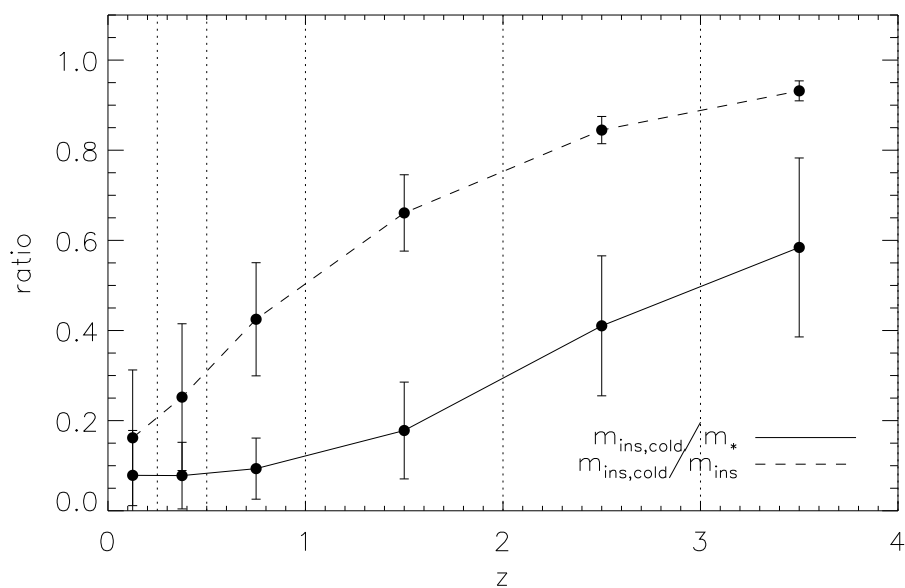


**Figure 5.5:** Average ratio of in-situ created stars that formed inside the bins indicated by the vertical dotted lines out of gas that was accreted cold to the total mass of in-situ created stars (dashed line). The solid line shows the ratio of the stars created in-situ out of cold gas to the total stellar mass growth, this includes in-situ star formation as well as accretion. The error bars correspond to the  $1\sigma$ -dispersion.

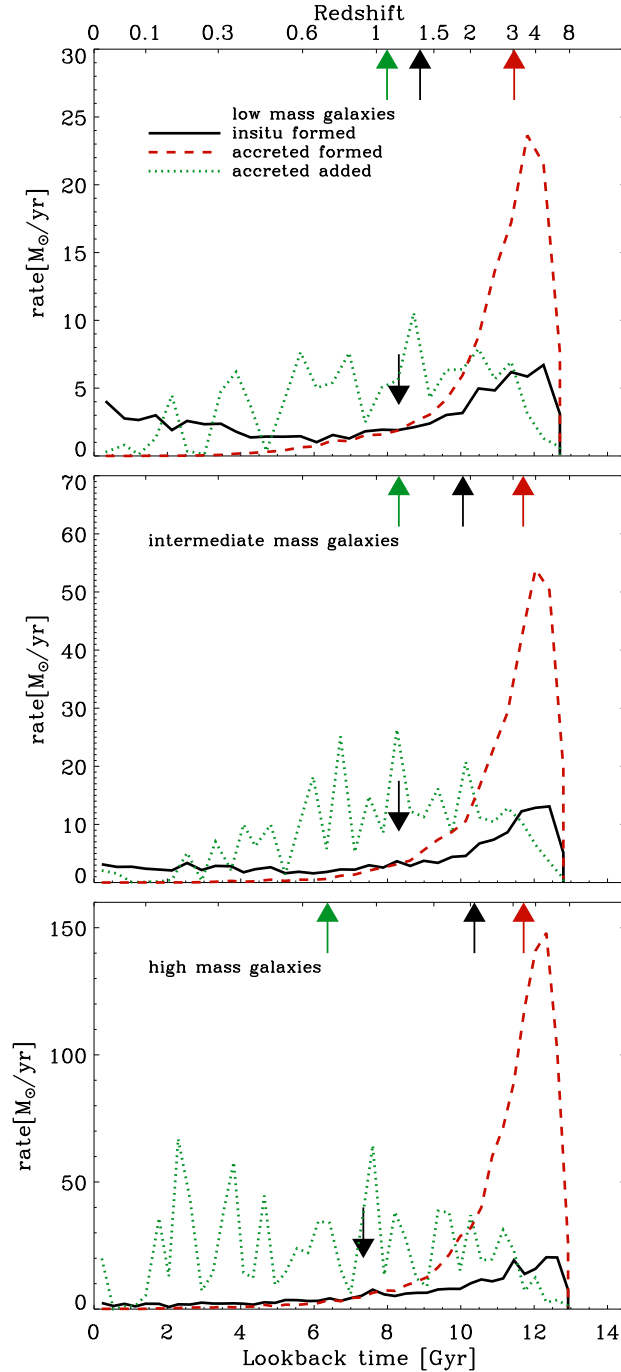


**Figure 5.6:** Star formation histories for low mass (upper panel), intermediate mass (middle panel) and high mass galaxies (lower panel) for all stars that end up inside the galaxy at  $z = 0$ . The solid black line shows the formation of the in-situ created stars, the red dashed line the formation of the ex-situ stars and the green dotted line shows the accretion rate of the ex-situ stars onto the galaxy. The arrows on top indicate the time at which half the stars are formed/added. The arrow at the bottom indicates the time at which 50% of the final galaxy mass is assembled.

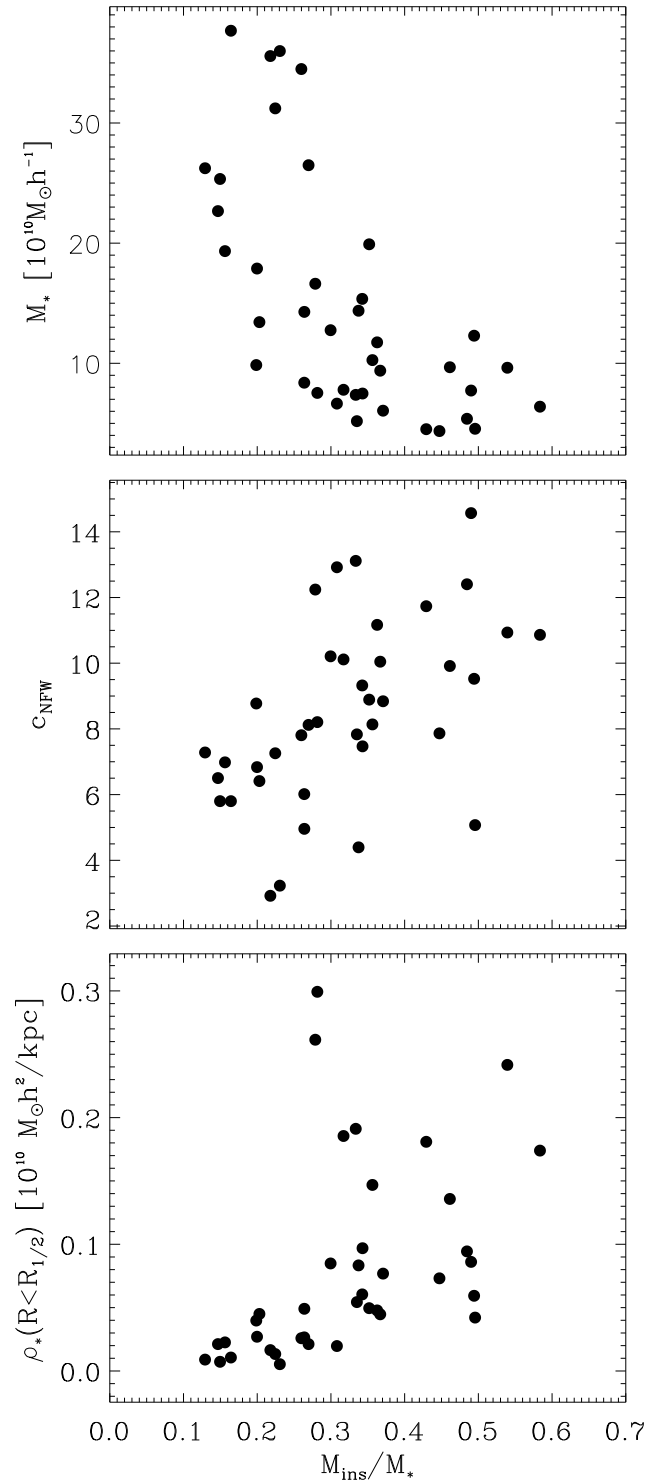


**Figure 5.7:** From top to bottom: Fraction of in-situ stellar mass vs total stellar mass inside  $r_{10}$ , halo concentration and stellar density inside  $R_{1/2}$  at  $z = 0$ . There is a clear trend that galaxies with less in-situ star formation are more massive, have less concentrated halos and lower density central regions.

(red vertical dashed lines). The spatial division line between these two phases of star formation is at about 10% of the virial radius indicated by the vertical blue dashed lines in Fig. 5.3. In addition, there is a clear trend that low mass galaxies have relatively more in-situ star formation at low redshift  $z < 1$  than higher mass galaxies. For the most massive galaxies the contribution from late in-situ star formation is relatively small. Panel d shows a histogram for the formation radii for all stars in all simulations. For this analysis we use 45 logarithmically evenly spaced bins. We see two peaks, for the in-situ created stars at  $\log(r/r_{\text{vir}}) \approx -2.5$  and for the ex-situ created stars at  $\log(r/r_{\text{vir}}) \approx 0.6$ , respectively. A third peak appears between  $r_{10}$  and  $r_{\text{vir}}$  that is due to infalling substructure that is still star-forming.

In Fig. 5.4 we show the average mass accretion histories for the stellar particles in the three mass bins separated into in-situ and ex-situ/accreted stars depending on whether they have formed inside or outside 10% of the virial radius. The galaxy growth is dominated for all three mass bins by in-situ star formation until  $z \approx 2$ , when the mass of accreted stars equals the mass of in-situ stars. By  $z = 0$  about  $41 \pm 9\%$  (we give mean values and the  $1\sigma$ -dispersion of the 13 galaxies) of the stars in the low mass sample (top panel) have formed in-situ, the rest were accreted. For the intermediate mass galaxies (middle panel) the fraction of in-situ stars is lower than for the low mass sample of  $\approx 33 \pm 10\%$ , and  $67\%$  of the stars were accreted. With  $78 \pm 7\%$  the fraction of accreted stars is even higher for the massive galaxies. On average only  $22\%$  of the present-day stellar mass is formed in-situ which is the dominant mode until  $z \approx 2$  but thereafter contributes very little to the stellar mass growth.

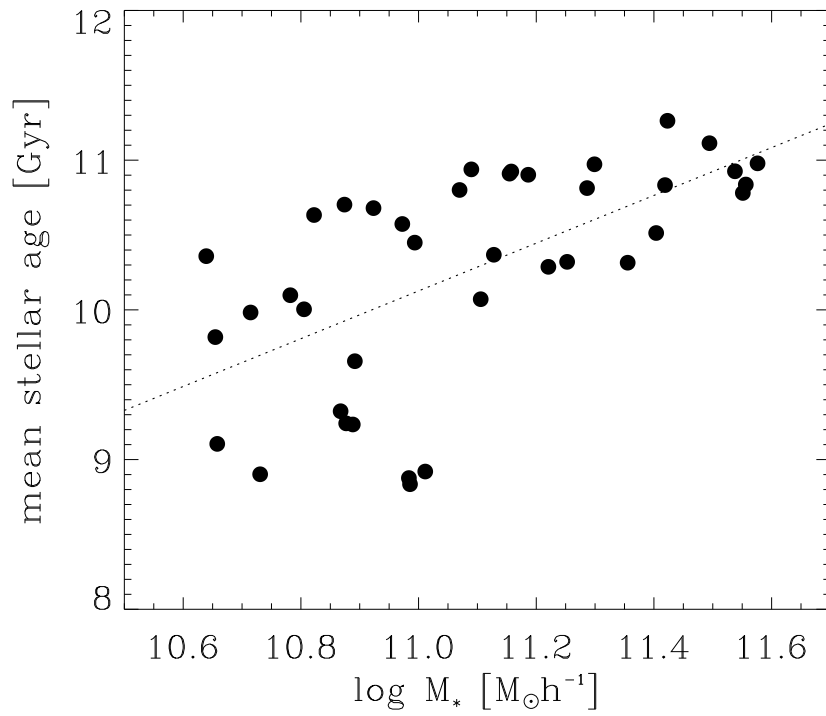
Following Kereš et al. (2005) and Kereš et al. (2009a) we examined whether the gas out of which the in-situ stars are formed in our galaxies was ever heated above  $T_{\text{hot}} > 2.5 \times 10^5 K$  throughout the simulation. The results can be seen in Fig. 5.5. The dashed line shows, that up to redshift 2, where in-situ star formation is still dominating over accretion, almost all of the in-situ stars are formed out of gas that was accreted cold. Only at later times ( $0 < z < 2$ ), when stellar accretion is the primary source of stellar mass growth, in-situ stars are forming out of cooling hot halo gas. At lower redshift the contribution of in-situ star formation out of cold flows to the total stellar mass growth becomes almost negligible (dotted line in Fig. 5.5). The interpretation of the results does not change when we instead of a fixed temperature cut use a temperature threshold related to the current halo virial temperature (see Kereš et al. (2005)). This is in agreement with the previous results of numerical simulations (Kereš et al. 2009a) and analytical predictions (Dekel & Birnboim 2006) that galaxy growth at high redshift ( $z \geq 2$ ) is dominated by cold accretion.

Fig. 5.6 illustrates the star formation and assembly histories for the galaxies in the three mass bins. The red dashed line shows the archaeological star formation history of the accreted stars computed from the mass weighted ages of the accreted stars at the present day. All curves show a steep increase towards the peak at  $z \approx 4$  at values of  $\approx 25M_{\odot}yr^{-1}$ ,  $\approx 55M_{\odot}yr^{-1}$ , and  $\approx 150M_{\odot}yr^{-1}$  for the low, intermediate and massive bin, respectively. This is followed by an approximately exponential decline towards  $z = 0$ . The red arrow on top indicates the time when half of the accreted stars are

formed. In all cases, i.e. at all masses this is at  $z \approx 3$ . The green dotted line shows when these stars are accreted onto the galaxies. As this happens in mergers, the curves show peaks. On average the rates increase towards  $z = 2$  and then stay relatively flat with average rates of  $\approx 3.6M_{\odot}yr^{-1}$ ,  $\approx 8.2M_{\odot}yr^{-1}$ , and  $\approx 17M_{\odot}yr^{-1}$ . The green arrow on top indicates when half of the present-day mass in ex-situ stars is accreted onto the galaxies. This happens around  $z=0.7-1.2$  and therefore significantly later than the formation of these stars at  $z=3-4$ . The black solid line shows the formation history of the in-situ stars in the galaxies. This is most closely related to the star formation rate that would actually be observed in these galaxies. All curves peak at  $z \geq 3.5$  at rates between  $\approx 5$  and  $\approx 20M_{\odot}yr^{-1}$ . Independent of galaxy mass all rates drop to  $\approx 2 - 3M_{\odot}yr^{-1}$  at  $z = 1$  and stay constant to the present day similarly to the observations of massive galaxies by Juneau et al. (2005). This results in a specific star formation rate of  $0.31 \pm 0.15$ ,  $0.18 \pm 0.15$  and  $0.053 \pm 0.071 \times 10^{-10}yr^{-1}$  for the different mass bins. According to the definition by Franx et al. 2008 ( $SFR/m_* < 0.3/t_{thub}$ ) the galaxies in the high mass bin would correspond to quiescent galaxies. The time when half of the in-situ stars are formed is indicated by the top black arrows. This changes systematically with galaxy mass from  $z=1.4$  to  $z=1.9$  and  $z=2.1$ , i.e. the in-situ component is oldest for the most massive systems. The black arrow at the bottom of the panels indicates the time when half of the final galaxy was assembled. For all galaxies this is around redshift  $z \approx 1$ . Therefore all galaxies double their mass since then. For low mass systems the low redshift growth is dominated by in-situ formation whereas for high mass systems it is dominated by accretion of small stellar systems (Tiret et al. 2011).

In summary, at high redshift the assembly of galaxies at all masses is dominated by in-situ star formation fed by cold flows. The larger the galaxy mass the smaller is the late contribution of in-situ star formation. At low redshift,  $z < 1$ , the growth of low mass galaxies continues by in-situ star formation and stellar accretion whereas, massive galaxies grow predominantly by accretion of ex-situ stars (see e.g. Feldmann et al. 2010; Naab et al. 2009).

In Fig. 5.7 we show interesting correlations of galaxy and halo properties with the fraction of in-situ stars indicating that this quantity is an important tracer of galaxy assembly. Essentially, this ratio,  $m_{ins}/m_*$ , is a dimensionless measure for the degree to which the galaxy was formed by a dissipational versus a dissipationless process (Lackner & Ostriker 2010). The fraction of the stellar galaxy mass formed in-situ  $m_{ins}/m_*$  is highest, up to 60%, for low mass galaxies and declines almost linearly (despite some scatter) with increasing galaxy mass down to  $\approx 13\%$  for the most massive systems in our simulations which are the central galaxies of massive groups (top panel of Fig. 5.7). This trend is very similar to semi-analytical predictions (Khochfar & Silk 2006a) and constraints based on halo occupation models combined with isolated merger simulations (Hopkins et al. 2009c). In the central panel of Fig. 5.7 we show the fraction of in-situ mass versus the concentration parameter  $c$  of the dark halo which is defined as the ratio between  $r_{200}$  and  $r_s$ , where  $r_s$  is the scale radius for an NFW fit (Navarro et al.



**Figure 5.8:** Mean age of the stars inside  $r_{10}$  as function of galaxy mass. High mass galaxies consist of older stars than the low mass galaxies, recovering the phenomenon usually referred to as 'archaeological downsizing' ( $t_{mean} \propto \log M_*^{1.6}$ ).

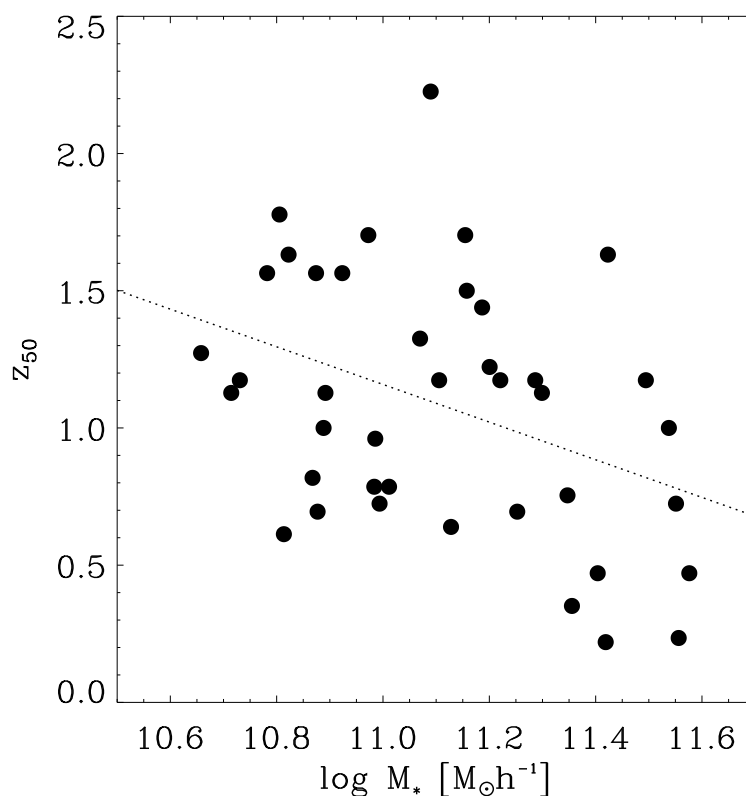


**Figure 5.9:** Redshift when the galaxies have assembled 50% of their present-day stellar mass as function of galaxy mass at redshift zero. Although the stars in the massive galaxies are typically older (see Fig. 5.8) there is a trend that the massive galaxies are assembled later ( $z_{50} \propto \log M_*^{-3.3}$ ). This is consistent with the global picture of hierarchical structure formation.

1997) of the density profile:

$$\rho(r) = \frac{\delta_c \rho_{crit}}{(r/r_s)(1 + r/r_s)^2} \quad (5.1)$$

For the fit we binned the halo into 32 spherical shells equally spaced in  $\log_{10}(r)$  between  $r_{200}$  and  $\log_{10}(r/r_{200}) = -2.5$  similar to Grossi & Springel (2009). We see a continuous change of the dark matter halo concentration. As expected from the effect of adiabatic contraction galaxies with significant in-situ star formation, i.e. more dissipation, live in more concentrated halos (Blumenthal et al. 1986; Dubinski 1994; Jesseit et al. 2002; Debattista et al. 2008; Gnedin et al. 2004; Abadi et al. 2010; Auger et al. 2010). The concentration of more massive halos does not increase significantly as the matter is added predominantly in stellar form and cannot dissipate (see e.g. Johansson et al. 2009b and references therein), i.e. the adiabatic contraction approximation cannot be applied for massive galaxies. The bottom panel in Fig. 5.7 shows the stellar density inside the spherical half-mass radius versus the ratio of in-situ created stars of the galaxies. The two properties are correlated in the sense that galaxies with a large fraction of accreted stars have lower central densities, a well known property of elliptical galaxies (e.g. Bender et al. 1992).

Fig. 5.6 gives a clue to the paradox of 'downsizing'. The initial expectation was that in a hierarchical universe, since more massive halos statistically are formed later than less massive ones, the same should be true of galaxies. But we know that this is not true observationally (Nelán et al. 2005), giant ellipticals are older - not younger - than lower mass systems (see e.g. Thomas et al. 2005). Our simulations give the same result as can be seen from Fig. 5.8, the most massive systems are made out of the oldest stars. The inclusion of galactic winds would probably lead to less efficient star formation at high redshifts and leave more gas for late in-situ star formation especially in the lower mass systems, rendering these galaxies even younger. This would lead to an even steeper relation than the one shown in Fig. 5.8. The explanation of the paradox is obvious: The accreted stars are typically made in smaller systems and these small systems are in fact made at early times (dashed red curves in Fig. 5.6). Massive galaxies are more dominated by the accreted stars and so by  $z=0$  they contain primarily old stars, although the galaxies themselves are assembled late. This effect can be seen in Fig. 5.9, here we show the redshift at which for the first time 50% of the final stellar mass is assembled in the most massive progenitor as a function of the present-day galaxy mass. We find that the most massive systems actually form last as predicted by the bottom-up structure formation paradigm. De Lucia et al. 2006 obtain the same result with their semi-analytic model. This way the expectation from hierarchical structure formation is satisfied. Both our simulations and the observations of van Dokkum et al. (2008) agree: even at late times massive galaxies continue to grow in mass and size.

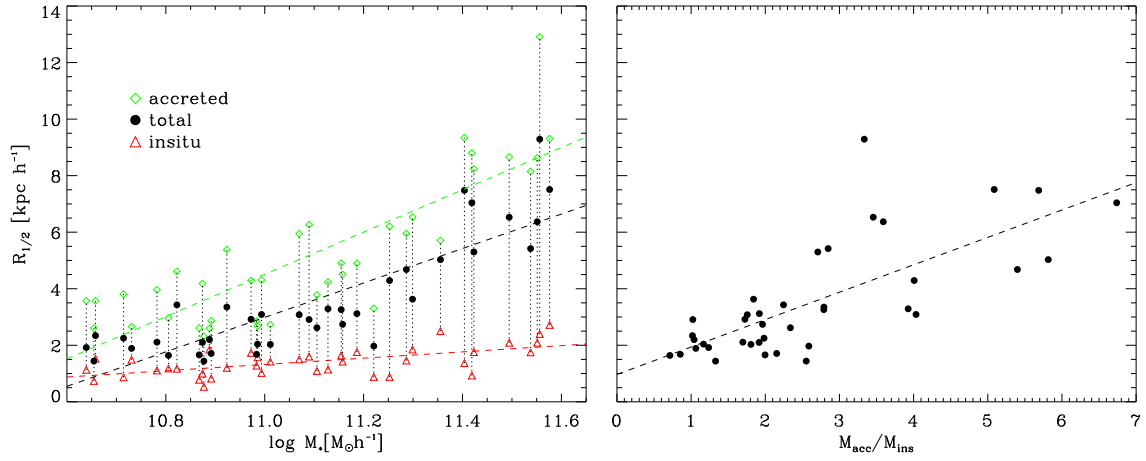


**Figure 5.10:** *Left panel:* Stellar mass inside 10% of the virial radius vs. spherical half-mass radius of accreted (green diamonds), in-situ (black triangles) and all stars (red squares), respectively. The dashed lines show the results of a linear fit for the respective components ( $r_{1/2} \propto \log M_*^\alpha$ , with  $\alpha = 7.5, 6.1$  and  $1.1$  for the accreted, total and in-situ stars, respectively). While the half-mass radius of the accreted stars strongly increases with mass, the half-mass radius of the in-situ formed stars shows only a weak dependence on galaxy mass. The mass-size relation is driven by the accreted stars. *Right panel:* This plot shows the spherical half-mass radii of the galaxies as a function of the ratio of accreted to in-situ created stars. The size increase of the galaxies is roughly linear dependent on this ratio ( $r_{1/2} \propto 0.97 * M_{acc}/M_{ins}$ ).

**Table 5.2:** The assembly of stars in massive galaxies

	In-situ	Accreted
<b>Epoch</b>	$6 \gtrsim z \gtrsim 2$	$3 \gtrsim z > 0$
<b>Baryonic mass source</b>	cold gas flows	minor & major mergers
<b>Size of region</b>	$r_{1/2} \approx 2\text{kpc}$	$r_{1/2} \approx 7\text{kpc}$
<b>Energetics</b>	Dissipational	Conservative

## 5.2 Galaxy sizes

The left panel of Fig. 5.10 shows the present-day spherical half-mass radius for the different components of our galaxies. The size of the in-situ component shows a very weak trend with galaxy mass. For the low mass galaxies the half-mass radii of the in-situ and the accreted stars are of similar size. While the in-situ component does not get larger than  $\approx 3\text{kpc } h^{-1}$ , the half-mass radius of the accreted stars is strongly increasing with galaxy mass and since the fraction of accreted stars rises with galaxy mass as well, the global half-mass radius of the galaxies follows this trend. In our simulations the majority of the in-situ created stars are formed in the bulges of the galaxies. Stronger feedback mechanism would probably lead to more star formation in galactic disks resulting in larger radii of the in-situ component. The half-mass radius of the accreted stars should not be affected by this. The right panel of Fig. 5.10 shows the galaxy radii versus the ratio of accreted to in-situ created stars. We find an almost linear trend. Fig. 5.10 shows, that stellar accretion is the dominant mechanism for the size growth of massive galaxies. For most of our systems the accretion of stars is significant at low redshifts, as seen in Fig. 5.6, especially for the high mass galaxies. Half of the total accreted stellar mass is added to the galaxies between redshift one and the present day which leads to considerable size increase at late times. Consistent with this pictures are the observations from e.g. van Dokkum et al. (2008) and others that show a significant growth between redshift  $z = 3$  and  $z = 0$  for quiescent early type galaxies. A detailed analysis of this effect will be presented separately. We give, in Naab et al. (2009) a simple argument based on the virial theorem showing how late accretion of low mass satellites ('minor mergers') will lead to the rapid growth in galactic size.

## 5.3 Summary and Discussion

We present results from 39 cosmological re-simulations of dark matter halos including gas and star formation covering a mass range of almost two orders of magnitude in virial mass. In the study presented here we used the simulations to investigate fundamental formation and assembly processes, i.e. how and when do galaxies get their gas and stars, and how does this influence the present day galaxy properties.

We have shown that it can be useful, at a very basic level, to distinguish between

stars that are created inside the galaxies themselves (in-situ) and those that are created outside (ex-situ) and are accreted later on. The division into these two separate phases is quite clean (see Fig. 5.3) with the in-situ stars typically formed closer than  $r/r_{vir} \sim 10^{-1}$ , i.e. within the galaxy, and the ex-situ stars formed outside the galaxy at  $r/r_{vir} \sim 10^{0.5}$  to 10. Independent of galaxy mass we find that the formation of the accreted stars peaks at redshift  $z \approx 4$ . The in-situ star formation as well has an early peak but extends over a longer period of time. The ratio of stars that are created in-situ to the accreted stars, however varies strongly for galaxies of different masses. We find that for massive galaxies ( $\sim 1.9 - 3.6 \times 10^{11} h^{-1} M_{\odot}$ ) the contribution of in-situ and accreted stars becomes comparable early ( $z \approx 2$ ) and the accreted stars can account for up to 87% of the final stellar mass. The lower mass galaxies ( $\sim 4 - 10 \times 10^{10} h^{-1} M_{\odot}$ ) still can have a high fraction of in-situ formed stars up to 60% at the present day. They show a significant amount of in-situ star formation throughout the whole simulation time. The large difference in time when those accreted stars are actually formed and when they are finally assimilated by their host, together with the trend shown of the ratio of in-situ formed stars explains the phenomenon of 'downsizing' (see also (De Lucia et al. 2006) for semi-analytical simulations). The more massive galaxies consist mainly of accreted and therefore old stars leading to the dependence of mean stellar age to galaxy mass shown in Fig. 5.8. The massive galaxies in our sample assemble about half their mass below a redshift of  $z=1$ . This mass increase, caused by stellar accretion and merging, is not accompanied by significant star formation, can be a significant contribution to the observed increase of stellar mass in the early-type galaxy population since  $z=1$  (see e.g. Brown et al. 2007; Faber et al. 2007).

We find that the accreted stars are primarily responsible for the low redshift size increase in massive galaxies (see e.g. Hyde & Bernardi 2009). When looking at the half-mass radii of the galaxies and the half-mass radii of the in-situ created and accreted components, we find that the half-mass radius of the in-situ created stars is only weakly dependent on the galaxy mass and is quite small ( $\lesssim 3 \text{ kpc } h^{-1}$ ). This component forms at redshift  $z > 2$  and makes the compact cores of the galaxies (see e.g. van Dokkum et al. 2008 and references therein). The larger sizes of galaxies with larger mass are mainly due to the accreted stars creating an outer envelope with half-mass radii exceeding  $8 \text{ kpc } h^{-1}$ .

Our simulations overestimate the stellar mass of the galaxies by roughly a factor of 2. This is probably due to the lack of ejective and preventive feedback mechanism in our simulations. The stars that are accreted as well as the early formed in-situ stars are generated in small systems where winds are most effective and lead to lower star formation rates and therefore lower accretion rates at lower redshifts. The late in-situ star formation should be diminished by AGN feedback particularly in the massive systems. It will be worthwhile to investigate whether and how the inclusion of those processes could influence the presented balance of in-situ star formation to stellar accretion.

The description of galaxy formation as a two phase process followed in a seemingly natural way from our detailed hydro simulations and is organized into a coherent

scheme in Table 5.2. It is not intended as a rival to other ways of seeing galaxy formation but rather as a framework within which the physical processes can be understood in a straightforward way. Early, in-situ star formation is clearly similar to that resulting from the 'cold flow' picture (Dekel et al. 2009a; Kereš et al. 2005) or the earlier descriptive term 'dissipative collapse'. In fact the in-situ phase bears an uncanny resemblance to the 'monolithic collapse' model (Eggen et al. 1962; Partridge & Peebles 1967; Larson 1969; Searle et al. 1973; Larson 1975). The late assembly phase of massive galaxies has many aspects similar to the 'dry merger' paradigm investigated by many authors (Khochfar & Burkert 2003; Khochfar & Silk 2006b; Naab et al. 2006; van der Wel et al. 2009; Bezanson et al. 2009; Nipoti et al. 2009b) with the added qualification that most of the accreted stellar systems are low in mass compared to the final assembled i.e. minor mergers dominate. There appears to be recent archaeological (Coccatto et al. 2010) and direct observational for this scenario. van Dokkum et al. (2010) conclude that massive compact galaxies at  $z=2$  (the end of the in-situ phase) have increased their mass at radii  $r > 5kpc$  by a factor of  $\approx 4$  since  $z=2$  with the mass at smaller radii being essentially unchanged.



# SIZE AND VELOCITY DISPERSION EVOLUTION OF MASSIVE EARLY-TYPE GALAXIES

The results presented in this chapter are drawn from the 40 most massive halos, that have been re-simulated for this work. We analyze the individual massive central galaxies with present-day stellar masses of  $M_* > 6.3 \times 10^{10} M_\odot$  forming in the simulations, in order to investigate the physical origin of the observed strong increase in galaxy sizes and the decrease of the stellar velocity dispersions since redshift  $z \approx 2$ . At present 25 out of 40 galaxies are quiescent with structural parameters (sizes and velocity dispersions) in agreement with local early type galaxies. At  $z=2$  all simulated galaxies with  $M_* \gtrsim 10^{11} M_\odot$  (11 out of 40) at  $z=2$  are compact with projected half-mass radii of  $\approx 0.77 (\pm 0.24)$  kpc and line-of-sight velocity dispersions within the projected half-mass radius of  $\approx 262 (\pm 28) \text{ kms}^{-1}$  (3 out of 11 are already quiescent). Similar to observed compact early-type galaxies at high redshift the simulated galaxies are clearly offset from the local mass-size and mass-velocity dispersion relations. Towards redshift zero the sizes increase by a factor of  $\sim 5 - 6$ , following  $R_{1/2} \propto (1+z)^\alpha$  with  $\alpha = -1.44$ . The velocity dispersions drop by about one-third since  $z \approx 2$ . On average, the dominant accretion mode is stellar minor mergers with a mass-weighted mass-ratio of 1:5. We therefore conclude that the evolution of massive early-type galaxies since  $z \approx 2$  and their present-day properties are predominantly determined by frequent 'minor' mergers of moderate mass-ratios and not by major mergers alone. The results presented in this chapter have been published in Oser et al. (2012)

There is growing observational evidence for the existence of a population of massive galaxies ( $\approx 10^{11} M_{\odot}$ ) with small sizes ( $\approx 1$  kpc) and low star formation rates at redshift  $z \geq 2$ . These galaxies are smaller by a factor of three to five compared to present-day ellipticals at similar masses (e.g. Hyde & Bernardi 2009) and their effective stellar densities are at least one order of magnitude higher (Daddi et al. 2005; Trujillo et al. 2006; Longhetti et al. 2007; Toft et al. 2007; Trujillo et al. 2007; Zirm et al. 2007; Buitrago et al. 2008; van Dokkum et al. 2008; Cimatti et al. 2008; Franx et al. 2008; Saracco et al. 2009; Bezanson et al. 2009; Damjanov et al. 2009, 2011). Deep observations down to low surface brightness limits ( $H \approx 28$  mag arcsec $^{-2}$ ) show no evidence for faint, previously missed, stellar envelopes (Carrasco et al. 2010; Szomoru et al. 2010) and measurements of higher velocity dispersions seem to independently confirm previous high mass estimates (van der Wel et al. 2005, 2009; Cenarro & Trujillo 2009; van Dokkum et al. 2009; Cappellari et al. 2009; Martinez-Manso et al. 2011).

Quiescent (red & dead) galaxies make up about half of the general high redshift ( $z \approx 2$ ) population of massive galaxies and most of them (90%) are found to be compact (Kriek et al. 2006; van Dokkum et al. 2006, 2008; Williams et al. 2009). In the local Universe, galaxies of similar mass and size are extremely rare (Trujillo et al. 2009) or do not exist at all (Taylor et al. 2010). This indicates that present-day early-type galaxies were not fully assembled at  $z \approx 2$  and underwent significant structural evolution until the present day. Observations of the growth of massive galaxies since  $z \approx 2$  selected at constant number density (van Dokkum et al. 2010) indicate that they grow inside-out. A quiescent - without significant in-situ formation of new stars - build-up of extended stellar envelopes can originate from minor mergers and was predicted from cosmological simulations (Naab et al. 2007, 2009; Oser et al. 2010) and recently, for the first time such minor mergers at high redshift might have been directly observed (van Dokkum & Brammer 2010; Carrasco et al. 2010).

A simple picture of high redshift monolithic formation or, similarly, a binary merger of massive very gas-rich disks at  $z \gtrsim 2$  - which has been suggested as a reasonable formation mechanism for compact high-redshift galaxies (Wuyts et al. 2010; Ricciardelli et al. 2010; Bournaud et al. 2011) - followed by passive evolution can be ruled out (Kriek et al. 2008; van Dokkum et al. 2008; Trujillo et al. 2009) unless the increase in size of ellipticals can be explained by secular processes such as adiabatic expansion driven by stellar mass loss and/or strong feedback (Fan et al. 2008; Damjanov et al. 2009; Fan et al. 2010). This process seems to be disfavored by observations (e.g. Hopkins et al. 2010b; Trujillo et al. 2011) and the absence of a significant young stellar population would indicate that such hypothesized secular processes would need to occur without significant star formation.

Based on high-resolution cosmological simulations of individual galaxies, Naab et al. (2007, 2009) and Oser et al. (2010) provide an explanation for the size growth and the decrease in velocity dispersion, which is consistent with the cosmological hierarchical buildup of galaxies. The compact cores of massive galaxies form during an early rapid phase of dissipational in-situ star formation at  $6 \gtrsim z \gtrsim 2$  fed by cold flows (Kereš et al. 2005; Dekel et al. 2009a; Oser et al. 2010) and/or gas rich mergers leading to large

stellar surface densities (Weinzirl et al. 2011). At the end of this phase the observed as well as simulated galaxies are more flattened and disk-like than their low redshift counterparts (van Dokkum et al. 2008; Naab et al. 2009; van der Wel et al. 2011). They are already massive ( $\approx 10^{11} M_{\odot}$ ) but have small sizes of  $\approx 1$  kpc and velocity dispersions of  $\approx 240 \text{ km s}^{-1}$  (see also Joung et al. 2009), in general agreement with observations. The subsequent evolution is dominated by the addition of stars that have formed ex-situ, i.e. outside the galaxy itself (Oser et al. 2010). These accreted stars typically settle at larger radii (see also Coccato et al. 2011). The early domination of in-situ star formation and the subsequent growth by stellar mergers is in agreement with predictions from semi-analytical models (Kauffmann 1996; Khochfar & Silk 2006a; De Lucia et al. 2006; De Lucia & Blaizot 2007; Guo & White 2008; Shankar et al. 2010a,b) and the assembly scenario discussed in Kormendy et al. (2009).

In the absence of gas, stellar (i.e. collisionless) accretion and 'dry' merging in general is an energy conserving process in the sense that none of the gravitational and binding energy in the accreted systems can be radiated away during the merging event. Therefore, while the galaxies grow in mass, they must significantly increase their sizes and, eventually, decrease their velocity dispersions during this phase, in particular if the stars are accreted in minor mergers. In massive galaxies that are embedded in a hot gaseous halos some fraction of the gravitational energy can be radiated away (Johansson et al. 2009b). Cole et al. (2000), Naab et al. (2009) and Bezanson et al. (2009) presented the simple virial arguments for why minor mergers lead to a stronger size increase and a decrease in velocity dispersion than the more commonly studied major mergers (Naab et al. 2006).

In Oser et al. (2010) we investigated this two phase scenario in more detail with a larger sample of re-simulations and found a connection between galaxy mass, size, and the assembly history (see also Khochfar & Silk 2006a; De Lucia & Blaizot 2007; Guo & White 2008; Hopkins et al. 2009c; Feldmann et al. 2010). More massive present-day systems contain a larger fraction of accreted stars (up to 80 per cent) which, over time, build an outer envelope and increase the size of the systems (Naab et al. 2009; Hopkins et al. 2009b; Oser et al. 2010; Feldmann et al. 2010). This scenario receives support from recent observational findings that massive galaxies have increased their mass at radii  $r > 5$  kpc by a factor of  $\approx 4$  since  $z=2$  with the mass at smaller radii being essentially unchanged (van Dokkum et al. 2010). It is also the favored model to explain observed kinematics (Arnold et al. 2011) and metallicity gradients (Forbes et al. 2011) of globular cluster populations in nearby elliptical galaxies.

In this chapter we analyze a subset of massive galaxies from the simulations described in chapter 4 with a particular focus on the evolution of sizes and velocity dispersions since  $z \approx 2$ . This chapter is organized as follows: The results on the evolution of size and velocity dispersion are presented in sections 6.2 and 6.3. The stellar merger histories of the resimulated galaxies are reviewed in section 6.4. We conclude and discuss our results in section 6.5.

## 6.1 High resolution simulations of individual galaxy halos

The results presented in this chapter are drawn from the 'zoom-in' resimulations of the 40 most massive systems in our sample. The simulated halo masses cover the range  $7 \times 10^{11} M_{\odot} h^{-1} \lesssim M_{\text{vir}} \lesssim 2.7 \times 10^{13} M_{\odot} h^{-1}$  and the central galaxy masses are between  $4.5 \times 10^{10} M_{\odot} h^{-1} \lesssim M_{*} \lesssim 3.6 \times 10^{11} M_{\odot} h^{-1}$  at  $z = 0$ . The selected galaxies all have present-day masses larger than  $M_{*} \approx 6.3 \times 10^{10} M_{\odot}$  for direct comparison with observations. These galaxies are well resolved with  $\approx 1.5 \times 10^5 - 3 \times 10^6$  particles within the virial radius ( $R_{\text{vir}} \equiv R_{200}$ , the radius where the spherical overdensity drops below 200 times the critical density of the universe at a given redshift). Using the simulation parameters as described in section 4.6 for zoom simulations have been shown to result in galaxies with reasonable present-day properties (Naab et al. 2007; Johansson et al. 2009b; Naab et al. 2009; Oser et al. 2010). However, the fraction of available baryons converted into stars,  $f_{*}$ , for galaxies in this mass range is typically 2 times higher (see Fig. 4.4) than estimates from models that are constructed by matching observed luminosity functions to simulated halo mass functions (Guo et al. 2010b; Moster et al. 2010; Behroozi et al. 2010 and references therein).

## 6.2 Redshift evolution of sizes

In the left panel of Fig. 6.1 we show the projected half-mass radii of the simulated galaxies as a function of their stellar mass at  $z=0$  (blue circles), as well as the sizes and masses of their most massive progenitors at  $z=1$  (red triangles),  $z=2$  (green triangles), and  $z=4$  (purple stars). We determine the center of the galaxies using the shrinking sphere technique described in Power et al. (2003), starting at redshift 0 with a sphere that contains all the stellar particles. In all the previous snapshots the center of the most massive progenitor is found with the same technique starting with a sphere of a radius of at least 25 kpc that encompasses the 50 innermost particles identified in the last processed snapshot. The sizes indicated here are the mean values of the half-mass radii of all stars within  $0.1 \times R_{\text{vir}} \equiv R_{\text{Gal}}$  (considered the central galaxy) projected along the three principal axes of the main stellar body. We always show the median of the sizes of the galaxies that we compute from the snapshot at the target redshift as well as the two snapshots before and after this one to avoid outliers caused interacting systems. We separate the sample into quiescent galaxies (solid symbols) with specific star formation rates  $\text{sSFR} < 0.3/t_{\text{H}}$  (Franx et al. 2008), where  $t_{\text{H}}$  is the age of the Universe at each redshift. Star forming galaxies are indicated by open symbols and have  $\text{sSFR} > 0.3/t_{\text{H}}$ . The dashed black line shows the  $z=0$  linear fit to the SLACS sample of local early-type galaxies (Nipoti et al. 2009a) with the observed scatter given by the dotted lines, which is in good agreement with the simulated galaxy sizes. Other published local mass-size relations have slightly different slopes and offsets (see e.g. Hyde & Bernardi 2009; Guo et al. 2009; Williams et al. 2010) which does, however, not

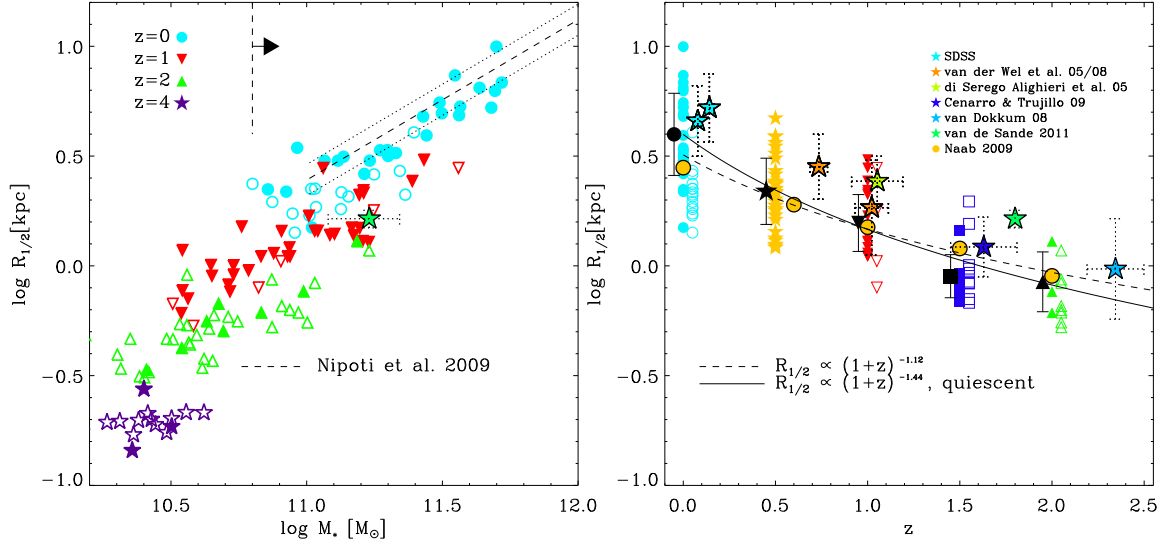


**Figure 6.1:** Left: Projected stellar half-mass radii of the simulated galaxies versus stellar masses for redshifts  $z=0$  (blue circles),  $z=1$  (red triangles),  $z=2$  (green triangles) and  $z=4$  (purple stars). Quiescent galaxies with low specific star formation rates ( $sSFR \leq 0.3/t_H$ ) have solid symbols, other galaxies have open symbols. Since  $z \approx 2$  all galaxies evolve rapidly in size. The dashed line indicates the observed size-mass relation for early-type galaxies of (Nipoti et al. 2009a) with the one-sigma scatter indicated by the dotted lines. The  $z=0$  mass cut of  $M_* > 6.3 \times 10^{10} M_\odot$  for the galaxy sample is indicated by the vertical dashed line. Right: Projected stellar half-mass radii of galaxies with stellar masses  $M_* > 6.3 \times 10^{10} M_\odot$  (see arrow on the left plot) as a function of redshift. The black symbols indicate the mean sizes at a given redshift with the error bars showing the standard deviation. The star forming galaxies (open symbols) and mean values are offset by 0.1 in redshift for clarity. The black lines show the result of a power law fit for all (dotted line) and quiescent (solid line) systems, respectively in good agreement with observed relations. Observational estimates from different authors are given by the solid star symbols where the dotted error bars show the observed scatter (see van Dokkum et al. 2008; Cenarro & Trujillo 2009) with the exception of the observation by van de Sande et al. (2011). Since this is a single object, here the error bars indicate the uncertainty of the measurement.. By  $z=3$  all progenitor galaxies drop below our mass limit.

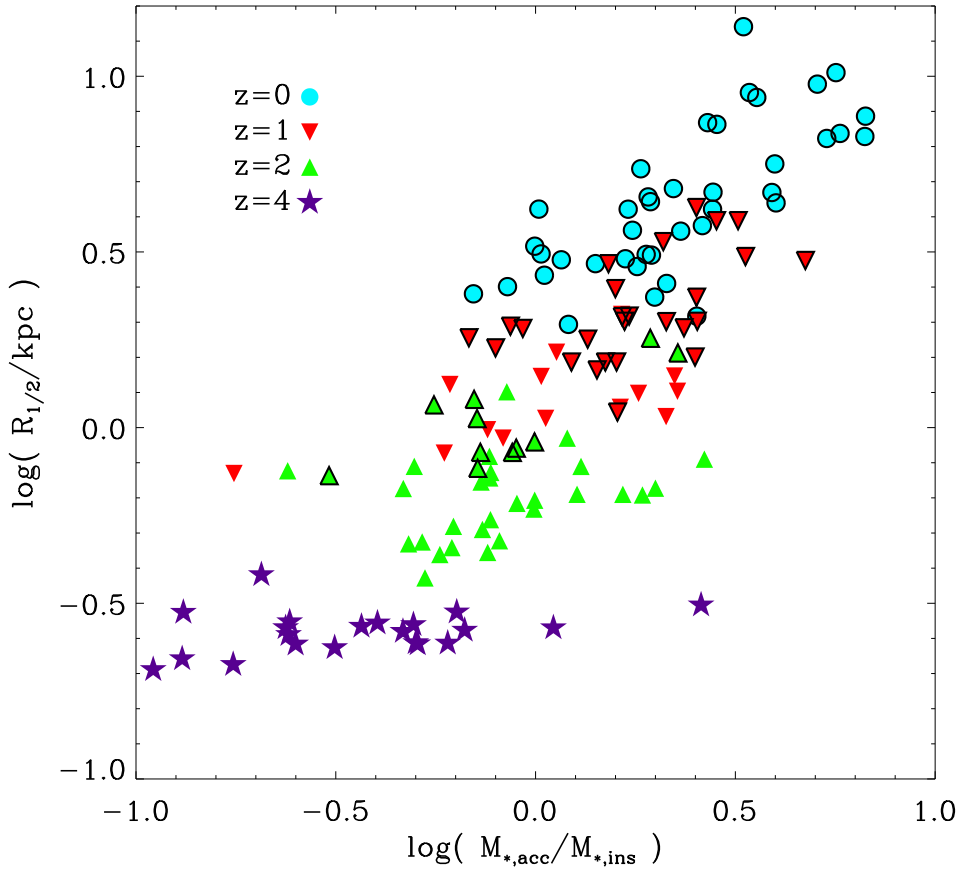


**Figure 6.2:** Projected stellar half-mass radius of the simulated galaxies at different redshifts (see Fig. 6.1) versus the fraction of stellar mass accreted (in major mergers, minor mergers and accretion events),  $M_{*,\text{acc}}$ , to the stellar mass formed in-situ,  $M_{*,\text{ins}}$ , in the galaxies. The black bordered symbols indicate systems more massive than  $M_* > 6.3 \times 10^{10} M_\odot$ . At  $z \gtrsim 2$  galaxies with a higher fraction of accreted stars have larger sizes indicating that accretion of stellar systems drives the size evolution of massive galaxies.

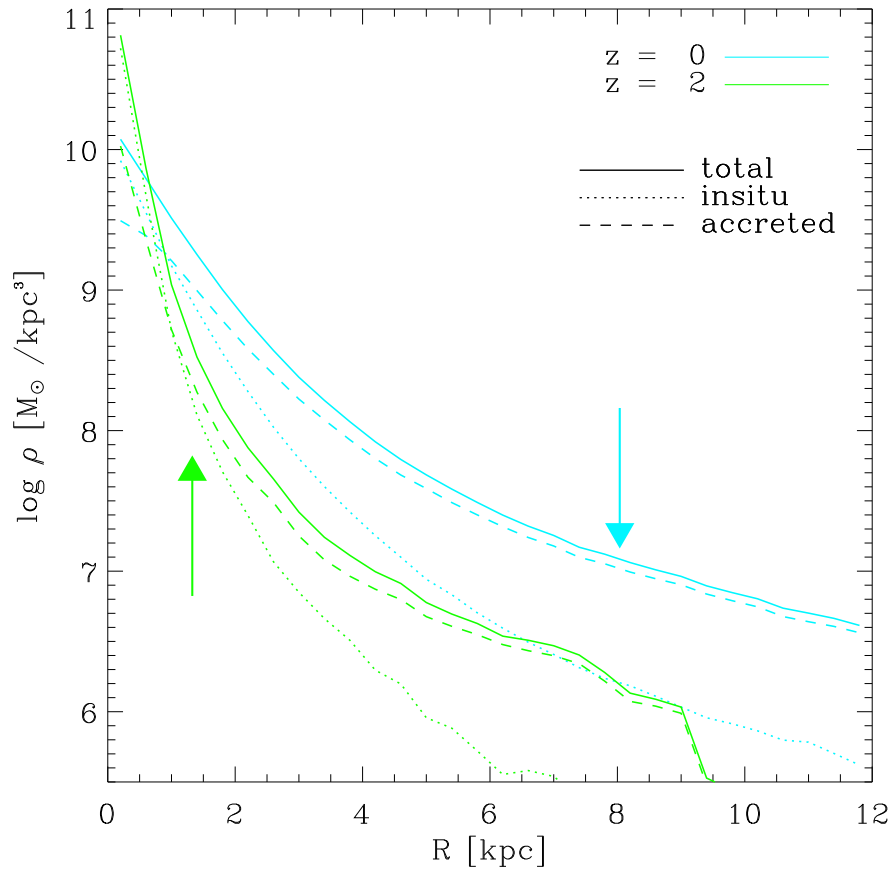


**Figure 6.3:** Stellar density as a function of radial distance to the galactic center at redshift 0 (blue) and 2 (green) averaged over the most massive systems ( $M_* > 2 \times 10^{11} M_{\odot}$  at  $z = 0$ ). The arrows indicate the average half-mass radii at a given redshift. At  $z = 2$  we find that the stellar mass profile inside the half-mass radius is still dominated by stars that have formed in-situ (dotted lines). At  $z = 0$  the half-mass radii of our galaxies have significantly extended due to accreted stars (dashed lines) which dominate the total density (solid lines) at larger radii.

affect our general conclusions. At  $z=4$  all progenitor galaxies are very compact with similar sizes ( $\approx 300$  pc) independent of their mass. During this phase the formation of the proto-galaxies is dominated by gas dissipation and in-situ star formation (Naab et al. 2009; Joung et al. 2009; Oser et al. 2010). By  $z=2$  a clearly visible mass-size relation has already developed. At this epoch the most massive galaxies of our sample have experienced the most rapid size growth with half-mass radii up to  $\approx 1.3$  kpc for galaxies with  $10^{11}M_{\odot}$  in stellar mass, in good agreement even with the most recent observations (e.g. Ryan et al. 2010; van der Wel et al. 2011; Cassata et al. 2011). Towards  $z=0$  the simulated galaxies continue to grow in size as well as mass. The descendants of galaxies that are already massive ( $> 6.3 \times 10^{10}M_{\odot}$ ) at  $z=2$  (green symbols to the right of the vertical dashed line) increase their mass by a factor of 3.5 ( $77 \pm 10\%$  of the accumulated mass is due to stellar accretion) and their projected half mass radii grow by a factor of 6.5. On average, all simulated galaxies more massive than  $6.3 \times 10^{10}M_{\odot}$  at any given redshift grow by a factor of 2.1 in mass (see e.g. Faber et al. (2007)) and a factor of 4.6 in radius since  $z=2$ . This already indicates that the size growth cannot be the result of equal-mass dry mergers, since the ensuing size growth should be, at most, directly proportional to the mass increase (Nipoti et al. 2003, 2009a; Naab et al. 2009). Overall, the size growth is differential, i.e. the most massive galaxies show the strongest size increase and the tilt of the mass-size relation increases towards lower redshifts. Fitting all galaxies with  $R_{1/2} \propto M_*^{\delta}$  we find  $\delta \approx 0.46 \pm 0.056$  at  $z=2$  and  $\delta \approx 0.69 \pm 0.064$  at  $z=0$ . For quiescent galaxies (with worse statistics) we find no trend for differential size growth with  $\delta \approx 0.67 \pm 0.069$  at  $z=2$  and  $\delta \approx 0.65 \pm 0.090$  at  $z=0$ . This is in qualitative agreement with recent observations by Williams et al. (2010) who do not find observational indications for a differential size growth of quiescent galaxies.

Observed sizes of massive galaxies are found to evolve as  $(1+z)^{\alpha}$ . Depending on the selection criteria (specific star formation rate, concentration etc.) and observed redshift range the observed values of  $\alpha$  for massive ellipticals range from  $\alpha = -0.75$  (Newman et al. 2010) to  $\alpha = -1.62$  (Damjanov et al. 2011). Franx et al. (2008) find  $\alpha \approx -0.8$  for all galaxies in this mass range ( $M_* \gtrsim 10^{11}M_{\odot}$ ) whereas for quiescent massive galaxies the observed size evolution is faster with  $-1.09 < \alpha < -1.22$ . Cassata et al. (2011) obtain values from  $\alpha = -0.87$  to  $\alpha = -1.42$  depending on stellar mass. van der Wel et al. (2008) find a value of  $\alpha \approx -0.98$ , when they include results from previous surveys this changes to  $\alpha \approx -1.20$ . A similar trend ( $\alpha \approx -1.11$ ) is found for UV-bright galaxies (Mosleh et al. 2011).

In the right panel of Fig. 6.1 we show the size evolution of galaxies more massive than  $6.3 \times 10^{10}M_{\odot}$  (see Franx et al. 2008) since  $z=2$ . At  $z=4$  all progenitor galaxies drop below the threshold mass, but are still resolved by  $\approx 10^4$  particles. We added the results from Naab et al. (2009), which were obtained with the same simulation code but with a softening length fixed in physical units. The size evolution in this case is very similar to the simulations that uses a fixed comoving softening length. We also included various observational results which find slightly larger sizes at a given redshift but with a very similar evolution in time. On average there is a strong evolution in galaxy sizes: for the  $R_{1/2} \propto (1+z)^{\alpha}$  power law fit to all (dashed line) and only

the quiescent (solid line) simulated galaxies we find a value of  $\alpha = -1.12 \pm 0.13$  and  $\alpha = -1.44 \pm 0.16$ , respectively. This is in good agreement with observed values - which are possibly a bit offset to higher values - and despite our statistical limitations we consider this trend robust. Possible simple explanations for an offset in size within a semi-analytical framework are discussed in Shankar et al. (2011).

To demonstrate the physical origin for the size growth in the simulated galaxies we show in Fig. 6.2 the projected half-mass radii presented in Fig. 6.1 at different redshifts as a function of the ratio of stars accreted onto the galaxy  $M_{*,\text{acc}}$  to the stars formed in-situ in the galaxy,  $M_{*,\text{ins}}$  at the same redshifts. We consider a star particle in the simulation as formed in-situ in the galaxy if it is created inside  $R_{\text{gal}} (\equiv 0.1 \times R_{\text{vir}})$ . Black bordered symbols indicate galaxies with stellar masses larger than  $6.3 \times 10^{10} M_{\odot}$  whose size evolution is plotted in the right panel of Fig. 6.1. There is a clear correlation between the relative amount of accreted stars and in-situ stars not only at redshift zero (Oser et al. 2010) but also at high redshifts ( $z \approx 2$ ). This indicates that stellar accretion drives the size evolution of the systems as soon as the accreted stars start to dominate the total mass ( $M_{*,\text{acc}}/M_{*,\text{ins}} > 1$ ) at  $z \approx 2$  as also predicted from semi-analytical modeling (Khochfar & Silk 2006b). At earlier times the stellar mass growth is dominated by in-situ star formation (Oser et al. 2010), i.e. the stars form out of cold gas that was able to radiate away a large fraction of its gravitational energy and thus leading to compact systems. The binding energy of the accreted stars, however, is retained and will increase the total energy content of the accreting galaxy, both by shock-heating the gas - which then can cool radiatively - as well as expanding the existing dark matter and stellar components (Johansson et al. 2009b). This in general leads to more extended systems.

In Fig. 6.3 we compare the density profiles of a subsample of massive galaxies ( $M_* > 2 \times 10^{11} M_{\odot}$ ) at redshift 2 and the present day. In agreement with Naab et al. (2009) we find that within the half-mass radius the high redshift systems are dominated by stars that formed in-situ while the contribution of accreted stars to the inner mass profile is small. At the present day the stellar mass inside the effective radius is dominated by accreted stars added at radii larger than  $> 1$  kpc. This accretion is responsible for the strong size increase (Oser et al. 2010) and is in agreement with the results from stacked imaging for massive galaxies at a constant number density that also show an increase in surface densities predominantly in the outer regions (van Dokkum et al. 2010).

### 6.3 Redshift evolution of velocity dispersions

In the left panel of Fig. 6.4 we show the central stellar line-of-sight velocity dispersions for the simulated galaxies as a function of the stellar mass at redshift  $z=4$  (purple stars),  $z=2$  (green triangles),  $z=1$  (red triangles) and  $z=0$  (blue circles). The line-of-sight velocity dispersions have been calculated within  $0.5 \times R_{1/2}$  along the three principal axes and then averaged. The mass-dispersion relation from Nipoti et al. (2009a) for galaxies

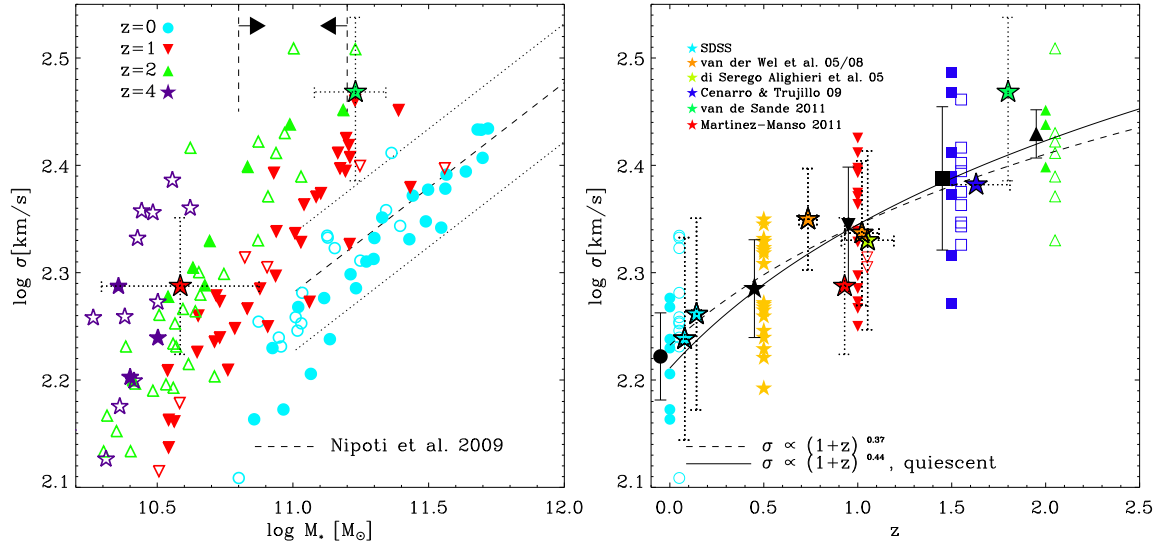


**Figure 6.4:** Central (within  $0.5 R_{1/2}$ ) projected velocity dispersion as a function of stellar mass at  $z=0$  (blue circles),  $z=1$  (red triangles),  $z=2$  (green triangles) and  $z=4$  (purple stars). The relation for local galaxies from Nipoti et al. (2009a) are shown by the dashed line with the dotted lines indicating the scatter of the observed galaxies. At a given mass the velocity dispersion decreases significantly from  $z=4$  to  $z=0$ . The mass limits used for the right plot are indicated by the vertical dashed lines. Right: Central projected velocity dispersion of the simulated galaxies with masses in the range of  $6.3 \times 10^{10} M_\odot < M_* < 1.6 \times 10^{11} M_\odot$  at any given redshift as a function of redshift. Solid symbols represent star forming galaxies and empty symbols show quiescent systems (offset by 0.1 in redshift for clarity). Observational estimates from different authors are given by the solid star symbols (see Cenarro & Trujillo 2009; van de Sande et al. 2011; Martinez-Manso et al. 2011) with the observed scatter given by the dotted error bars, where available. The black lines show the result of a power law fit for all (dashed line) and the quiescent (solid line) galaxies, respectively. The simulations indicate a mild dispersion evolution from  $\approx 262 \text{ km s}^{-1}$  at  $z=2$  to  $\approx 177 \text{ km s}^{-1}$  at  $z=0$ , in agreement with observations.

more massive than  $M_* \approx 10^{11} M_\odot$  is indicated by the dashed line. It is evident that at a given mass range the velocity dispersions of the galaxies systematically increase with redshift. This is illustrated in the right panel of Fig. 6.4 where we show the evolution of the projected velocity dispersion for galaxies with masses in the range of  $6.3 \times 10^{11} M_\odot < M_* < 1.6 \times 10^{12} M_\odot$  (indicated by the vertical lines in the left panel) as a function of redshift. In this mass range the velocity dispersions drop from  $262 \pm 28 \text{ km s}^{-1}$  at  $z=2$  to  $177 \pm 22 \text{ km s}^{-1}$  at  $z=0$ , a decrease of roughly a factor of 1.5. The evolution is statistically significant but weak (see also Hopkins et al. 2009c). The black lines show a fit for the average velocity dispersions for all (dashed line) and the quiescent (solid line) galaxies only. As for the sizes, we fit the redshift evolution of the velocity dispersions like  $\sigma_{1/2} \propto (1+z)^\beta$ . Again we find a slightly stronger evolution for the quiescent systems ( $\beta = 0.44$ ) than for all galaxies in our samples ( $\beta = 0.37$ ). van de Sande et al. (2011) obtain a similar value of  $\beta = 0.51 \pm 0.07$ . Depending on selection criteria Saglia et al. (2010) find values for  $\beta$  ranging from  $0.59 \pm 0.10$  to  $0.19 \pm 0.10$ . Following Cenarro & Trujillo (2009) we compare to observations of local ellipticals and measurements at higher redshift (di Serego Alighieri et al. 2005; van der Wel et al. 2005, 2008; Cenarro & Trujillo 2009). In general we find a good agreement with the observations.

## 6.4 Stellar Merger histories

Similar to Cole et al. (2000), Naab et al. (2009) and Bezanson et al. (2009) demonstrated, using the virial theorem, how the size growth of a galaxy after a dissipationless merger event can be predicted. Assuming energy conservation and parabolic orbits (Benson 2005; Khochfar & Burkert 2006) the final gravitational radius of the system is given by

$$\frac{R_{g,f}}{R_{g,i}} = \frac{(1 + \eta)^2}{(1 + \eta\epsilon)}, \quad (6.1)$$

where  $R_{g,i}$  and  $R_{g,f}$  are the initial and final gravitational radii (before and after the merger event) which we assume to be proportional to the spherical half mass radii (Naab et al. 2009). Here,  $\eta = M_a/M_i$  is the fractional mass increase during the merger and  $\epsilon = \langle v_a^2 \rangle / \langle v_i^2 \rangle$  is the ratio of the mean square speeds of the accreted satellites and the initial system. This estimate implies that the accretion of weakly bound stellar systems ( $\epsilon \ll 1$ ) results in a particularly efficient size increase. To test the validity of this simple estimate in our full cosmological simulation we follow the stellar merger histories of our simulated galaxies. We identify every satellite merging with the most massive progenitor of the central galaxy using a FOF-finder with a minimum number of 20 stellar particles ( $\approx 1.2 \times 10^8 M_\odot$ ). At  $z = 2$  all galaxies in our sample are more massive than  $\approx 10^{10.1} M_\odot$ , i.e. we resolve mergers at least down to a mass-ratio of  $\approx 1 : 100$ . For the satellites as well as the host we compute the mass and the total internal velocity dispersion and with this information and Eqn. 6.1 we estimate the size evolution since  $z=2$ . In Fig. 6.5 we show the estimated size growth for all galaxies

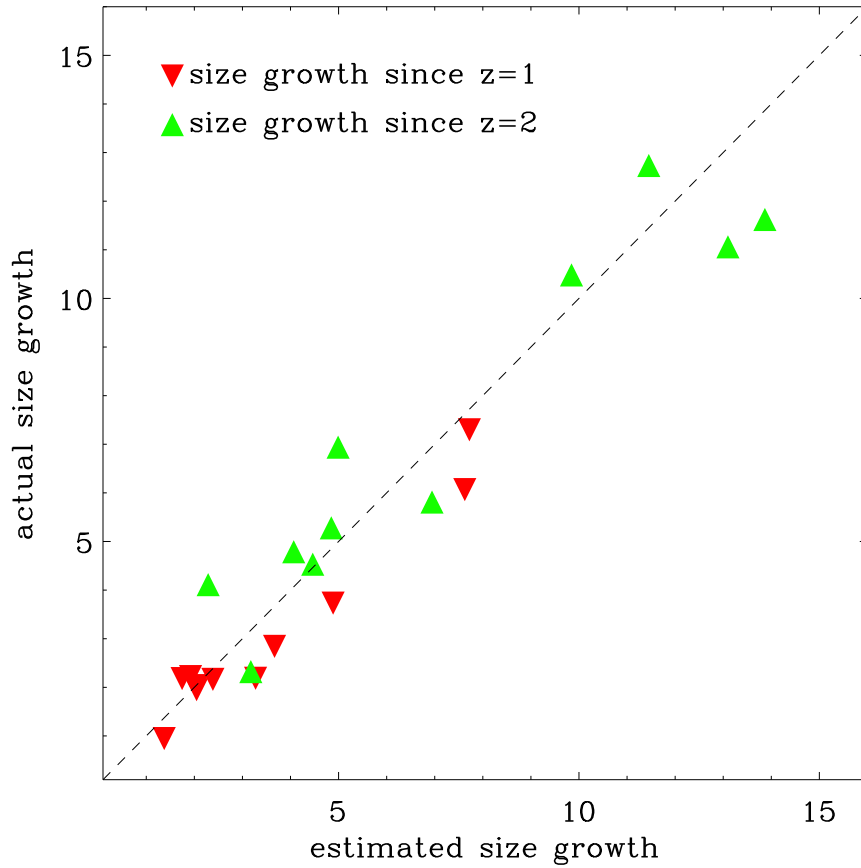


**Figure 6.5:** The size growth predicted by equation 6.1 in combination with the stellar merger histories compared to the actual size growth in the simulations of the galaxies more massive than  $M_* = 6.3 \times 10^{10} M_\odot$  at  $z=2$ . The green triangles indicate the evolution between  $z=2$  and  $z=0$  the red triangles the evolution between  $z=1$  and  $z=0$ . The simple virial estimate is a good predictor for the actual size evolution.

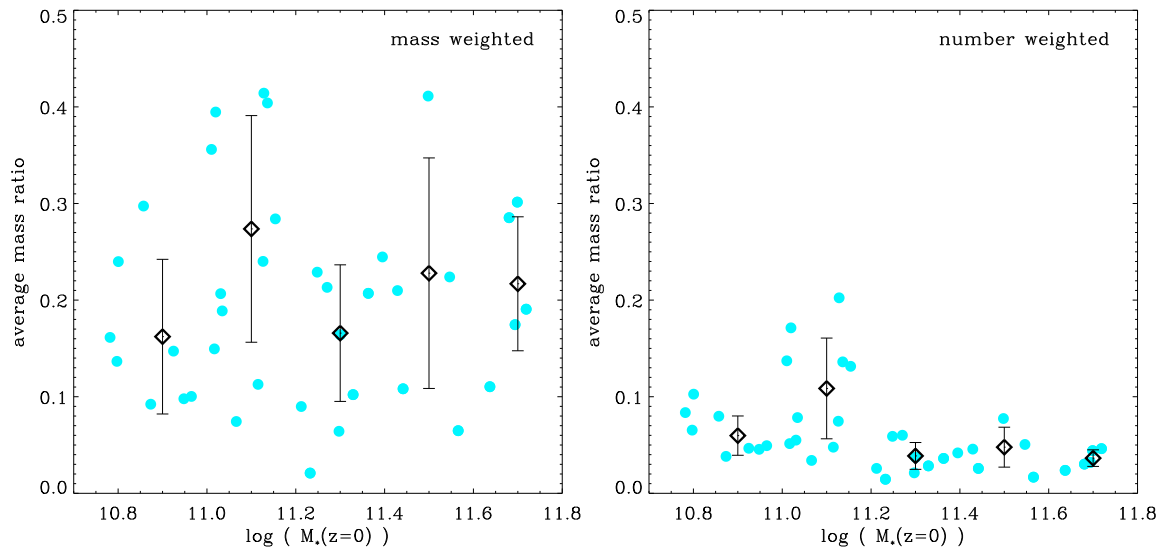


**Figure 6.6:** Left: The average mass-weighted stellar merger mass-ratios (since  $z=2$ ) as a function of present-day galaxy mass (blue dots). The black diamonds show the binned averages within 0.2 dex in stellar mass with the one sigma error bars. Trends with galaxy mass are statistically not significant. The mass growth is dominated by minor mergers with a mass ratio of  $\approx 1:5$ . Right: The average number-weighted merger mass-ratio (for all stellar mergers since  $z=2$ ) as a function of present-day galaxy mass. There is a weak trend for more massive galaxies to experience relatively more minor mergers. On average most stellar mergers have mass-ratio of  $\approx 1:16$ .

exceeding the  $z=2$  mass limit of  $6.3 \times 10^{10} M_{\odot}$  since redshift 2 (green triangles) and 1 (red triangles), respectively. We compare this estimated size growth to the actual size growth that we directly measure from our simulated galaxies. Considering the simplifications used in Eqn. 6.1 - homologous, one-component systems merging on zero energy orbits - the predicted and actual growth agree notably well. This confirms earlier findings (Naab & Ostriker 2009) that the simple formula is a good predictor even in a full cosmological context. This approximation however can only be valid if the assembly history for  $z < 2$  is not dominated by dissipational processes which is the case for the massive systems presented here (see Oser et al. 2010 for the relevant analysis).

To better understand the dominant assembly mechanism of our simulated massive galaxies we have computed the average mass-weighted merger mass-ratio for every galaxy since  $z=2$ . In the left panel of Fig. 6.6 we show the average mass-weighted merger mass-ratio as function of present-day stellar galaxy mass (blue dots). The dependence on galaxy mass is weak. The average values in bins of 0.2 dex in mass are shown by the black diamonds with one sigma errors bars. Overall the average mass-weighted merger mass-ratio is  $\sim 0.20 \pm 0.10$ . This makes 'minor mergers' with mass ratios of 1:5 the dominant assembly mode, on average, for the massive simulated galaxies (see Hirschmann et al. 2011 for a representation of a typical merger tree). The tendency of this ratio to change with the mass of the host system cannot be determined by our calculations with any statistical certainty (the slope of the fitted curve is  $0.05 \pm 0.18$ ). However, we anticipate that for very low mass galaxies major mergers would become more important. If the slope of the mass function for satellites were  $d(\ln N)/d(\ln M) \sim -\gamma$ , then the expectation would be that the mass-weighted merger ratio would be  $(2 - \gamma)/(3 - \gamma) \sim 0.44$  if dynamical friction were not a dominant process and  $(3 - \gamma)/(4 - \gamma) \sim 0.64$  if it were dominant. Thus, for low mass parent galaxies, we would anticipate that the typical merger would be relatively 'major' with the ratio of parent to satellite being  $\sim 1 : 2$ . Here we note that a significant number of the simulated galaxies (7 out of 40,  $\approx 18$  per cent) do not experience any merger with a mass ratio larger than 1:4, e.g. they have experienced no major merger since  $z=2$  at all. Estimates of merger rates for massive galaxies due to observations of disturbed systems (Jogee et al. 2009; Kaviraj et al. 2011; Lotz et al. 2011), as well as semi-analytic models lead to similar results. E.g. Khochfar & Silk (2009), Hopkins et al. (2010a) and Shankar et al. (2010a) find, that massive early-type galaxies on average encounter less than one major dry merger since their formation epoch. This confirms previous suggestions motivated by the dearth of compact galaxies in the nearby Universe, that a highly stochastic process like major mergers cannot be the main driver for the observed size evolution (Bezanson et al. 2009; Trujillo et al. 2009; Taylor et al. 2010). However, major mergers do happen and will have an impact on the early-type galaxy population. They can contribute significantly to the final stellar mass with minor mergers still dominating the size growth (Shankar et al. 2010b, 2011). The observed merger rates, which are difficult to determine, are in the range of only  $\sim 1$  major merger since  $z = 2$  (Bell et al. 2006; Bluck et al. 2009; Naab et al. 2006) which is consistent

with our interpretation.

In the right panel of Fig. 6.6 we show, the more conventionally defined, average number-weighted merger mass-ratio. The merger history since  $z=2$  is clearly dominated by minor mergers with mass-ratios smaller than 1:10. Those mergers, however, do on average not add most of the mass to the systems. There is a slight trend for more massive galaxies to experience a larger relative number of minor mergers. Over the full mass range the average number-weighted merger mass ratio is  $\sim 0.062 \pm 0.043$ , indicating that the typical merger was indeed very minor (1:16).

## 6.5 Conclusion & Discussion

In this chapter we use a sample of 40 cosmological re-simulations of individual massive galaxies to investigate the evolution of galaxy sizes and velocity dispersions with redshift. The simulated galaxies form in a two phase process (Oser et al. 2010) where the first phase at redshifts of  $z \gtrsim 2$  is dominated by a dissipative assembly. This formation phase is driven by in situ star formation resulting in compact galaxies having small sizes of  $r \lesssim 1.3$  kpc. The subsequent evolution of the galaxies at redshifts of  $z \lesssim 2$  is dominated by accretion of stars in satellite stellar systems. Naab & Ostriker (2009) and Oser et al. (2010) have shown that the accreted stellar systems preferentially settle into the outer parts of the galaxies, resulting in a gradual increase in their sizes until the simulated galaxies closely follow the present-day mass-size relation. Between redshift 2 and 0 our simulated galaxies grow on average by a factor of  $\sim 5 - 6$ , whereas recent semi-analytical models find a smaller size increase of  $\sim 2 - 4$  (Khochfar & Silk 2006a; Guo et al. 2011; Covington et al. 2011). At the present day 25 out of the 40 simulated galaxies are quiescent ( $s\text{SFR} \leq 0.3/t_H$ ) and have structural parameters in agreement with observed local early-type galaxies. The underlying physical reason for the size growth for our simulated galaxies is stellar accretion, as can be seen in the strong positive correlation between the projected stellar half-mass radii and the fraction of accreted stellar material (Fig 6.2). Our detailed analysis presented in this chapter confirms that the stellar material is predominantly accreted through minor mergers (Naab et al. 2009), with typical galaxy mass-ratios of  $\approx 1 : 5$ . By number the merger history is dominated by even more minor mergers with mass-ratios of  $\approx 1 : 16$ . A significant fraction (18 per cent) of the galaxies experience no major merger with mass-ratios larger than 1:4 since  $z=2$  confirming previous suggestions, motivated by the lack of compact galaxies in the nearby Universe, that a highly stochastic process such as major mergers cannot be the main driver for the observed size evolution (Bezanson et al. 2009; Trujillo et al. 2009; Taylor et al. 2010). Semi-analytical models also find significant stellar mass growth due to minor mergers. These models, however, predict that for the most massive galaxies major mergers are becoming increasingly important (e.g. Baugh et al. 1996; De Lucia et al. 2006; De Lucia & Blaizot 2007; Guo & White 2008). This is a result of the sharp drop-off in the galaxy mass function due to AGN feedback, which is not followed in our simulations.

For galaxies with masses above  $6.3 \times 10^{10} M_{\odot}$  our simulated size evolution is in very good agreement (Fig 6.1) with the observed size evolution of galaxies with similar masses at redshifts of  $z \lesssim 2$  (e.g. Franx et al. 2008). The evolution of the sizes can be well described by  $R_{1/2} \propto (1+z)^{\alpha}$  with  $\alpha = -1.12$  for all galaxies and  $\alpha = -1.44$  for quiescent galaxies only. The size growth measured from the simulations is in good agreement with simple estimates from the virial theorem assuming energy conservation during dissipationless merger events (Naab et al. 2009).

The projected velocity dispersions for simulated galaxies with masses around  $\approx 10^{11} M_{\odot}$  decrease systematically towards lower redshifts from  $\approx 262 \text{ kms}^{-1}$  at  $z=2$  to  $177 \text{ kms}^{-1}$  at  $z = 0$ , again in good agreement with observations (e.g. Cenarro & Trujillo 2009). Assuming an evolution as  $\sigma_{1/2} \propto (1+z)^{\beta}$  we find  $\beta = 0.37$  for all galaxies and  $\beta = 0.44$  for quiescent galaxies. Future observations might confirm this prediction.

We conclude that in the absence of dissipation and associated star formation a growth scenario dominated by minor stellar mergers, with less bound stars, is a viable physical process for explaining both the observed growth in size and the decrease in velocity dispersion of massive early-type galaxies from  $z \sim 2$  to the present-day. Accretion of systems not gravitationally bound to the central galaxy causes, as noted, substantial size growth. But it has another, dramatic, concomitant effect. As this mass becomes gravitationally bound, it releases a large amount of gravitational energy. This process, which has been measured in our simulations (Khochfar & Ostriker 2008; Johansson et al. 2009b), and termed 'gravitational heating' can add  $\sim 10^{59.5}$  ergs (i.e.  $\sim 10^{43}$  erg/s) to the parent systems, causing heating of the ambient gas and reducing the central dark matter component.

Despite these successes some obvious caveats concerning our simulations remain. Most importantly our simulated galaxies are overly efficient in transforming gas into stars (Hirschmann et al. 2011) and consequently the conversion efficiency of baryons into stars, even at  $z=2$ , in the massive galaxies in our simulated sample is overestimated by roughly a factor of  $\approx 2$  compared to predictions from halo occupation models (Behroozi et al. 2010 and references therein). This discrepancy is most probably due to the fact that our simulations neither include strong supernova-driven winds nor AGN feedback from supermassive black holes and would be enhanced if metal-line cooling was included. Observations and modeling have shown that strong galactic winds generating significant outflows are ubiquitous at high redshifts of  $z \sim 2 - 3$  (e.g. Steidel et al. 2010; Genel et al. 2010) and in our simulations this aspect is missing by construction. The effect of supernova driven winds and AGN feedback is differential with respect to the masses of galaxies, with the former primarily affecting smaller galaxies (Oppenheimer et al. 2010b) and the latter being increasingly important for more massive galaxies (Kormendy et al. 2009). The proper inclusion of all the above mentioned physical effects would certainly lower the overall total stellar masses (both the in-situ and the accreted component). Still, the relatively simple two-phase formation scenario provides a viable model to physically explain the observed growth in size and decrease in velocity dispersion. However, this is an issue clearly deserving further studies on the effect of AGN feedback (e.g. Sazonov et al. 2004; Di Matteo et al. 2005; Springel et al.

---

2005a; Johansson et al. 2009a; Booth & Schaye 2009; Debuhr et al. 2010; Ostriker et al. 2010; Schaye et al. 2010), radiative feedback from stars (e.g Oppenheimer & Davé 2006; Petkova & Springel 2009; Hopkins et al. 2011) and feedback from supernovae type II (e.g Scannapieco et al. 2008; Schaye et al. 2010; Sales et al. 2010) and Ia (e.g Ciotti & Ostriker 2007; Oppenheimer & Davé 2008). Preferentially this will be investigated with the help of a large sample of zoom simulations with better statistics, as presented here, with the aim of studying how these processes would affect in detail the resulting size growth and velocity dispersion evolution of massive galaxies.



## Stellar Kinematics

We perform the first detailed two-dimensional stellar dynamical analysis of cosmological hydrodynamical simulations of individual galaxies. Kinematic maps of the stellar velocity, velocity dispersion, and higher-order Gauss-Hermite moments  $h_3$  and  $h_4$  are presented in this chapter. The velocity and velocity dispersion fields of the simulated galaxies show a similar diversity to observed kinematic maps of early-type galaxies in the ATLAS<sup>3D</sup> survey. This includes fast, slow, and misaligned rotation, hot spheroids with embedded cold disk components as well as galaxies with counter-rotating disk-like components. We quantify the amount of rotation using the  $\lambda_R$ -parameter. In general, the most massive and round simulated galaxies are slow rotators, as observed. These galaxies grow to a significant degree by collisionless late accretion of stars, predominantly in more minor mergers with average mass-weighted mass-ratios of 1:5. The role of major mergers for the formation of slow rotators in a cosmological context is ambiguous. We find fast as well as slow rotating remnants with late major mergers. The galaxy most consistent with the rare class of non-rotating ellipticals grows by minor mergers alone. This might indicate the importance of accretion of weakly bound stellar systems during their formation. The mass assembly of fast rotators is dominated by dissipative in-situ star formation. In agreement with previous theoretical studies and observations the fast rotating components of these galaxies also have asymmetric line-of-sight velocity distributions with steep leading wings, i.e. a velocity- $h_3$  anti-correlation. The results presented in this chapter will be published as part of the ATLAS<sup>3D</sup> project.

Observationally, the *ATLAS*<sup>3D</sup> survey (Cappellari et al. 2011a) provides the most complete panoramic view on the properties of 260 local early-type galaxies (ETGs) in a volume limited sample covering different environments (Cappellari et al. 2011b). This includes a complete inventory of the central and extended baryonic galactic building blocks such as stars (Emsellem et al. 2011; Duc et al. 2011), molecular gas (Young et al. 2011; Davis et al. 2011), neutral gas (Serra et al. 2011, in preparation) and ionized gas (Davis et al. 2011, in preparation), as well as high-density gas tracers (Crocker et al. 2011, in preparation). This is combined with unique two-dimensional information about the stellar (Krajnović et al. 2011; Emsellem et al. 2011) and gaseous (Davis et al. 2011) kinematics as well as photometry (Krajnović et al. 2011) within the main body of the galaxies.

The theoretical effort within the survey is twofold. Based on the observed photometry and kinematics we aim at understanding the underlying three-dimensional dynamical structure (Emsellem et al. 2011; Krajnović et al. 2011, Cappellari et al. 2011, in preparation) and the chemical composition, the ages of the stellar populations (McDermid et al. 2011, in preparation), as well as a combination of both (Scott et al. 2011, in preparation; Kuntschner et al. 2011, in preparation). With a - backwards - archaeological approach we can then put constraints on the formation histories of ETGs. Based on semi-analytical models (Khochfar et al. 2011) and simulations we investigate possible - forward - formation scenarios and check their success in predicting the observed present day galaxy properties. The simulations cover different levels of complexity: idealized high-resolution simulations of mergers between two or more galaxies including (or not) star formation (Bois et al. 2010, 2011), simulations of model realizations of observed galaxies (Bournaud et al. 2011, in preparation), and simulations of the entire formation history of galaxies in a full cosmological context as presented in this work. One of the striking results from *ATLAS*<sup>3D</sup>, which is in the focus of this chapter, is that the majority (86%, 224/260) of ETGs shows significant (disk-like) rotation with regular velocity fields. Only a small fraction (12%, 32/260) of the galaxies rotate slowly with no indication of embedded disc components (Krajnović et al. 2011; Emsellem et al. 2011). Galaxies with corresponding properties were coined fast rotators and slow rotators, respectively, by the preceding SAURON survey (Bacon et al. 2001; de Zeeuw et al. 2002; Emsellem et al. 2004) based the  $\lambda_R$ -parameter ( $\lambda_R > 0.1$  = fast rotator,  $\lambda_R < 0.1$  = slow rotator), which gives an approximate measure of the angular momentum of a galaxies from its two-dimensional line-of-sight velocity field (Emsellem et al. 2007). Fast rotators dominate the low- and intermediate-mass field population (Cappellari et al. 2011b) and form a quite homogeneous family of flattened, oblate systems with regular velocity fields. Typical slow rotators dominate in high density environments, are among the most massive round galaxies, and have peculiar properties like kinematic twists and kinematically decoupled components (Krajnović et al. 2011; Emsellem et al. 2011).

Given the above kinematical characteristics theorists (and observers) might wonder (or not) in how far the properties of fast and slow rotators are consistent with popular formation scenarios for ETGs. Interestingly, one of the first formation scenarios for

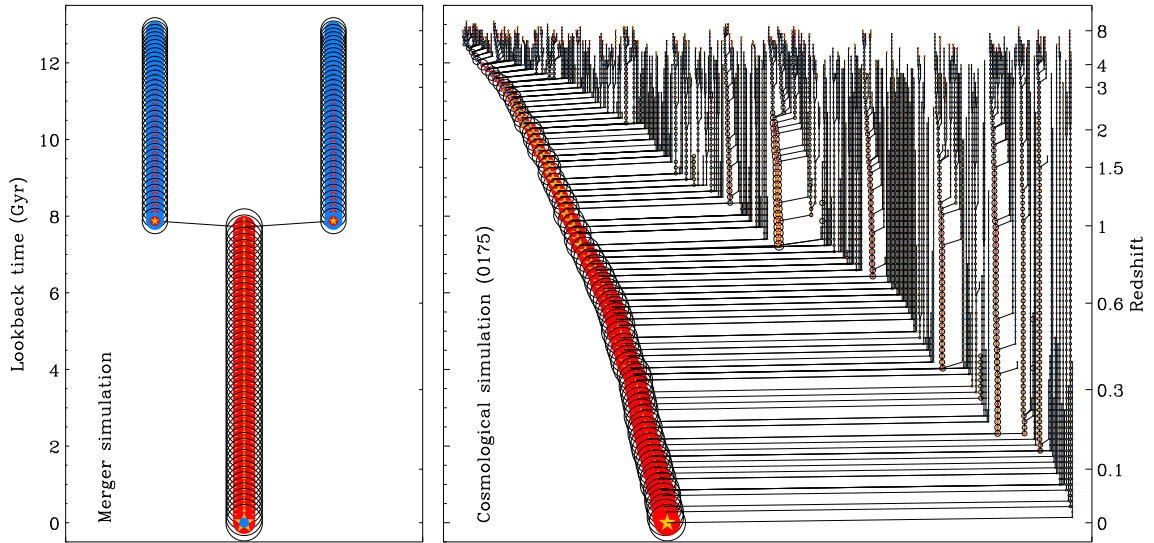


**Figure 7.1:** *Left panel:* Schematic 'merger-tree' representation of a binary disk merger simulation. Two gas-rich (blue) stellar (yellow) disks with little hot gas (red) merge at  $z \approx 1$  and form an elliptical galaxy. *Right panel:* Computed merger tree for the formation of halo (0175) and its galaxy within the concordance cosmology. Black circles indicate the dark matter halo mass at every redshift with the symbol size proportional to the square root of the normalized halo mass at  $z = 0$ . The yellow stars indicate stellar mass, the blue and red filled circles show the cold and hot gas mass within the virial radius (Hirschmann et al. 2011). It is evident that almost continuous infall of matter in small and large units is an important characteristic of the assembly of massive galaxies (see e.g. (De Lucia & Blaizot 2007)). The galaxy shown (0175) has no major merger since  $z \approx 3$ . Others galaxies can have 1-3 major mergers. The growth, however, is always accompanied by minor mergers (see Section 7.3)

ETGs, before the advent of modern hierarchical cosmologies, was motivated by, back then, new measurements of the kinematics of stars in the outer halo of the Milky Way. The radial orbits of old, non-rotating, halo stars were explained by their rapid formation in collapsing protogalactic cold gas streams, followed by the formation of stars on circular orbits in a thin cold gas disk (Eggen et al. 1962). If this simple formation scenario were true for all old spheroidal systems they would consist of a spherical bulge with stars on radial orbits and a thin rotating disk component whose relative mass would depend on the efficiency of star formation (i.e. gas consumption) during the collapse and on the ability of the gas to cool. The amount of "turbulent viscosity", caused by large inhomogeneities in the in falling gas clouds, and the angular momentum of the in falling gas determine the predicted galaxy properties such as isophotal shapes, rotation, age and metallicity gradients, and even the formation of disk-like substructures in elliptical galaxies which have successfully been computed decades ago (Partridge & Peebles 1967; Larson 1969, 1974; Searle et al. 1973; Larson 1975). In simple words, the pre-merger-scenario and pre- $\Lambda$ CDM model for the formation of fast and slow rotators was as follows: the bulk of the stars in slow rotators form in rapidly collapsing gaseous systems with efficient star formation and efficient gas heating, fast rotators in settled systems with inefficient star formation in the absence of strong heating processes.

An alternative (or supplementary) scenario was provided by Toomre & Toomre (1972) and Toomre (1974, 1977) who investigated tidal interactions between disk galaxies and the possible formation of spheroidal systems by merging spirals. This scenario became particularly attractive as mergers play an important role during the formation and/or evolution of every dark matter halo and almost every galaxy in modern hierarchical cosmological models (White & Rees 1978). This scenario quickly started a whole industry of simulations of mergers of disk with disks and spheroids with other spheroids. Early simulations of spheroid mergers focused on the evolution of already existing spheroids and were mainly used to investigate the evolution of abundance gradients and the merger dynamics (White 1978, 1979b). Back then it was already shown that major mergers can significantly flatten preexisting abundance gradients (White 1978) and the difficulty of forming slowly rotating ellipticals from mergers of ellipticals was pointed out (White 1979a, 1980), a problem that has been confirmed with modern high-resolution simulations (Bois et al. 2010). Later studies of spheroid mergers mainly focused on the merger dynamics, the evolution of scaling relations, also investigating the effect of different mass-ratios (Makino & Hut 1997; Nipoti et al. 2003; Boylan-Kolchin et al. 2005; Naab et al. 2006; Boylan-Kolchin et al. 2006; Nipoti et al. 2009b,a; Di Matteo et al. 2009).

A separate process that was investigated using idealized merger simulations was the formation of elliptical galaxies by the morphological transformation of disk galaxies in a major galaxy merger. The first self-consistent disk merger simulations clearly demonstrated that a major merger can indeed transform a kinematically cold disk into a kinematically hot spheroid with elliptical-like properties (Gerhard 1981; Farouki & Shapiro 1982; Negroponte & White 1983). Simulations of isolated merger events, however, are rather limited in reproducing the formation history of a galaxy in a

$\Lambda$ CDM Universe. Fig. 7.1 is comparing the schematic 'merger-tree' of a binary merger simulation to one that is typical for the cosmological simulations presented in this work. We have already shown in section 6.4 the accretion history of galaxies is often dominated by minor mergers, that are usually ignored in idealized merger simulations.

## 7.1 High-resolution simulations of individual galaxy halos

The analysis presented in this chapter is based on 50 'zoom-in' cosmological hydrodynamic simulations of individual massive galaxy halos selected from a larger set of re-simulations (Oser et al. 2010; Hirschmann et al. 2011), described in section 4.6.2. We present results from re-simulated halos in the mass range of  $1.3 \times 10^{12} M_{\odot} h^{-1} \lesssim M_{\text{vir}} \lesssim 2.7 \times 10^{13} M_{\odot} h^{-1}$  presented in Oser et al. (2012). The halos host massive galaxies with present day stellar masses between  $6.3 \times 10^{10} M_{\odot} h^{-1} \lesssim M_{*} \lesssim 3.6 \times 10^{11} M_{\odot} h^{-1}$  and projected half-mass radii of  $1.5 < r_{1/2} < 10.5 \text{ kpc}$ . All galaxies are well resolved with  $\approx 1.5 \times 10^5 - 3 \times 10^6$  particles within the virial radius. The masses of individual gas and star particles are  $m_{*,\text{gas}} = 4.2 \times 10^6 M_{\odot} h^{-1}$  (we spawn one star particle per gas particle), and the dark matter particles have a mass of  $m_{\text{dm}} = 2.5 \times 10^7 M_{\odot} h^{-1}$ . Compared to some other recently presented cosmological zoom simulations (Scannapieco et al. 2009; Governato et al. 2009; Dolag et al. 2009; Feldmann et al. 2010; Piontek & Steinmetz 2011; Feldmann et al. 2011; Scannapieco et al. 2011; Governato et al. 2010; Puchwein et al. 2010; Guedes et al. 2011; Agertz et al. 2011; Teyssier et al. 2011; Avila-Reese et al. 2011) the resolution level of our simulations is comparable or slightly lower. But while these simulations were limited to a single or few halos in a narrow mass range we performed a significantly larger number of re-simulations of halos spanning a mass range of two orders of magnitude.

Cosmological zoom simulations using similar simulation parameters to the sample presented here - also not including the effect of AGN feedback - typically resulted in galaxies with photometric and kinematic properties similar to present day ETGs (Naab et al. 2007; Johansson et al. 2009b; Naab et al. 2009; Feldmann et al. 2010). In particular, the galaxies presented in this work agree with present day ETG scaling relations and their observed evolution with redshift (Oser et al. 2012). Still, the employed star formation prescription favors efficient star formation at early times resulting in preferentially spheroidal systems with old stellar populations and we do not produce supernova driven winds. In addition, models for feedback from central AGN are not included. Therefore, the fraction of available baryons (in every halo) converted into stars of the central galaxies in the simulated mass range is typically 2 times higher than estimates from models matching observed galaxy mass functions to simulated halo mass functions (Oser et al. 2010; Guo et al. 2010b; Moster et al. 2010; Behroozi et al. 2010; Neistein et al. 2011; Leauthaud et al. 2011). The physical processes eventually responsible for this discrepancy are well studied. It has been argued that feedback from SNII is important for low mass systems (Larson 1974; Dekel & Silk 1986; Governato

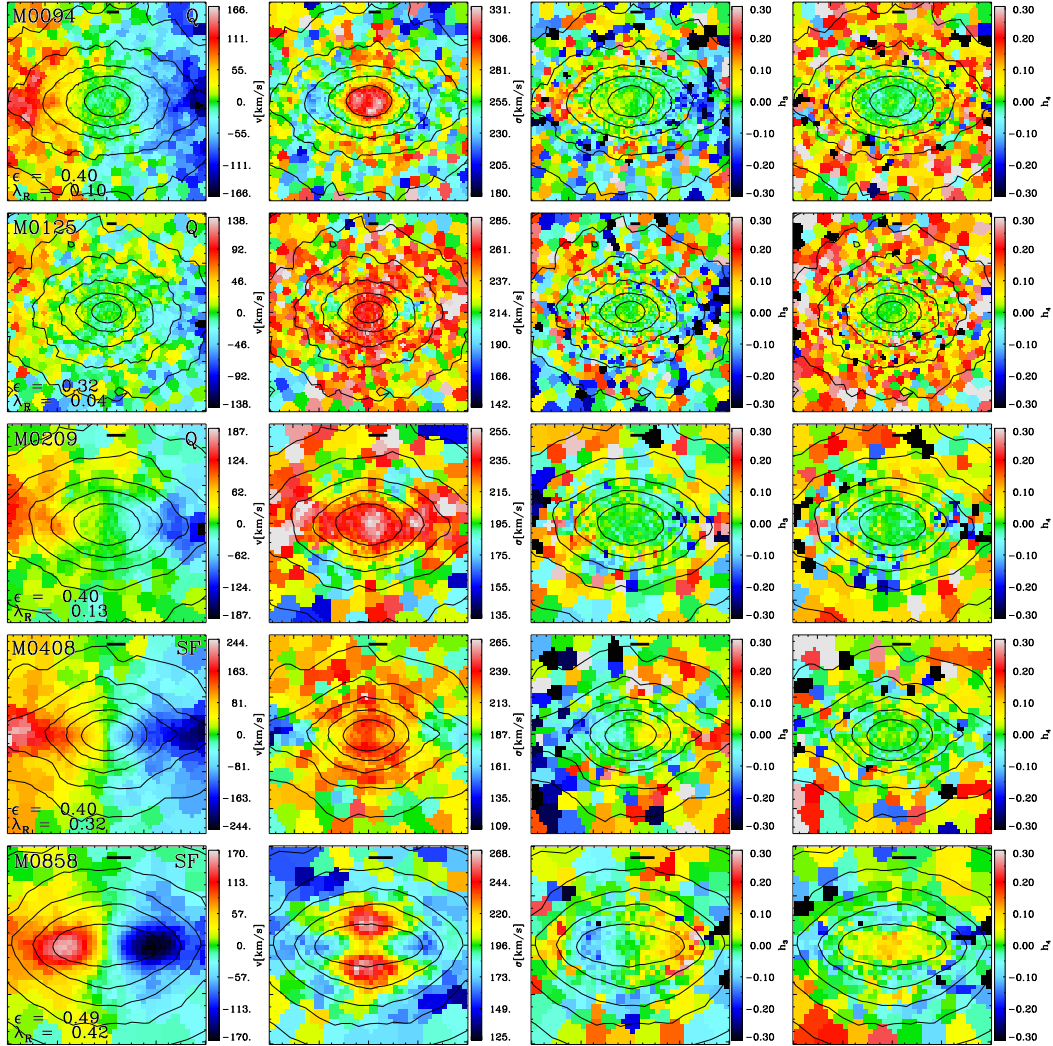


**Figure 7.2:** Kinematic maps for edge-on projections of five simulated galaxies 0094, 0125, 0209, 408, and 0858 (from top to bottom) with characteristic features. The area shown covers a box of 3 projected stellar half-mass radii ( $r_{1/2}$ ) side length. The contour lines show the projected mass surface density. The halo ID, the  $\lambda_R$  parameter (Section 7.3), the ellipticity at  $r_{1/2}$ , and the physical scale of 1kpc (indicated by the black bar) are given in the leftmost panels. From the left to the right we show line-of-sight velocity ( $v$ ), line-of-sight velocity dispersion ( $\sigma$ ), a measure for the asymmetric ( $h_3$ ), and symmetric ( $h_4$ ) deviations from a Gaussian LOSVD shape. Galaxy M0094 has a central counter-rotating component which is also apparent in the  $h_3$  map. M0125 shows very weak rotation not exceeding  $\approx 30\text{km s}^{-1}$  but a very high central velocity dispersion of  $\approx 280\text{km s}^{-1}$ . The maps for  $h_3$  and  $h_4$  are almost featureless. The velocity dispersion of M0209 is enhanced along the major axis, a feature that is attributed to two counter-rotating flattened components. 0408 shows significant rotation (up to  $200\text{km s}^{-1}$ ) and a very regular velocity field. As observed in real galaxies, the  $h_3$  values are anti-correlated to the line-of-sight velocity indicating steep leading winds in the LOSVD. The values for  $h_4$  are slightly positive at the center indicating a more peaked than Gaussian LOSVD. M0858 shows a very characteristic dumbbell feature (i.e. a suppression of the stellar dispersion along the major axis) which is indicative of the presence of a kinematically cold disk component. The maps of all galaxies can be found in the appendix.

et al. 2010; Sawala et al. 2010) and feedback from super-massive black holes dominates for high mass systems (Croton et al. 2006; Di Matteo et al. 2008; Sijacki et al. 2009; Puchwein et al. 2010; Teyssier et al. 2011; McCarthy et al. 2010b). Although the physics is relatively well understood and many individual detailed calculations have shown how these feedback processes can expel the baryons from galaxies, there have been only a few high resolution galaxy formation calculations, using cosmological initial conditions, beginning to master the physics well enough to match either the winds seen in forming galaxies or the final metal distribution between galaxies and the IGM (Scannapieco et al. 2008; Sawala et al. 2010). Some other calculations do successfully allow for winds and for the consequences these winds have on the galaxies and the surrounding ISM (Springel & Hernquist 2003; Oppenheimer & Davé 2008; Oppenheimer et al. 2010b; Cen & Chisari 2011; Wiersma et al. 2010b; McCarthy et al. 2010b). Our computations do not generate significant winds at high redshift (e.g. Steidel et al. 2010) and thus overestimate, by roughly a factor of two to three, the condensed baryon fraction of the most massive galaxies (Guo et al. 2010b; Moster et al. 2010) and we are currently working to implement physically valid feedback implementations to address this problem.

Table 7.1. Table Caption

ID	$M_*$ ( $10^{10}M_\odot$ )	$R_{1/2}$ (kpc)	$\lambda_R$	$\epsilon$	q	s	$M_{ins}/M_*$	$\lambda_H$
(1)	(2)	(3)	(4)	(5)	(6)	(7)	(8)	(9)
M0040	49.98	8.85	0.08	0.37	0.89	0.80	0.23	0.053
M0053	69.45	9.19	0.05	0.39	0.81	0.6	0.24	0.013
M0069	49.41	6.42	0.13	0.43	0.72	0.58	0.22	0.082
M0089	52.33	8.04	0.05	0.47	0.68	0.52	0.16	0.023
M0094	47.9	5.37	0.1	0.41	0.79	0.61	0.26	0.034
M0125	43.36	6.54	0.04	0.32	0.73	0.69	0.23	0.035
M0162	36.44	6.58	0.04	0.54	0.59	0.49	0.13	0.039
M0163	35.2	7.37	0.22	0.44	0.7	0.53	0.15	0.028
M0175	36.79	5.18	0.04	0.31	0.83	0.67	0.27	0.043
M0190	31.48	4.95	0.06	0.56	0.55	0.41	0.15	0.045
M0204	26.86	4.73	0.07	0.21	0.9	0.73	0.16	0.046
M0209	19.96	2.87	0.15	0.4	0.83	0.61	0.34	0.079
M0215	27.64	3.77	0.11	0.26	0.86	0.68	0.35	0.028
M0224	24.84	4.33	0.13	0.28	0.89	0.63	0.2	0.04
M0227	30.88	5.54	0.21	0.32	0.76	0.63	0.13	0.057
M0259	19.83	3.43	0.33	0.39	0.96	0.53	0.26	0.045
M0290	22.04	2.67	0.41	0.29	0.97	0.61	0.28	0.036
M0300	18.65	3.36	0.22	0.47	0.77	0.47	0.2	0.069
M0329	21.33	3.27	0.08	0.35	0.83	0.67	0.34	0.033
M0380	17.08	3.01	0.36	0.37	0.66	0.44	0.5	0.038
M0408	17.71	2.61	0.38	0.45	0.94	0.55	0.3	0.047
M0443	23.08	2.13	0.1	0.29	0.82	0.58	0.41	0.027
M0501	16.31	3.2	0.09	0.38	0.79	0.59	0.36	0.051
M0549	11.64	3.41	0.35	0.29	0.85	0.55	0.27	0.056
M0616	13.03	3.05	0.06	0.42	0.71	0.57	0.37	0.04
M0664	10.39	2.24	0.1	0.26	0.74	0.64	0.35	0.012
M0721	13.37	1.81	0.3	0.48	0.94	0.3	0.54	0.043
M0763	13.68	3.14	0.35	0.35	0.86	0.59	0.2	0.066
M0858	14.26	2.19	0.41	0.47	0.85	0.18	0.36	0.024
M0908	13.43	2.17	0.35	0.43	0.92	0.35	0.46	0.013
M0948	9.23	3.45	0.09	0.21	0.89	0.82	0.31	0.014
M0959	8.41	2.18	0.1	0.35	0.77	0.73	0.37	0.04
M0977	6.32	2.41	0.31	0.55	0.76	0.46	0.5	0.085

Table 7.1—Continued

ID	$M_*$ ( $10^{10}M_\odot$ )	$R_{1/2}$ (kpc)	$\lambda_R$	$\epsilon$	q	s	$M_{ins}/M_*$	$\lambda_H$
(1)	(2)	(3)	(4)	(5)	(6)	(7)	(8)	(9)
M1017	8.87	1.73	0.07	0.42	0.73	0.55	0.59	0.017
M1061	7.2	2.19	0.08	0.44	0.7	0.49	0.34	0.065
M1071	10.82	1.83	0.13	0.23	0.89	0.74	0.32	0.008
M1091	10.46	1.51	0.05	0.38	0.75	0.52	0.28	0.032
M1167	10.24	1.74	0.07	0.41	0.71	0.47	0.33	0.027
M1192	6.05	2.03	0.43	0.48	0.56	0.39	0.45	0.038
M1196	10.74	2.31	0.38	0.48	0.93	0.42	0.49	0.048
M1306	9.04	1.46	0.47	0.37	0.85	0.31	0.45	0.024
M1646	7.47	2.03	0.15	0.49	0.92	0.18	0.49	0.015
M1859	6.27	1.5	0.07	0.35	0.75	0.6	0.43	0.015
M2283	4.7	1.39	0.14	0.47	0.5	0.36	0.49	0.054
M2665	4.4	1.54	0.1	0.27	0.68	0.6	0.44	0.028

Note. — Column (1): ID of the galaxy. Column (2): stellar mass inside  $R_{10}$ . Column (3): projected half-mass radius. Column (4): Column (5): Column (6): intermediate to major axis ratio. Column (7): minor to major axis ratio. Column (8): Ratio of in-situ created to total stellar mass. Column (9): halo spin parameter.

## 7.2 Construction of kinematic maps

So far two-dimensional velocity fields from numerical galaxy simulations have only been constructed and analyzed for remnants of binary merger simulations which provide the necessary resolution for a reliable analysis (Bendo & Barnes 2000; Jesseit et al. 2007, 2009; Hoffman et al. 2009, 2010; Bois et al. 2010, 2011). The high spatial and mass resolution of modern cosmological simulations of individual galaxies makes it now possible to extend the two-dimensional analysis to simulated galaxies that form and evolve in a full cosmological context.

The two-dimensional kinematic maps of the cosmological galaxy simulations presented here are constructed in a similar way as described in Jesseit et al. (2007, 2009), with a few notable differences to follow as close as possible the observers data analysis for the galaxies in the ATLAS<sup>3D</sup> sample. In a first step we identify the central galaxy of the simulated halos and shift all positions and velocities to its baryonic center using a shrinking sphere technique. The stellar component of the galaxy is rotated according to the principle axes of the moment-of-inertia tensor of the 50 per cent most tightly bound stellar particles. As a reference measure we compute the edge-on projected (along the minor-axis) circular half-mass radius,  $r_{1/2}$ , within 10 percent of the virial radius of the galaxy (Oser et al. 2012). For every projected stellar particle within a square of two half-mass radii side lengths, centered on the galaxy, we create a set of 60 pseudo-particles with identical line-of-sight velocities and 1/60th the original particle mass. The pseudo-particles are distributed in the plane of the sky according to a two-dimensional Gaussian with a standard deviation of 0.4 kpc. This way we account for seeing effects on the projected mass and velocity distribution and the limited spatial resolution of the simulations.

All pseudo-particles are binned on a spatial grid, centered on the projected particle position with two-half-mass radii side length and a pixel size of 277pc. The grid has variable dimensions depending on the projected size of the galaxy. Our chosen pixel size approximately corresponds to the spatial coverage of one lenslet of the SAURON instrument (Bacon et al. 2001) at a distance of  $20Mpc$ . In contrast to simulations, real galaxies are observed with an instrument of fixed angular coverage and the spatial coverage varies between 0.5 and 3 effective radii depending on the physical size and distance of the galaxies (Cappellari et al. 2011a).

Using the regularly binned spatial data we group, whenever necessary, adjacent bins into larger bins with a comparable pre-defined signal-to-noise ratio using a Voronoi tessellation method as described in Cappellari & Copin (2003). This results in an irregular grid structure but guarantees that all bins contain approximately the same number of particles. From the velocity data we construct line-of-sight velocity profiles for each Voronoi bin along the two-dimensional grid.

To get a quantitative measurement for the deviations of the LOSVD from the Gaussian shape the velocity profile  $P(v)$  can be parametrized in accordance with Gerhard (1993) and van der Marel & Franx (1993) by a Gaussian plus third- and fourth-order

Gauss-Hermite functions (see Bender et al. 1994)

$$P(v) = \gamma \frac{\alpha(w)}{\sigma} [1 + h_3 H_3(w) + h_4 H_4(w)], \quad (7.1)$$

where  $w = (v - v_{\text{fit}})/\sigma_{\text{fit}}$  and

$$\alpha(w) = \frac{1}{\sqrt{2\pi}} e^{-w^2/2} \quad (7.2)$$

$$H_3(w) = \frac{1}{\sqrt{6}} (2\sqrt{2}w^3 - 3\sqrt{2}w) \quad (7.3)$$

$$H_4(w) = \frac{1}{\sqrt{24}} (4w^4 - 12w^2 + 3). \quad (7.4)$$

$H_3$  and  $H_4$  are the standard Hermite polynomials as defined by

$$\left(-\frac{d}{dx}\right)^j \alpha(x) = \sqrt{j!} H_j(x/\sqrt{2}) \alpha(x). \quad (7.5)$$

The  $H_j$  form a set of orthogonal functions,  $u_i = \exp(-w^2/2) \times H_i(w)$  are the Gauss-Hermite basis functions, and  $h_3$  and  $h_4$  are their amplitudes which represent the skewness and the kurtosis of the velocity profile, respectively. Note that the skewness/kurtosis and  $h_3/h_4$  are not identical. The skewness and kurtosis are the normalized third- and fourth-order moments of the LOSVD and are more susceptible to the wings of the line profile which are ill-constrained by the observations (see van der Marel & Franx 1993).  $\gamma$  is a normalization constant. If the LOSVDs deviate from a Gaussian, the fit parameters  $v_{\text{fit}}$  and  $\sigma_{\text{fit}}$  correspond only to first order to the real first ( $v_{\text{los}}$ ) and second ( $\sigma_{\text{los}}$ ) moment of the velocity distribution (differences of up to 15%, see Bender et al. 1994; Magorrian & Binney 1994). For  $h_3 = 0$  and  $h_4 = 0$  the resulting velocity profile is a Gaussian. For asymmetric profiles with the prograde (leading) wing steeper than the retrograde (trailing) one,  $h_3$  and  $v_{\text{fit}}$  have opposite signs. This corresponds to a negative  $h_3$  as defined by observers (van der Marel & Franx 1993; Bender et al. 1994; Fisher 1997)). When  $v_{\text{fit}}$  and  $h_3$  have the same sign, the leading wing is broad and the trailing wing is narrow. LOSVDs with  $h_4 > 0$  have a 'triangular' or peaked shape, here the distribution's peak is narrow with broad wings. Flat-top LOSVDs have  $h_4 < 0$  where the peak is broad and the wings are narrow. The kinematic parameters of the LOSVD in each Voronoi bin ( $v_{\text{fit}}$ ,  $\sigma_{\text{fit}}$ ,  $h_3$ ,  $h_4$ ) are determined following the procedure described in van de Ven et al. (2006) which is particularly suitable for our purposes. Whenever indicated we repeat this analysis for different projections of the galaxies on the plane of the sky.

In Fig. 7.2 we show, as an example, the two-dimensional maps for the line-of-sight velocity ( $v$ ), line-of-sight velocity dispersion ( $\sigma$ ), a measure for the asymmetric ( $h_3$ ), and symmetric ( $h_4$ ) deviations from a Gaussian LOSVD shape, within  $3r_{1/2}$  of five galaxies (M0094, M0125, M0290, M0408, M0858 from top to bottom). Maps for the whole sample are presented in Figs. A.1 - A.8 of the appendix. The contour lines indicate the projected mass surface density. The halo ID, the  $\lambda_R$  parameter (Section

7.3), the ellipticity at  $r_{1/2}$ , and the physical scale of  $1kpc$  (indicated by the black bar) are given in the leftmost panels. In general, the quality of the maps is very good and rotation, kinematic substructure, and higher-order kinematic features are clearly visible, quantifiable and have similar amplitudes than observed in real galaxies.

Galaxy 0094 (top row in Fig. 7.2) is a slowly rotating galaxy with a counter-rotating core. This feature is also apparent in the  $h_3$  map. Galaxy 0125 is an example for a galaxy with very weak rotation not exceeding  $\approx 30kms^{-1}$ . The central velocity dispersion is very high, at a value of  $\approx 280kms^{-1}$  and dropping towards larger radii. The maps for  $h_3$  and  $h_4$  show almost no features with values scattering around zero. The velocity dispersion of the rotating galaxy 0209 is enhanced along the photometric major axis, a feature that is attributed to two counter-rotating flattened components (Emsellem et al. 2004). A galaxy with significant rotation (up to  $200kms^{-1}$ ) and a very regular velocity field is 0408. As observed in real galaxies (Bender et al. 1994; Krajnović et al. 2008, 2011), the  $h_3$  values are anti-correlated to the line-of-sight velocity indicating steep leading wings of the LOSVD and the amplitudes in are of the same order of magnitude. The values for  $h_4$  are slightly positive at small projected radii corresponding to a LOSVD that is more peaked than a Gaussian at the center with broader wings, also in general agreement with observations. 0858 shows a very characteristic dumbbell feature (i.e. a suppression of the stellar dispersion along the major axis, see e.g. Emsellem et al. (2004)) which is indicative of the presence of a central kinematically cold disk component

### 7.3 Fast and slow rotators

From the two-dimensional velocity maps we compute the  $\lambda_R$ -parameter as introduced by Emsellem et al. (2004) according to

$$\lambda_R = \frac{\sum_{i=1}^{N_p} F_i R_i |V_i|}{\sum_{i=1}^{N_p} F_i R_i \sqrt{V_i^2 + \sigma_i^2}}, \quad (7.6)$$

where  $F_i$  is the flux (here the projected mass in every bin),  $R_i$  the projected radius,  $v_i$  the line-of-sight velocity and  $\sigma_i$  the line-of-sight velocity dispersion of each grid cell. These properties are determined as explained in the previous section and we can therefore calculate  $\lambda_R$  as a function of radius for every galaxy from its two-dimensional map (Jesseit et al. 2009). When computing a characteristic value of  $\lambda_R$  we have to consider that *ATLAS<sup>3D</sup>* has a finite field-of-view which typically extends to 0.3 - 3 effective radii. To take this into account we determine the half-mass radius for each projection and sum only over the grid cells inside one effective radius. Thus we ensure a fair comparison to the *ATLAS<sup>3D</sup>* data. The global values of  $\lambda_R$  for our galaxies are given in Tab. 7.1 as well as in the left panels of Figs. 7.2 and A.1 - A.8

In Fig. 7.3 we show the variation of  $\lambda_R$  as a function of radius for the edge-on projections of all simulated galaxies up to two projected half-mass radii. Galaxies with slowly rising profiles up to the half-mass radius are mostly identified as slow rotators

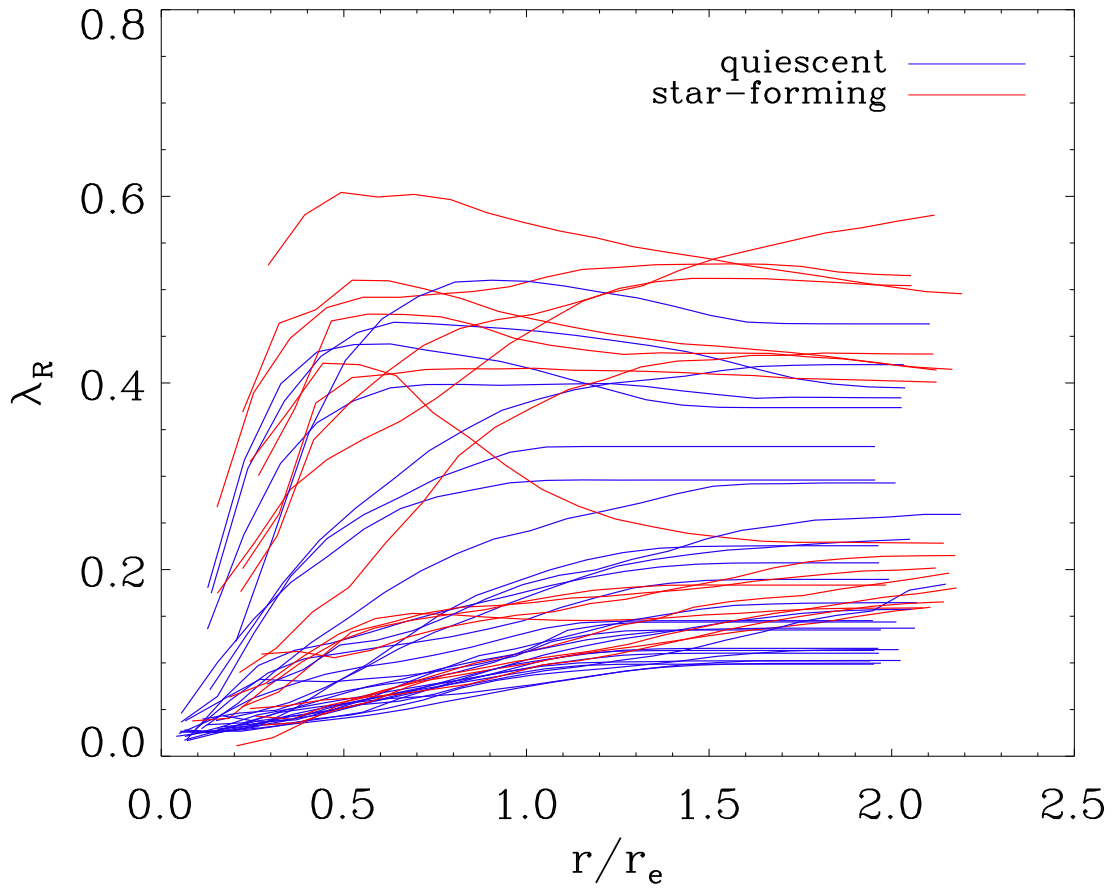


**Figure 7.3:**  $\lambda_R$  profiles for the simulated galaxy sample up to two half-mass radii. Galaxies with slowly rising profiles are mostly identified as slow rotators and galaxies with steeply rising profiles are fast rotators. The profiles of quiescent galaxies (SSFR  $< 0.3/t_{hub}$ ) are shown in blue those of star-forming galaxies in red. The amplitude of  $\lambda_R$  as well as the characteristic profile shapes are in agreement with observed ETGs (Emsellem et al. 2004, 2011).

and galaxies with steeply rising profiles are fast rotators. The slow rotators ( $\lambda_R < 0.1at_{r_e}$ ) are mostly quiescent galaxies (specific star formation rate  $< 0.3/t_{\text{hub}}$ , blue) fast rotators can be quiescent or star-forming (red). The amplitude of  $\lambda_R$  as well as the characteristic profile shapes are in agreement with observed ETGs (Emsellem et al. 2004, 2011). Similar to observed galaxies we also find steeply rising and then falling profiles. These particular profile shape corresponds to galaxies with rapid rotation at their centers which almost then drops to zero in the outer parts. The clearest case is M1646 whose kinematic map can be found in Fig. A.7 in the appendix.

The location of the galaxies in the  $\lambda_R$  - galaxy mass plane is shown in Fig. 7.4 for all edge-on projections. The location approximately corresponding to slow ( $\lambda_R < 0.1$ ) is indicated by the shaded area. We can see two clear trends here. At low masses the distribution is bi-modal with a group of galaxies with low  $\lambda_R \approx 0.1$  and another group of fast rotators with the highest  $\lambda_R \approx 0.5$ . Towards higher masses  $\lambda_R$  continuously decreases and the high-mass end of our sample is dominated by slowly rotating galaxies. This trend is in remarkable agreement with the observed *ATLAS<sup>3D</sup>* galaxies (see Emsellem et al. (2011), Fig. 3). However, our presentation is biased in two ways. First, the simulated galaxy sample was randomly picked from a larger simulated volume and is not statistically complete. Second, we show only the edge-on projection, whereas real galaxies can be assumed to be oriented randomly on the sky. To estimate the second effect we plot in Fig. 7.4 the results for  $\lambda_R$  for 50 random projections of every galaxy as small dots and their average value as empty circles. The bi-modality is less pronounced for the average values but the trend for  $\lambda_R$  to decrease with increasing galaxy mass is unaffected.

In Fig. 7.5 we show the  $\lambda_R$ -parameter as a function of the projected ellipticity at  $r_{1/2}$ . The roundest galaxies are slow rotators. At higher Ellipticities many galaxies are fast rotators. We again show the results of 50 random projections for all the simulated galaxies as dots. Whereas the ellipticity decreases significantly for all non-edge-on projections,  $\lambda_R$  stays roughly constant over a wide range. With the projections taken into account, we find a good agreement to observed values for  $\lambda_R$  and ellipticities (Emsellem et al. 2011).

We showed in chapter 5 that massive galaxies in this sample grow in two phases. A first phase down to  $z \approx 2$  is dominated by in-situ star formation inside the galaxy and a second phase at  $z < 2$ , which is dominated by accretion of stellar systems that have formed outside the galaxy and are then accreted at lower redshifts. This growth mechanism was shown to be the most plausible growth mechanism for massive early-type galaxies (Khochfar & Silk 2006a; Naab et al. 2009). Towards lower galaxy masses in-situ star formation becomes more important and the stellar accretion rates drop. In this scenario it is plausible to assume that galaxies with a more dissipative formation history rotate faster. There is large scatter (see Fig. 7.6) in the correlation between  $\lambda_R$  and the fraction of in situ created stars, with the galaxy with the highest fraction of in situ formed stars (M1017) in the sample being a slow rotator. However the trend (linear fit represented by the dotted line in Fig. 7.6) indicates an increasing value for  $\lambda_R$  for an increasing fraction of stars formed inside the galaxy itself suggesting that

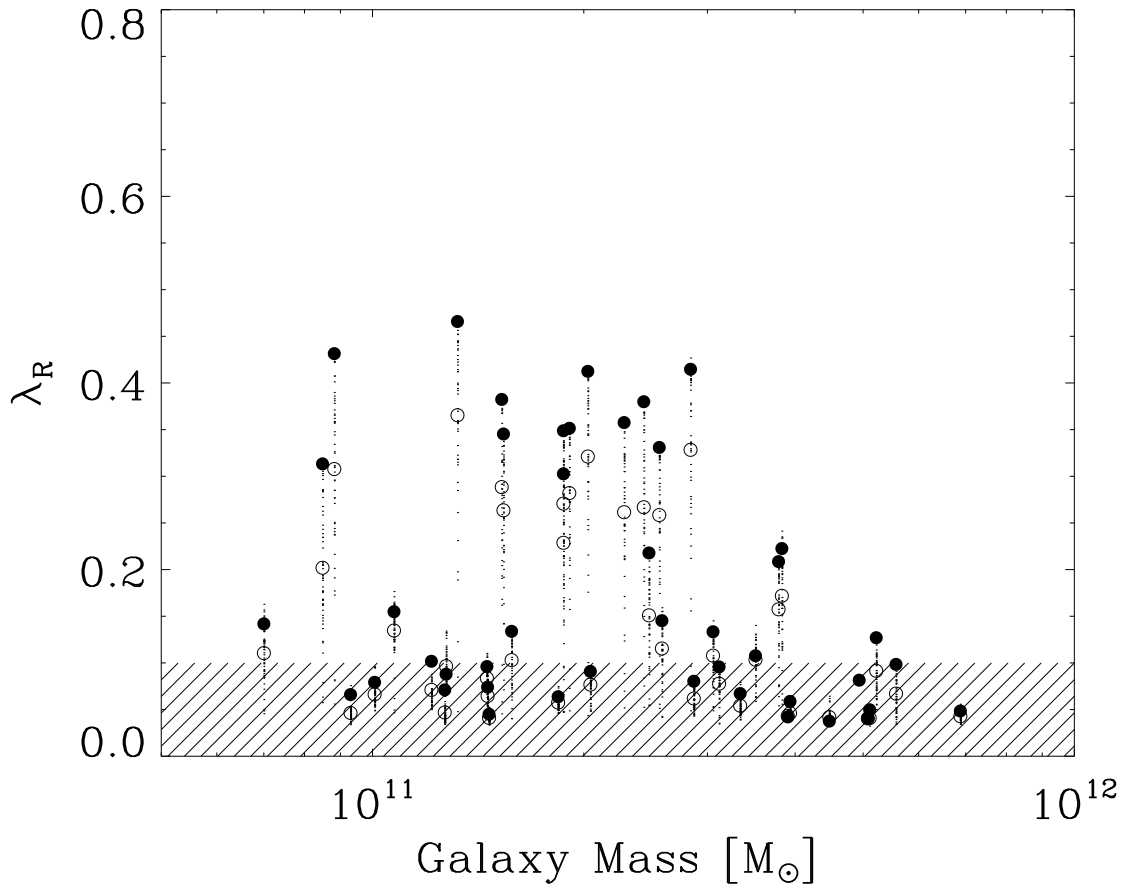


**Figure 7.4:** Stellar mass of the simulated galaxies versus the  $\lambda_R$  parameter measured in the edge-on projection (filled circles). The dots show the results of 50 random projections, the empty circles indicate the mean values for  $\lambda_R$  for the projections. Massive galaxies tend to be slow rotators. Less massive galaxies can be slow as well as fast rotators. This is in qualitative agreement with the *ATLAS<sup>3D</sup>* galaxies (Emsellem et al. 2011).

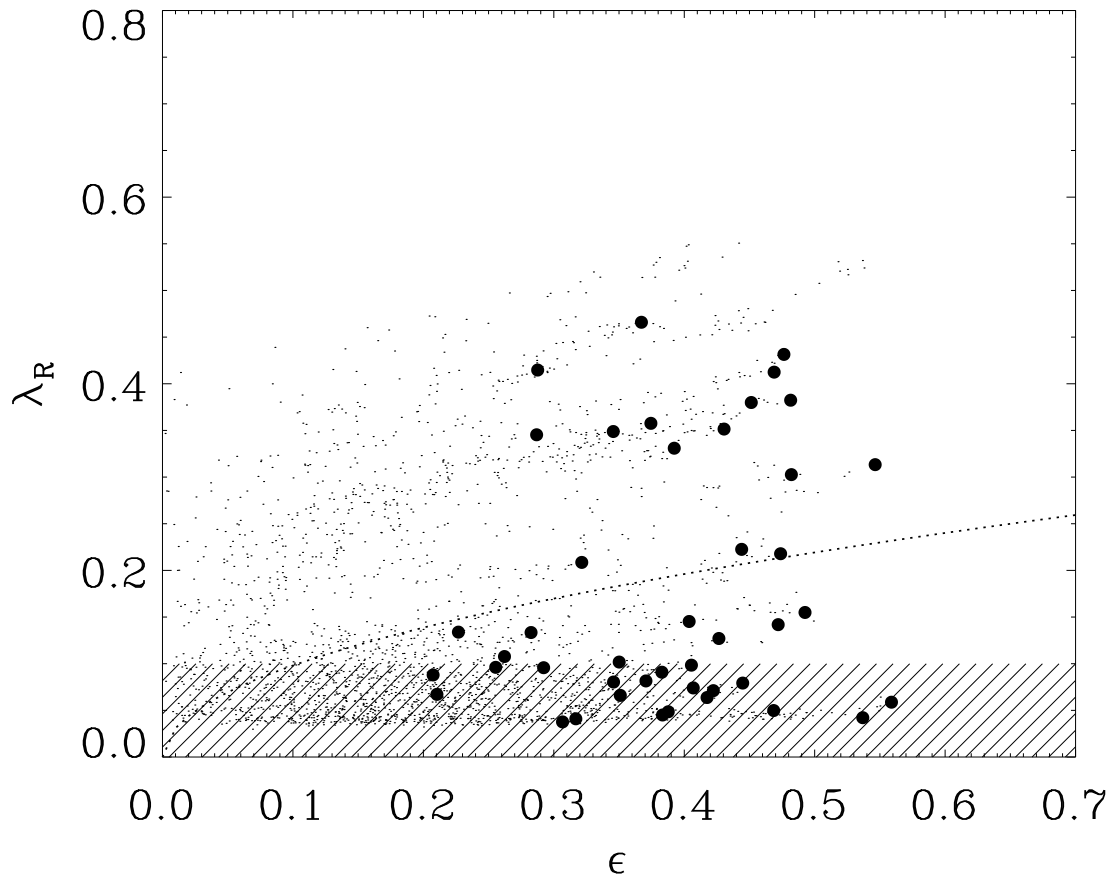


**Figure 7.5:** Ellipticities of the simulated early-type galaxies versus the  $\lambda_R$  parameter measured in the edge-on projection (filled circles). The shaded area indicates again the limit for slow rotating galaxies. The dotted line shows the limit for slow rotators ( $< 0.3 \times \epsilon^{-1/2}$ ) as defined in Emsellem et al. (2011). Round galaxies tend to be slow rotators whereas very elongated galaxies can be both fast and slow rotating. The ellipticity drops fast for non-edge-on projections (dots), whereas  $\lambda_R$  falls off only for projections where the galaxy shape is approaching spherical symmetry.

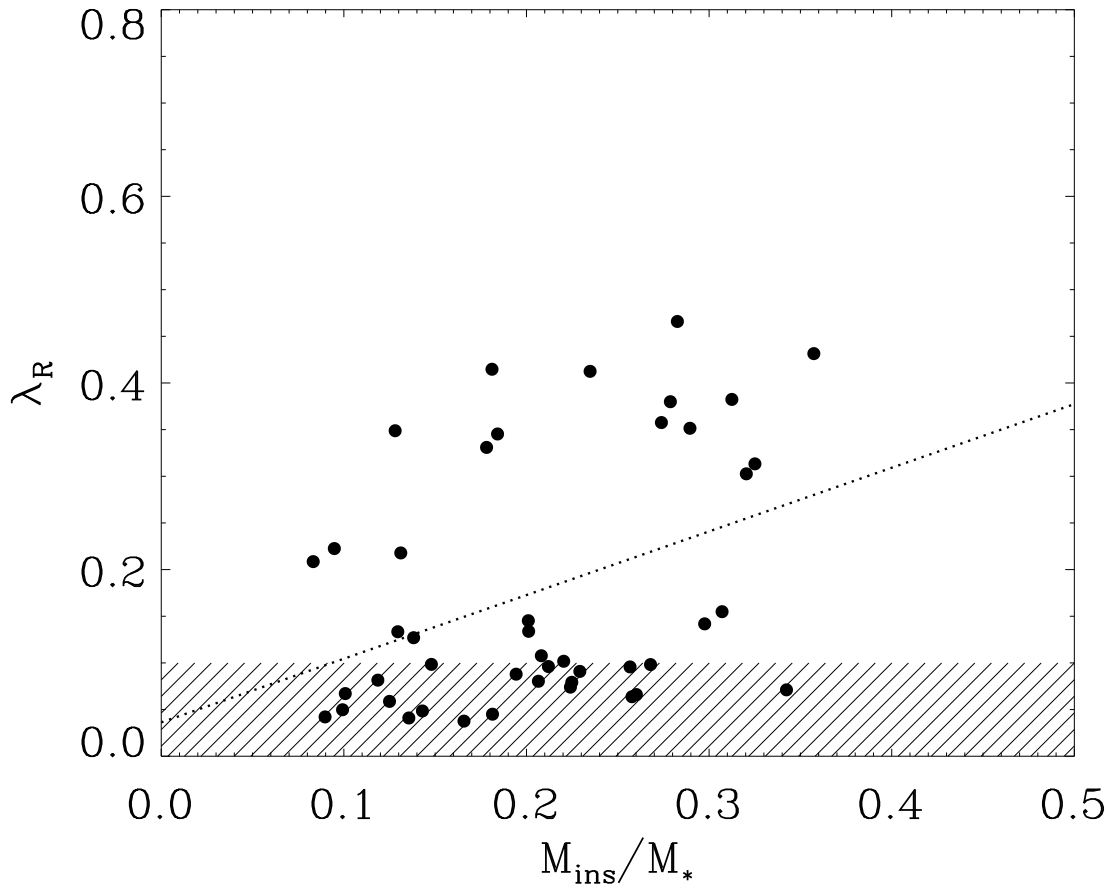


**Figure 7.6:** Fraction of stars formed in the galaxy  $N_{*,\text{ins}}$  to those formed outside the galaxy and accreted later-on  $N_{*,\text{acc}}$  versus the  $\lambda_R$  parameter measured in the edge-on projection.  $N_{*,\text{ins}}/N_*$  can be considered as an estimate of the importance of dissipative processes inside the main galaxy during its formation. The dotted line represents the linear fit to the plotted values indicating that  $\lambda_R$  is increasing with an increasing fraction of in situ created stars.

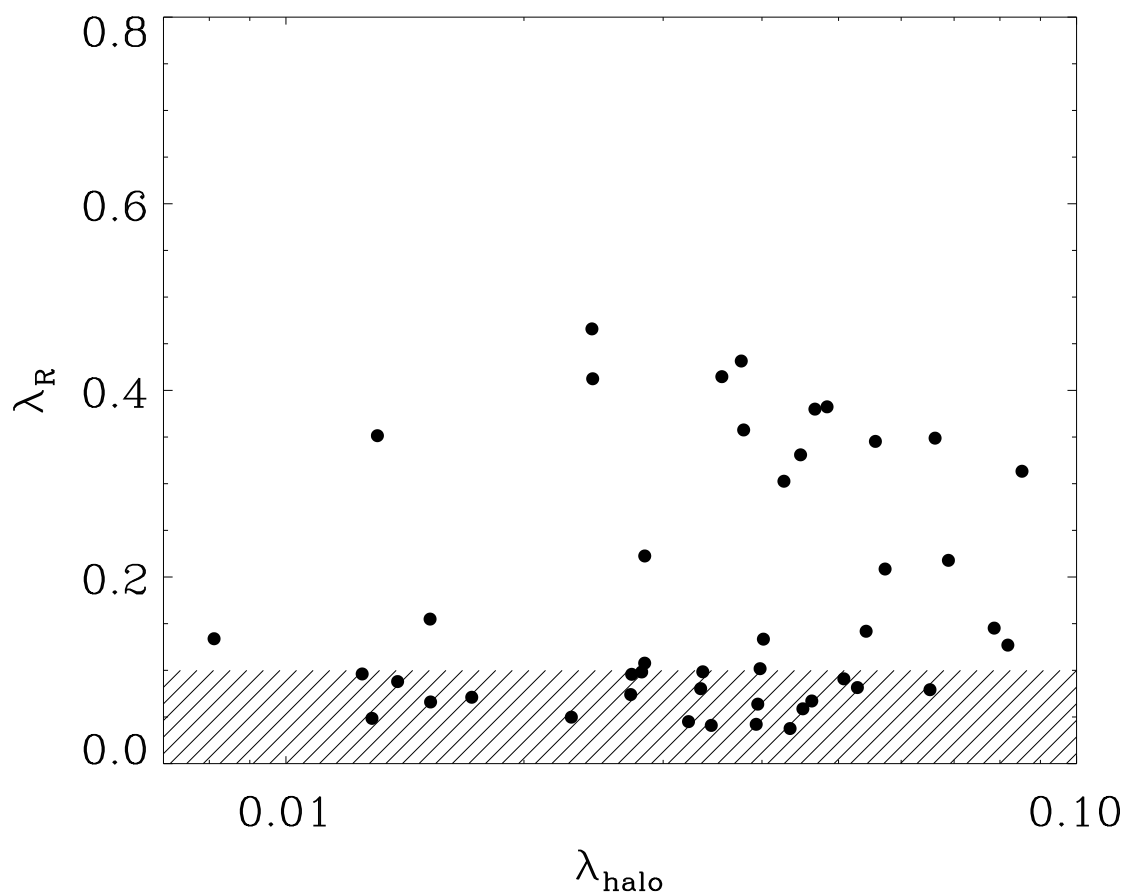


**Figure 7.7:** Spin parameter of the dark matter halo,  $\lambda$  versus the  $\lambda_{\text{R}}$  parameter measured in the edge-on projection. Galaxies with low halo spin tend to be slow rotators whereas galaxies with high halo spin can host slow as well as fast rotating galaxies.

dissipational effects during galaxy formation are important in defining the rotational properties.

Intuitively, the exception could be, that  $\lambda_R$  is simply set by the total angular momentum imprinted onto the system in the initial conditions. In Fig. 7.7 we show the dependence of  $\lambda_R$  on the dimensionless spin parameter as introduced in section 4.6.1. There is no obvious correlation indicating that dissipational effects are important that lead to different evolution of the angular momentum in the baryonic matter as compared to the dark matter. Halos with a small spin parameter almost exclusively host galaxies with little rotational support whereas halos with a large spin parameter host fast rotators as well as slow rotators. This suggests that it is easier for the baryonic components to lose angular momentum in the process of forming galaxies than to gain it. Idealized merger simulations (Bois et al. 2010, 2011) conclude, that slow rotators form as the result of major mergers. At lower mass fractions (below 0.5) the resulting remnant is almost always fast rotating. We however find that the repeated accretion of smaller systems (see Fig. 7.1) is a valid mechanism to form slowly rotation ETGs. In Fig. 7.8 we show  $\lambda_R$  as a function of the highest merger ratio encountered by the galaxy between redshift 2 and 0. We find no evidence for major mergers being particularly important for the formation of slow rotators. Some of them encounter major mergers but others do not have any major at all. The same is true for the fast rotators, indicating that the ratios of preceding mergers are of minor importance.

In Fig. 7.9 we show the accretion history and the evolution of the specific angular momentum for the galaxy with the lowest value for  $\lambda_R$  in our sample. The significant build up stellar mass between redshift 2 and the present day is not followed by an increase of the angular momentum instead it decreases almost continuously. At redshift 0 the galaxy is a slow rotator and has a value of  $\lambda_R$  of 0.04. In the lower panel we show the amount of identified mergers (see section 6.4) in the same time. This particular galaxy has no major ( $> 0.25$ ) merger at all between redshift 2 and 0. We find that major mergers are not necessary for the development of slowly rotating systems.

Fig. 7.10 shows a further example for the evolution of stellar mass and specific angular momentum. The galaxy presented encounters two major mergers since redshift 2. While the first one at  $z \approx 1.3$  is not followed by a significant change of the specific angular momentum the second one at  $z \approx 0.45$  leads to a steep rise in the specific angular momentum. At the present day the galaxy is a fast rotating ETG with a value for  $\lambda_R$  of 0.38. Overall the role of major mergers seems to be ambiguous.

## 7.4 Conclusions and Discussion

We present the first detailed analysis of projected stellar kinematic properties of cosmological hydrodynamical simulations. The two-dimensional maps of the stellar velocity, velocity dispersion and higher-order Gauss-Hermite moments for the 45 simulated early-type galaxies described here can be found in Figs. A.1 to A.8. We recover the same diversity in kinematic properties as in the observations including slow and

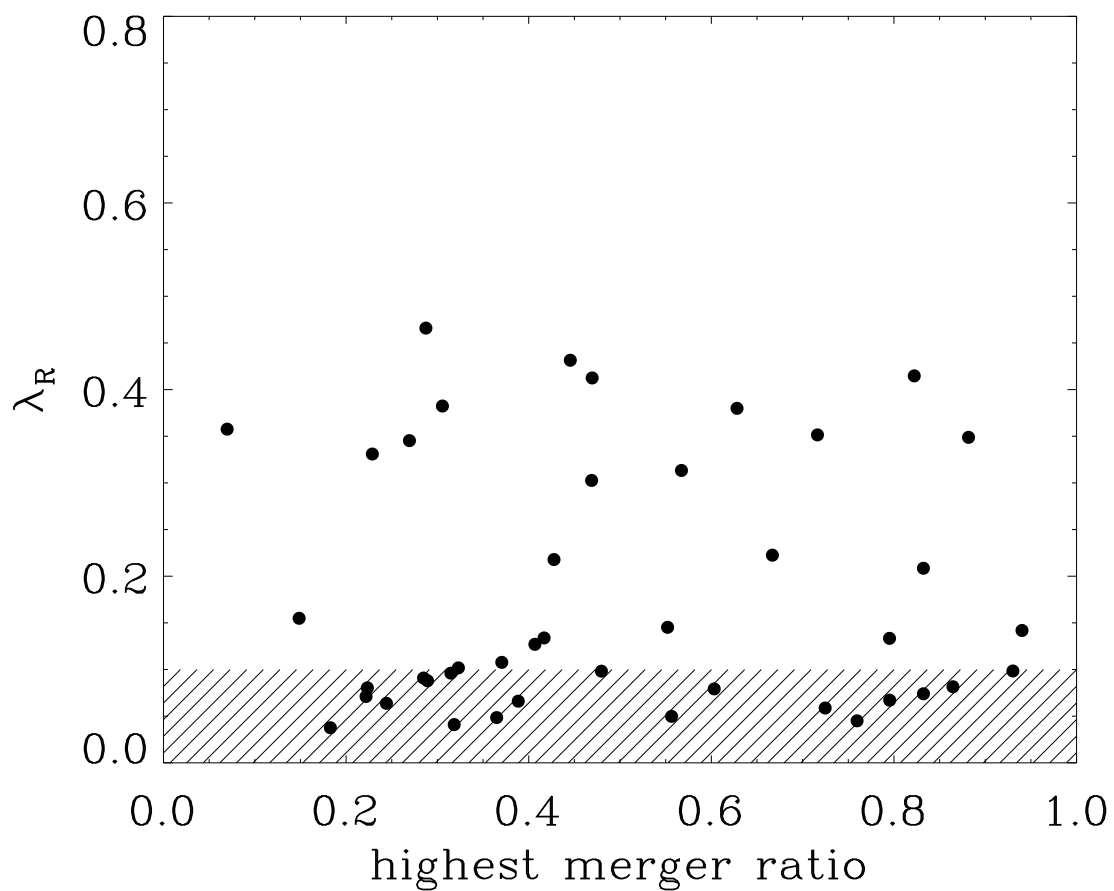


**Figure 7.8:** The highest merger ratio of all the mergers between redshift 2 and 0 vs.  $\lambda_R$ . Slow rotators form as the result of minor as well as major mergers, the same is true for the slow rotators.

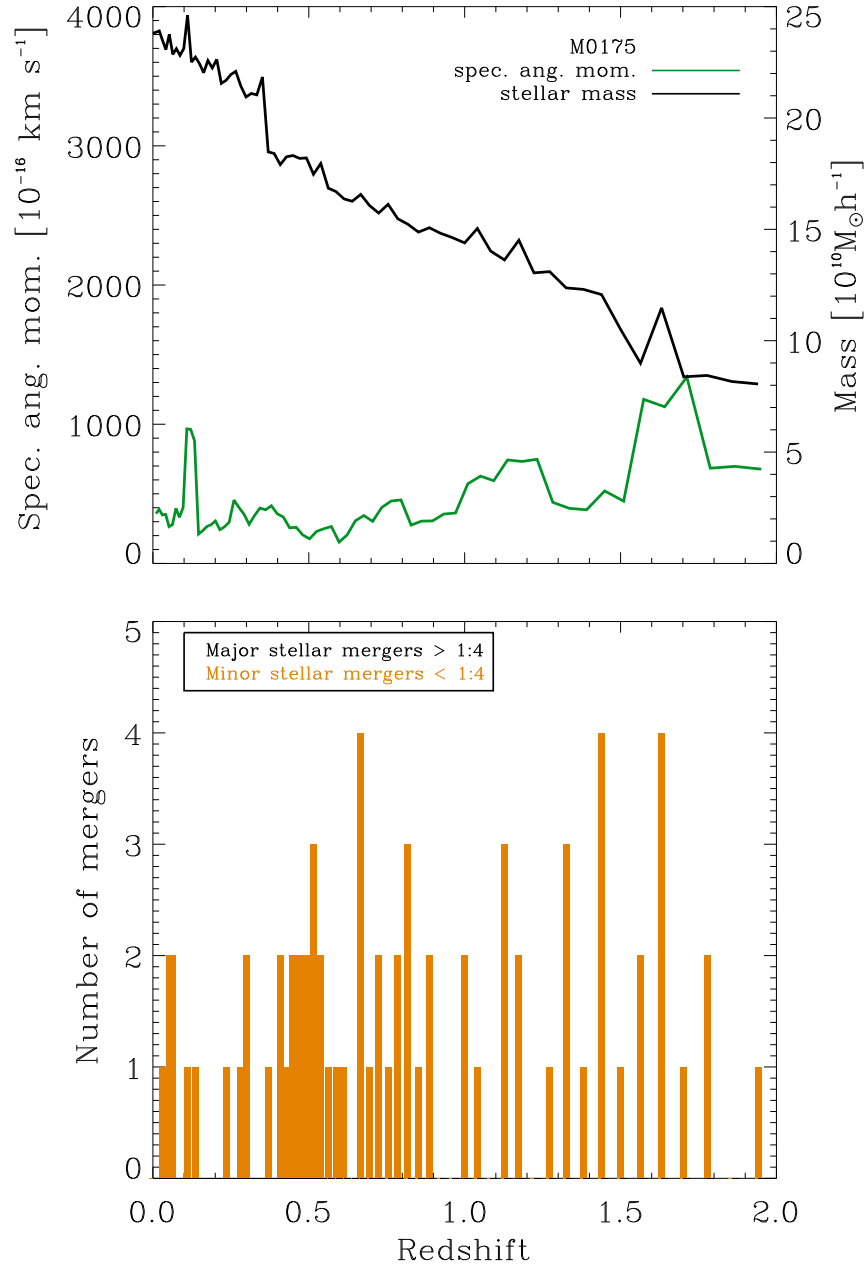


**Figure 7.9:** The upper panel shows an example for the evolution of the specific angular momentum and stellar mass between redshift 2 and the present day. In the lower panel we show the number of identified minor ( $< 0.25$ , orange) and major ( $> 0.25$ , black) mergers in the same timespan. The galaxy shown has no major merger - its merger tree is depicted in Fig. 7.1. - and the build up of stellar mass is accompanied by a steady decrease of the specific angular momentum. At redshift 0 the result is a slow rotator with a value for  $\lambda_R$  of 0.04.

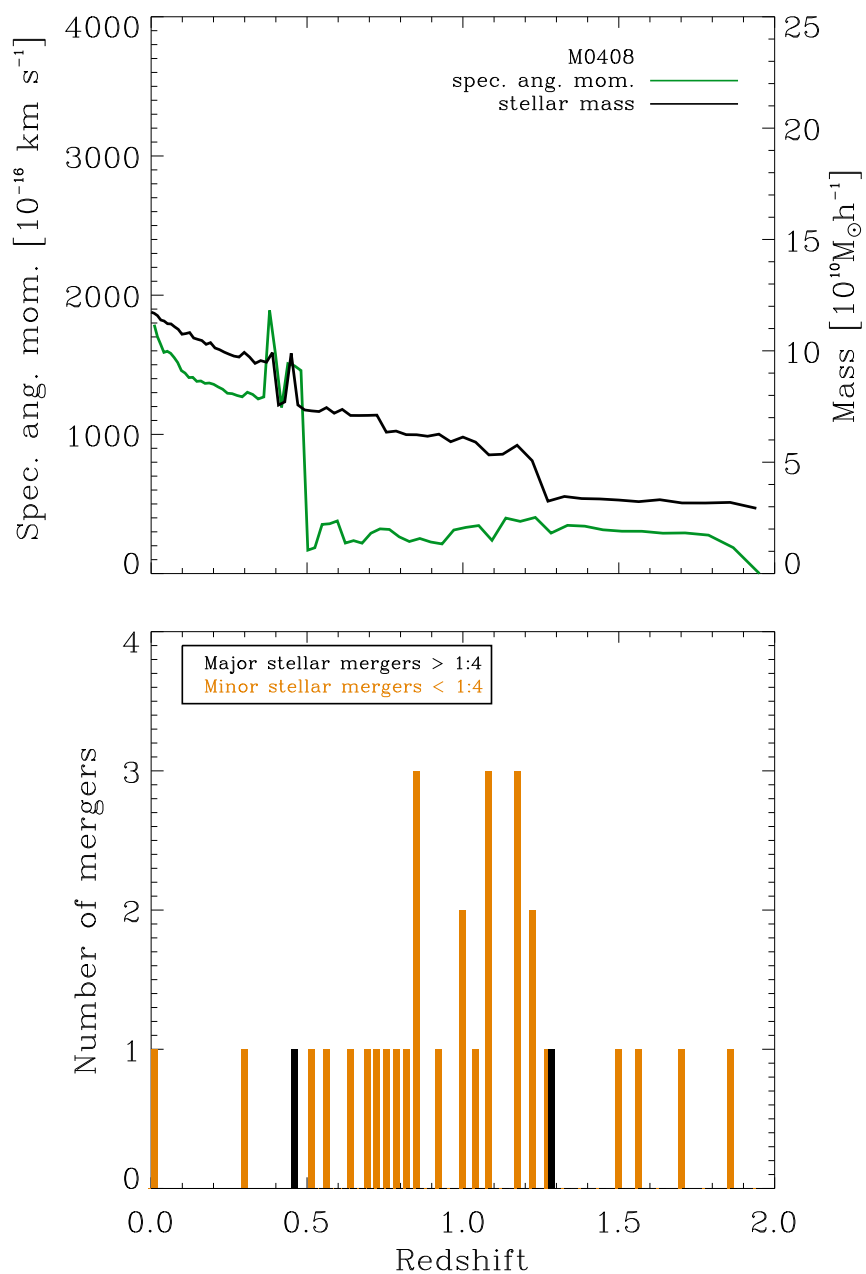


**Figure 7.10:** Another example (M0408) with two major mergers. The first one  $z \approx 1.3$  has almost no effect on the specific angular momentum of the system. The second one at  $z \approx 0.45$  is followed by a significant increase of the specific angular momentum. At redshift 0, the galaxy is a fast rotator with a value for  $\lambda_R$  of 0.38.

fast rotators as well as misaligned and counter-rotating components. We use the  $\lambda_R$ -parameter introduced by Emsellem et al. (2004) to quantify the amount of rotation in the simulated galaxies. Our simulations support the observed trend that a significant fraction of early-type galaxies show a large amount of rotational support.

At lower masses ( $\sim 10^{11}M_\odot$ ) we find slow ( $\lambda_R < 0.1$ ) as well as fast ( $\lambda_R > 0.1$ ) rotators, whereas at the high mass end ( $> 4 \times 10^{11}M_\odot$ ) slow rotators are dominant, a trend that can also be found in observations. We find flat and steeply rising radial  $\lambda_R$ -profiles when we analyze the kinematics up to two effective radii from the center. When we take projection effects into account in the simulations the most spheroid systems tend to be slow rotators. Again these results follow the observed trends. Overall we conclude that the simulated galaxies presented here are able to reproduce the kinematic diversity observed in local early-type galaxies.

We find that dissipational effects are important for the formation of fast rotators, with galaxies that show a high fraction of in situ (dissipational) created stars having larger values of  $\lambda_R$ . The total amount of angular momentum in the halo seems to be less important as well as the mass ratios of recent mergers. In contrast to recently published results, in our simulations slow rotators can form as the result of several minor mergers, major merger are neither necessary nor do they prevent the build up of systems with little rotational support. We show an example (Fig. 7.9) of a slowly rotating system that formed without any major mergers at redshifts below 2. In this case the specific angular momentum of the galaxy decreases as the result of the continuous accretion of smaller systems. The role of major mergers is ambiguous, we find no dependence of  $\lambda_R$  to the mass ratios of mergers encountered since redshift 2.



## Conclusions & Outlook

In order to investigate the formation and evolution of massive early-type galaxies, we performed the so far largest sample of cosmological, high resolution 'zoom-in' simulations spanning a halo mass range of nearly two orders of magnitude. Starting from a dark-matter only simulation of a cosmological volume  $(100 \text{ Mpc}/h)^3$  we picked over 50 halos and resimulated them at higher resolution, including hydrodynamics, radiative cooling and heating, star formation and supernovae feedback. This way we were able to simulate a set of massive galaxies with properties similar to observed early-type galaxies from cosmological initial conditions (Oser et al. 2010, 2012).

We find that galaxies generally form in a two phase process. The early phase ( $z > 2$ ) of star formation is dominated by dissipative assembly where in situ star formation is sustained by cold gas streams (Kereš et al. 2005). At later times ( $z < 2$ ) the assembly of stellar mass is driven by the accretion of stellar systems. While the in situ created stars typically form compact systems nearly independent of their stellar mass, the accreted stars are added to the outer regions of the galaxies establishing the mass-size relation. We find that the dominance of accretion over in situ star formation is mass dependent with more massive systems containing a higher fraction of accreted stars at the present day rendering more massive galaxies larger. This also explains the observational phenomenon usually referred to as 'archaeological downsizing' where the most massive galaxies are made out of the oldest stars (Thomas et al. 2005; De Lucia et al. 2006). This seems to be in contradiction with the picture of hierarchical structure formation in which the most massive systems are assembled last. We find that the more massive systems indeed assemble late, they show a strong mass growth even at low redshifts with is primarily due to accretion of stars that already formed at high redshifts, leading to large mean stellar ages in those systems. In less massive systems, in situ star formation is a significant contribution to the stellar mass growth even at late times and the ratio of accreted to in situ formed stars is typically lower. This results in overall younger stellar populations.

Furthermore we studied in detail the size and velocity dispersion evolution of the resimulated galaxies on cosmological timescales (Oser et al. 2012). We find, that the

strong size increase and mild drop in central line-of-sight velocity dispersions, between redshift two and the present day, of our simulated galaxies can be explained with the above mentioned two-phase assembly scenario. Due to the dissipative character of early galaxy formation, the systems at high redshift ( $z > 3$ ) are compact with sizes of  $r \lesssim 1.3\text{kpc}$ . Until the present day the galaxies grow by accretion and increase their sizes. The most massive systems show the highest fraction of accreted stars at redshift zero and encounter the strongest size increase. The evolution of sizes and velocity dispersion with redshift of the simulated galaxies as well as the present day mass-size relation are in agreement with observations (see chapter 6 Figs. 6.1 and 6.4). Galaxy surveys find a population of massive quiescent galaxies already in place at redshift 2 which is missing in the local universe (Taylor et al. 2010; van Dokkum et al. 2010). We identified all stellar mergers that the simulated galaxies are encountering with a mass ratio of 1:100 or higher. We find that the size growth experienced by the massive galaxies in our simulations is the result of successive minor and major merging events between redshift two and zero. Minor mergers are particularly efficient in increasing galaxy sizes and we find that indeed the stellar mass that is accreted onto the galaxies is added typically in mergers with a ratio of 1:5. In our simulations the size growth is in agreement with simple virial predictions on the basis of the identified stellar merger events.

We present the first detailed two-dimensional analysis of the stellar kinematics in cosmological hydrodynamical simulations. We recover the observational result that a large fraction of early-type galaxies show a significant amount of rotation. We divide the sample of simulated galaxies in slow ( $\lambda_R < 0.1$ ) and fast ( $\lambda_R > 0.1$ ) rotators according to the  $\lambda_R$ -parameter introduced by Emsellem et al. (2004) and find its relation to ellipticity and stellar mass in the simulations to be similar to the observed values, with the most massive galaxies being dominated by slow rotators. The simulated galaxies show the same diversity in kinematic properties than observed local early-type galaxies with misaligned rotation and we even find one example of a counter-rotating central component. We find, that dissipational effects are important for the evolution of slow rotators: the  $\lambda_R$ -parameter is increasing for an increasing fraction of in situ created stars and on the other hand there is almost no correlation of  $\lambda_R$  to the dimensionless spin parameter (see Section 4.6.1). Contrary to recently published results we find no dependence of the  $\lambda_R$ -parameter on the mass fractions of the encountered mergers. Idealized merger simulations produce slow rotators as the result of major mergers. In the cosmological simulations presented here, slow and fast rotators form out of major as well as minor mergers. In fact we present an example for a slowly rotating galaxy (see Fig. 7.9) that has no major ( $> 1 : 4$ ) merger at all between redshift 2 and 0.

Additionally to the work presented in this thesis the simulations performed in the course of this work have been and will be used to study various astrophysical problems. Moster et al. 2010 used the dark matter only simulation for halo occupation models. In Genel et al. 2010 the same initial conditions are evolved with an adapted version of GADGET to investigate the lifetime of star-forming clumps in gas-rich galaxies at redshift 2. A comparison of our simulations to semi-analytic models is presented in

---

Hirschmann et al. 2011. Lyskova et al. (2011, submitted) utilizes the simulation models here to test mass estimators meant to yield reliable galaxy masses from minimal observational data.

This progress in understanding the formation and evolution of massive galaxies is promising but we will need to improve the models used in our simulations in the future to study the effects of galactic winds and active galactic nuclei. Our simulations on average over-predict the mass of stars bound in the central galaxies by a factor of 2 when compared to halo-occupation-distribution models. The feedback mechanism used here is not strong enough to produce the galactic outflows that are usually observed in highly star-forming galaxies and therefore favors the production of old spheroidal systems. The above mentioned feedback processes are believed to be important to sufficiently suppress star formation in high and low mass systems. Recent simulations (Governato et al. 2010; Brook et al. 2011) have shown that high spatial resolution is needed in order to be able to resolve the clumpy structure of the ISM and to produce galactic outflows - which are deemed to be important to suppress the star formation efficiency and to explain the enrichment of the inter galactic medium (Oppenheimer & Davé 2006; Oppenheimer et al. 2010b). Only at this high resolution winds with high mass loading factors form self-consistently as a result of supernovae feedback. This high spatial accuracy is becoming feasible in simulations of massive galaxies and we are currently implementing a new star formation model that will not rely on the multi-phase subgrid model presented in section 4.5. A high spatial and mass resolution is needed to resolve the multi-phase ISM in the simulations. The large amount of the momentum released to the ISM from massive stars and SNe is added to the momentum of neighboring gas particles instead of just increasing the internal energy of the gas particles. First tests have shown that this model is able to produce galactic outflows where the mass loading is several times the star formation rate in the galaxy. However this method has yet to be implemented in the cosmological simulations.

We performed some of our simulations with the ad-hoc wind model presented in (Oppenheimer & Davé 2006). These simulations follow the enrichment with metals and we show one example of the metal distribution in a galaxy at the present day in Fig. 8.1. Like in this representative example we often find metal gradients in the galaxies where the highest level of metal enrichment is reached in the centers of the galaxies. This is where the youngest stars are created out of gas that is pre-enriched by older generations of stars. We intend to make predictions for metal and age gradients for direct comparison with galaxy redshift surveys (Förster Schreiber et al. 2009; Grogin et al. 2011).

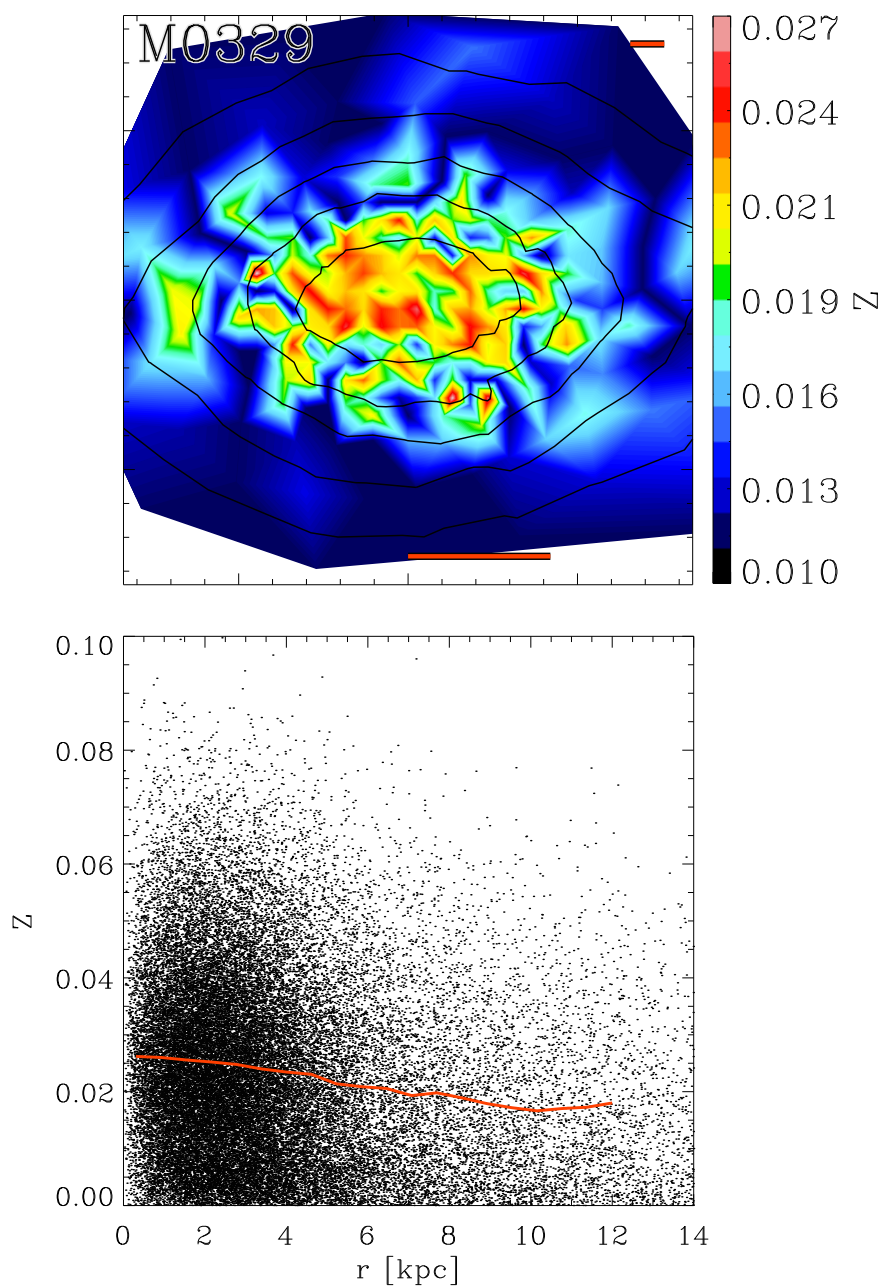


**Figure 8.1:** This figure shows in the top panel the total mass fraction of metals in stars for the galaxy M0329 at the present day. The red bar at the bottom indicates the half mass radius, the one on top represents 1 kpc. The lower panel shows the stellar metal distribution as function of distance to the galaxy center. The red line represents the average value of the binned metallicities. The stars formed in the center show the highest level of enrichment.

# Appendix A

## Kinematic maps

Here we present the stellar kinematic maps of all the galaxies discussed in chapter 7 for their edge-on projection. The two-dimensional maps show from left to right the stellar velocities, velocity dispersions as well as the amplitudes of the higher order Gauss-Hermite polynomials  $h_3$  and  $h_4$  (see Section 7.2). The halo ID, the  $\lambda_R$ -parameter (see Section 7.3), the ellipticity at  $r_{1/2}$  and the physical scale of 1 kpc (black bar) are given in the leftmost panels.

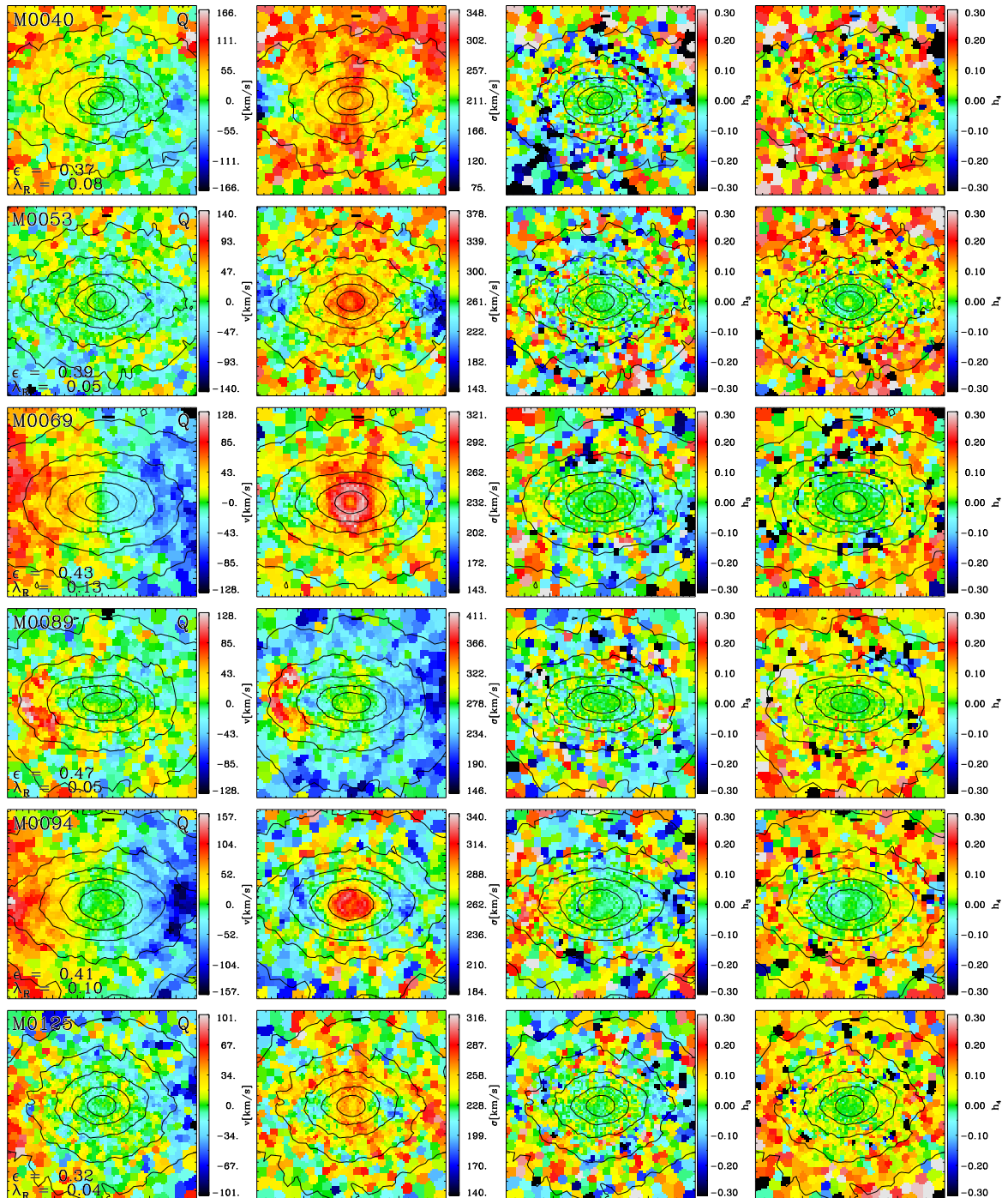


Figure A.1: Kinematic maps: M0040 - M0125

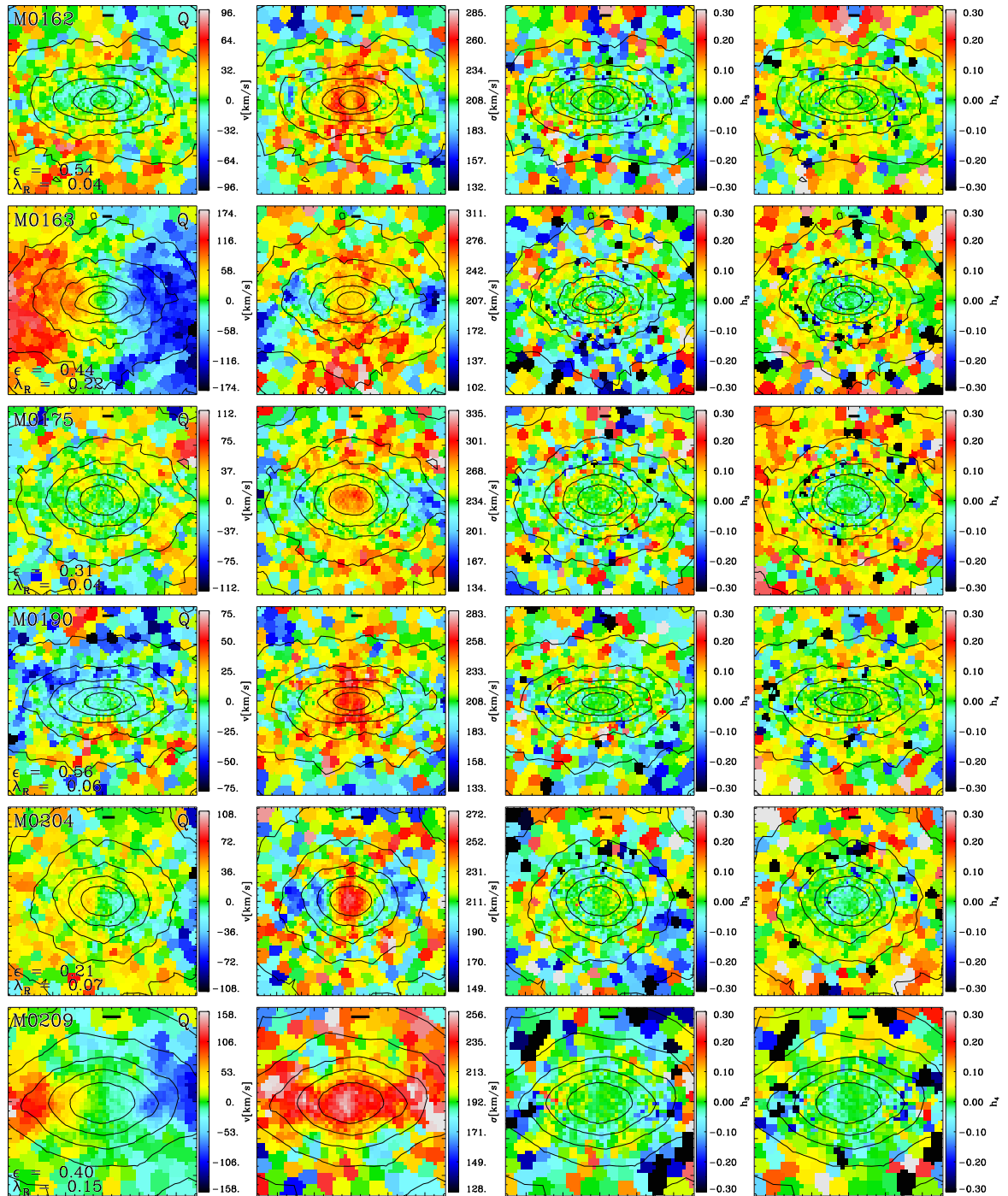


Figure A.2: Kinematic maps: M0162 - M0209

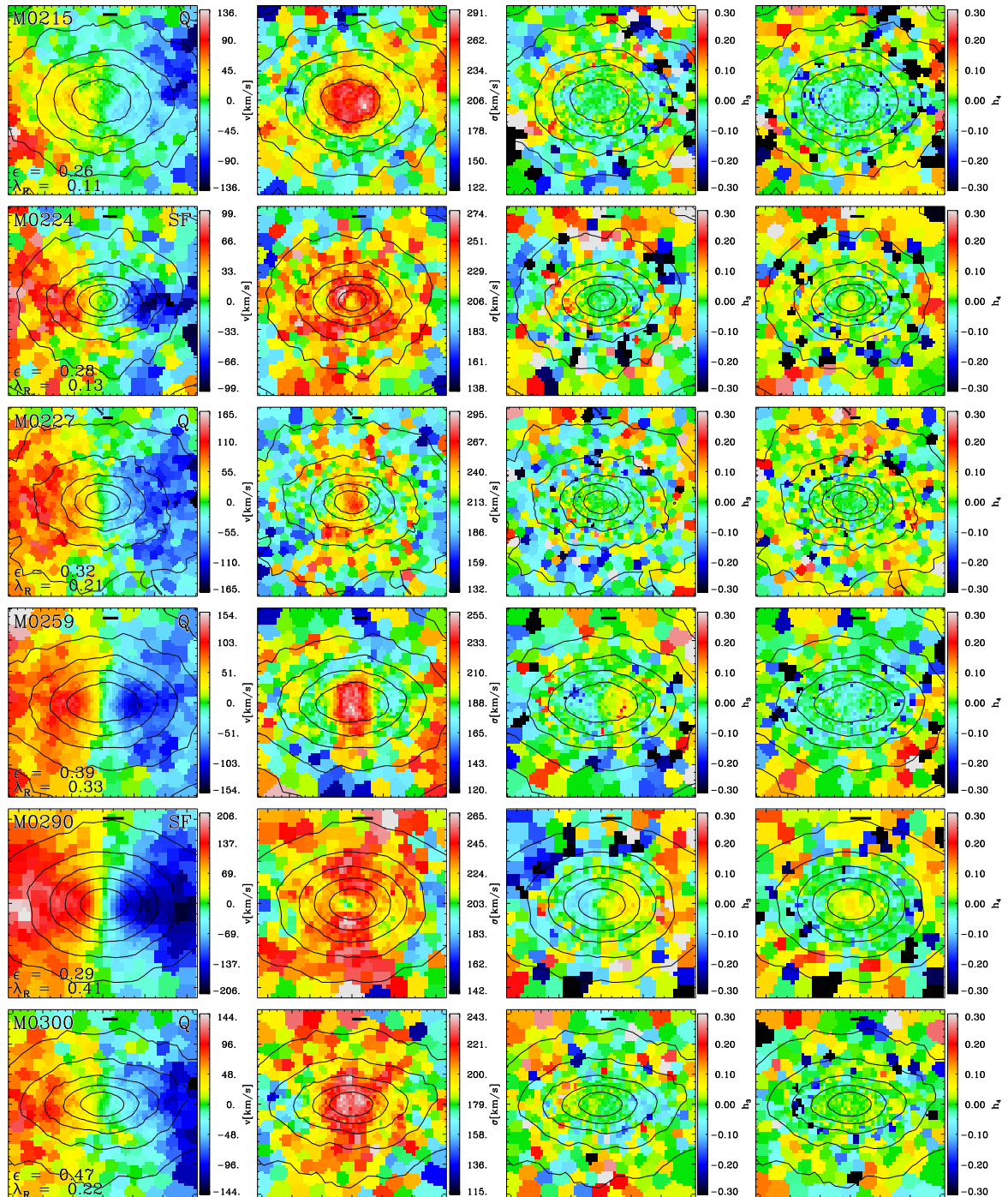


Figure A.3: Kinematic maps: M0215 - M0300

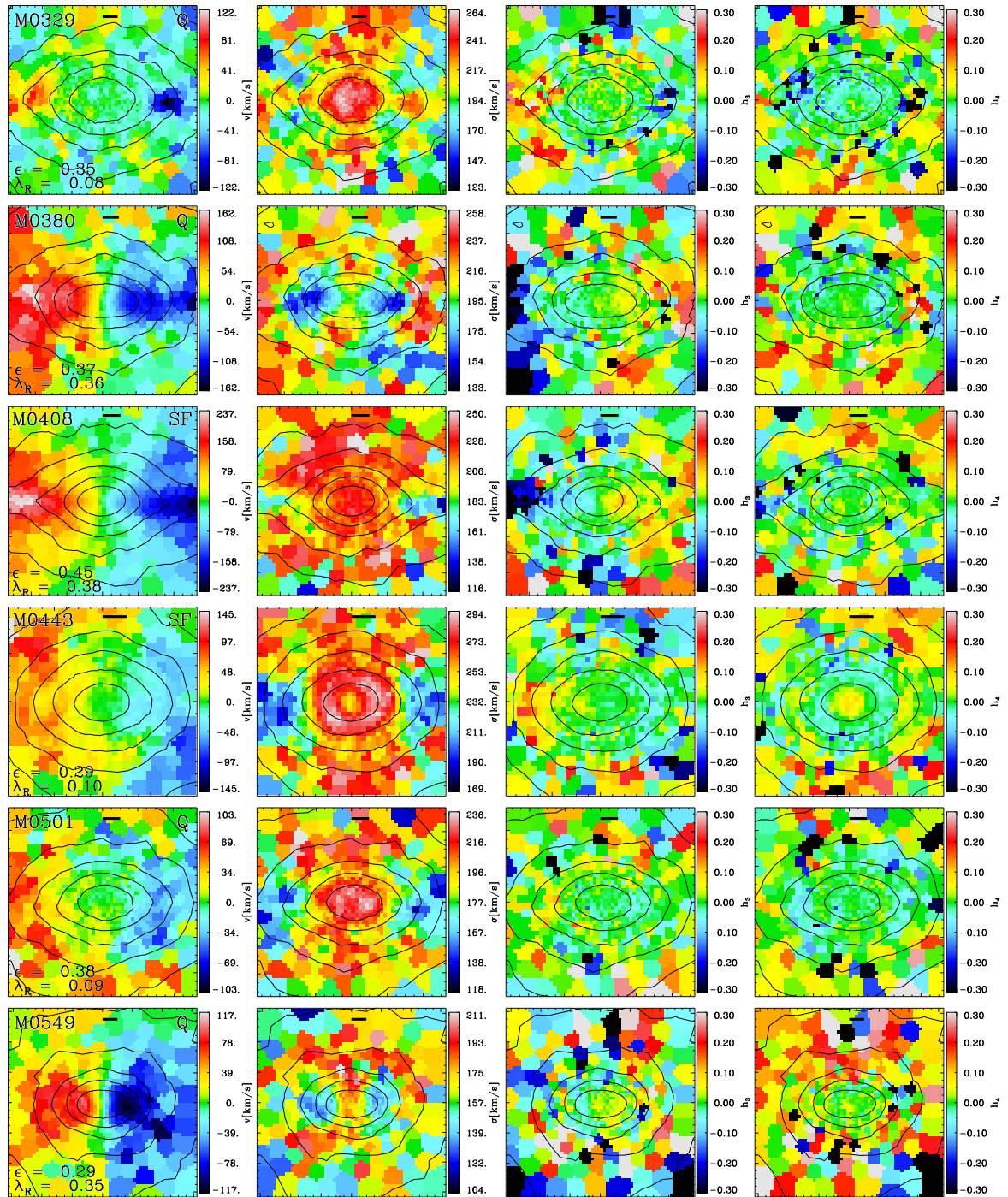


Figure A.4: Kinematic maps: M0329 - M0549

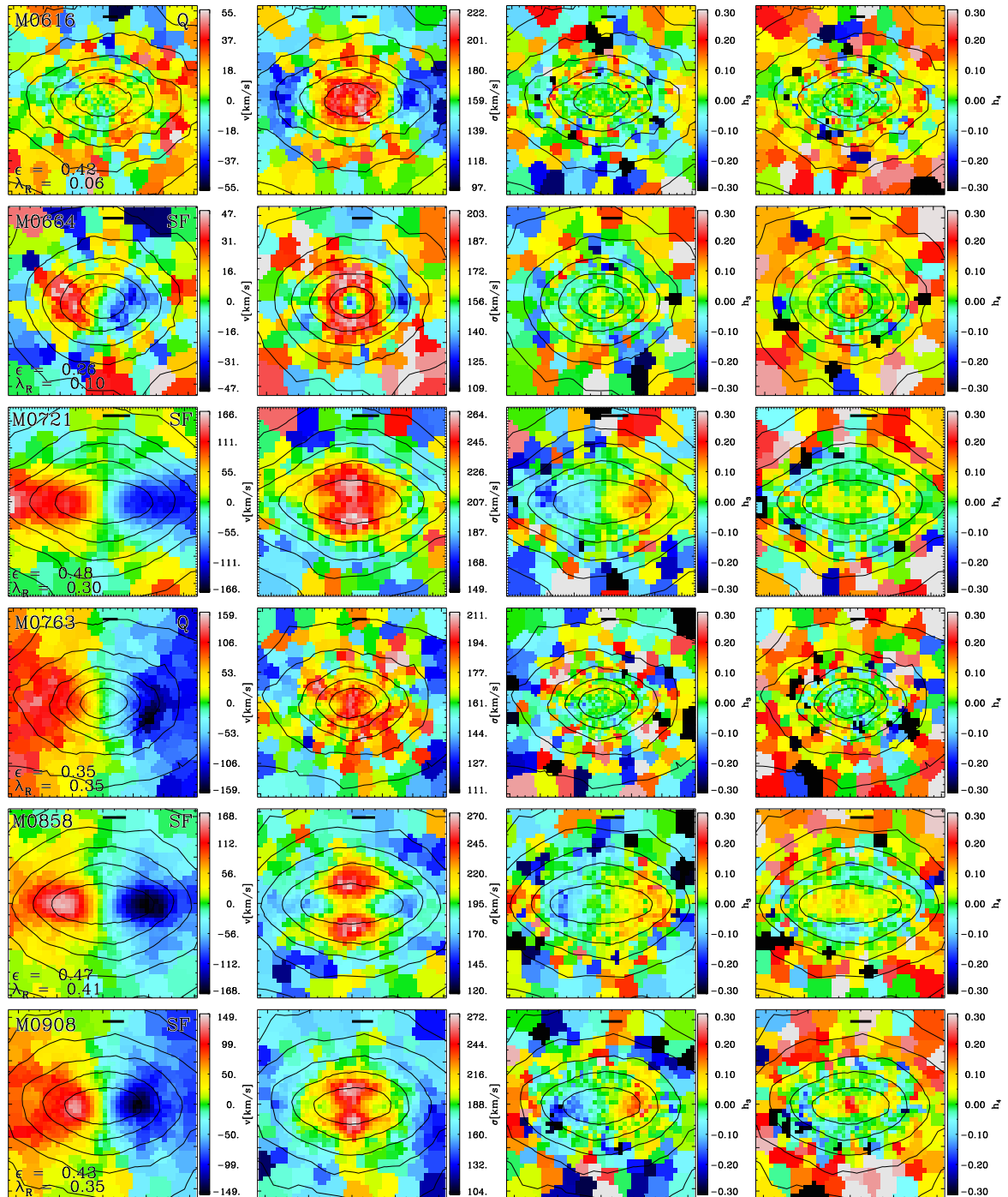


Figure A.5: Kinematic maps: M0616 - M0908

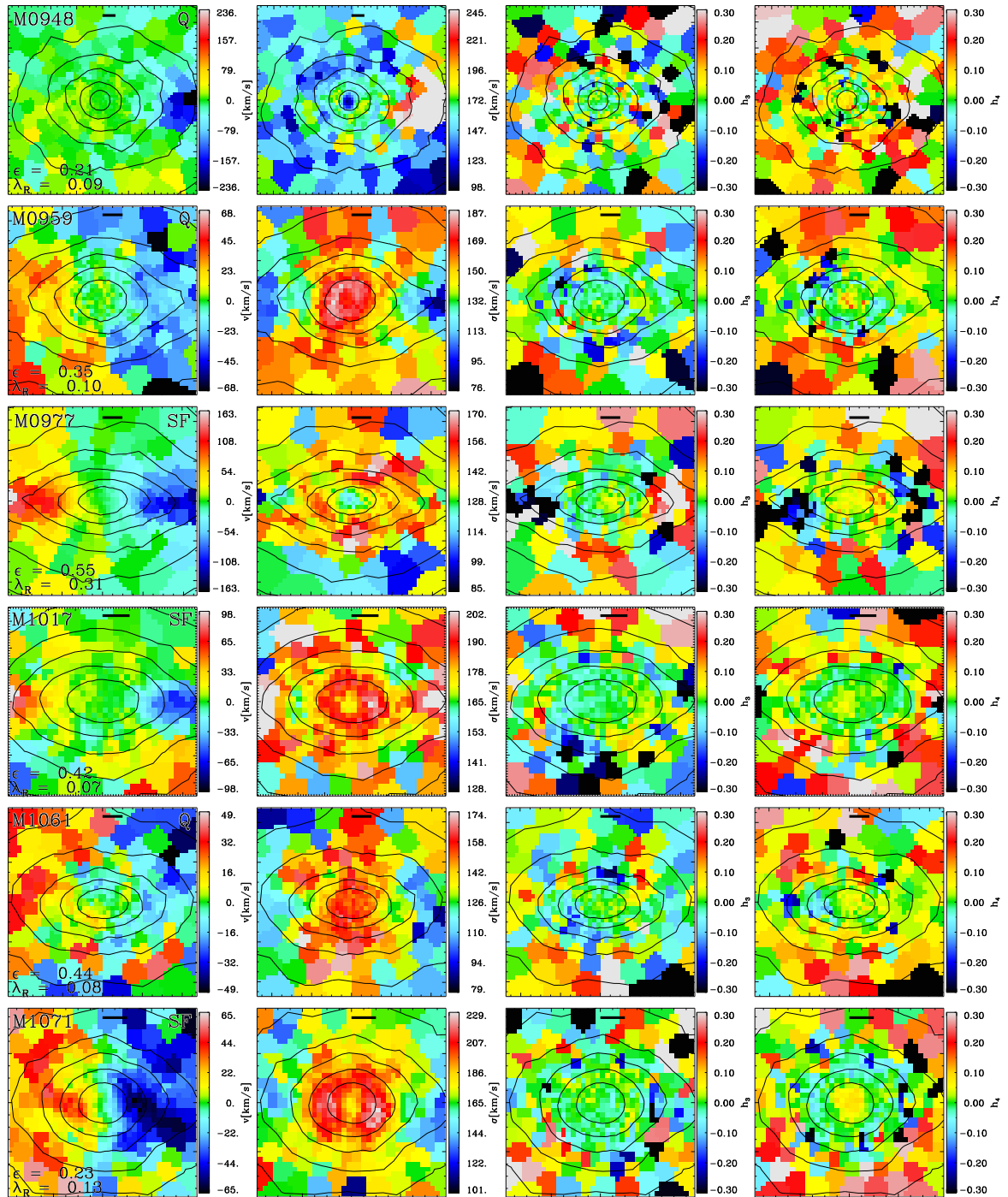


Figure A.6: Kinematic maps: M0948 - M1071

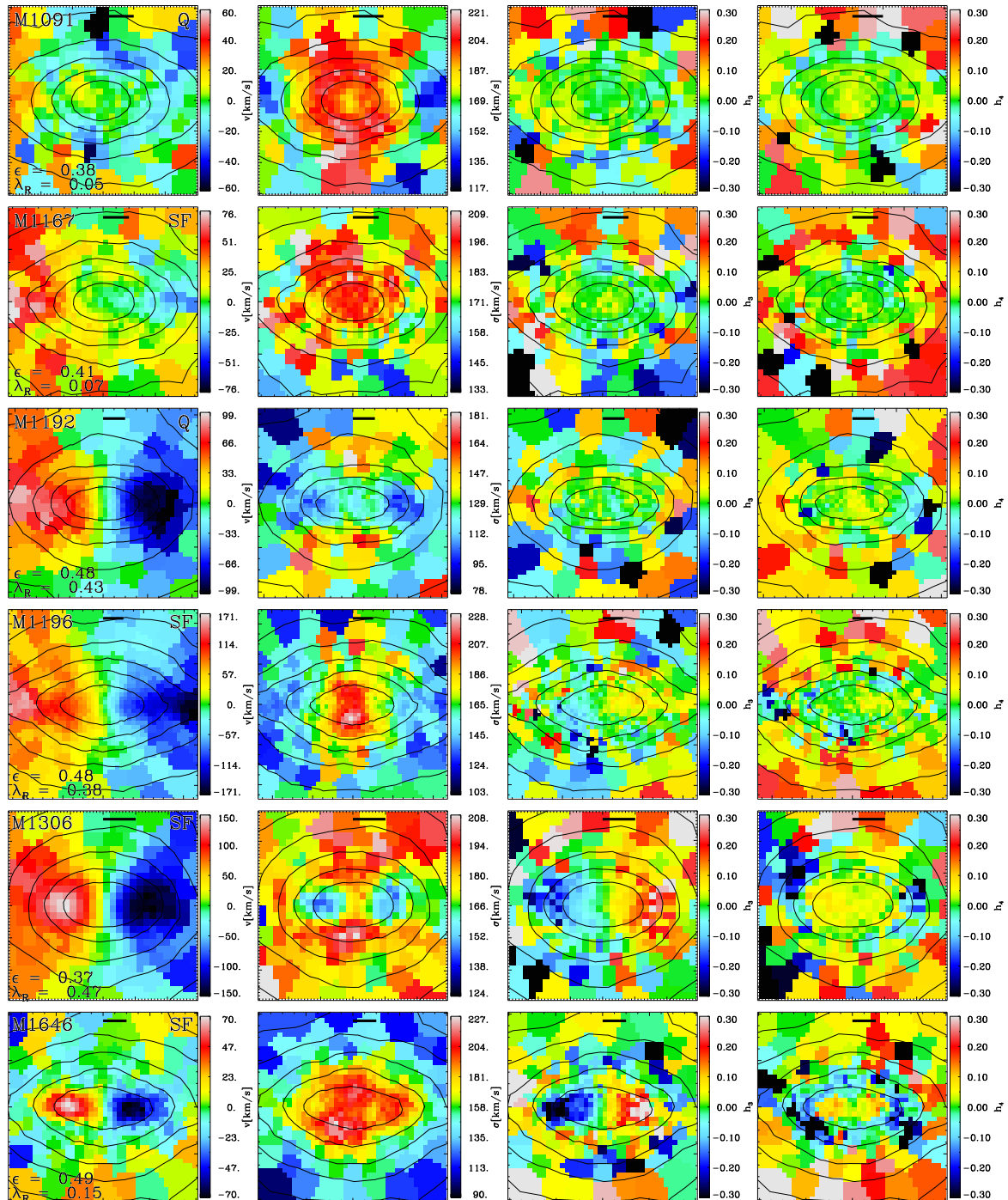


Figure A.7: Kinematic maps: M1091 - M1646

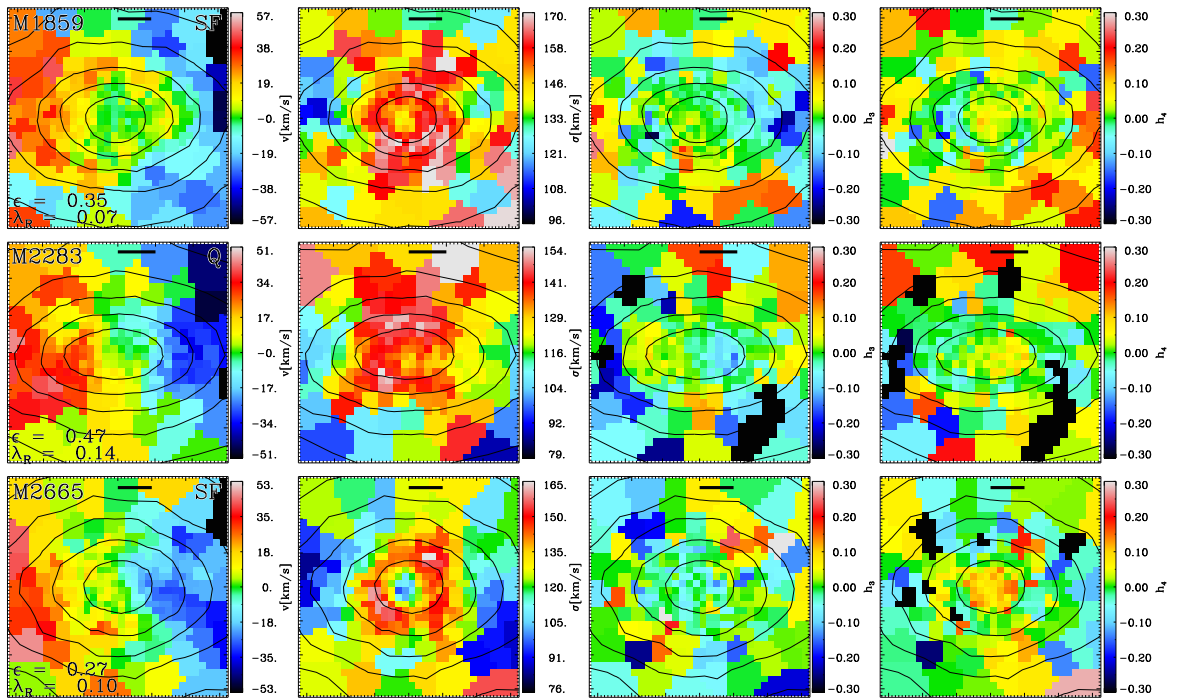


Figure A.8: Kinematic maps: M1859 - M2665



# Bibliography

AARSETH, S. J.: 1963. Dynamical evolution of clusters of galaxies, I. MNRAS, **126**, 223.

ABADI, M. G., NAVARRO, J. F., FARDAL, M., ET AL. : 2010. Galaxy-induced transformation of dark matter haloes. MNRAS, arxiv:n 847-+.

ABADI, M. G., NAVARRO, J. F., STEINMETZ, M., ET AL. : 2003. Simulations of Galaxy Formation in a  $\Lambda$  Cold Dark Matter Universe. II. The Fine Structure of Simulated Galactic Disks. ApJ, **597**, 21–34.

AGERTZ, O., TEYSSIER, R., MOORE, B.: 2010. The formation of disk galaxies in a LCDM universe. ArXiv e-prints.

AGERTZ, O., TEYSSIER, R., MOORE, B.: 2011. The formation of disc galaxies in a  $\Lambda$ CDM universe. MNRAS, **410**, 1391–1408.

ANGULO, R. WHITE, S.: 2011. The millennium-xxl project: Simulating the galaxy population in dark energy universes, [http://www.mpa-garching.mpg.de/mpa/research/current\\_research/h12011-9/h12011-9-](http://www.mpa-garching.mpg.de/mpa/research/current_research/h12011-9/h12011-9-)

ARNOLD, J. A., ROMANOWSKY, A. J., BRODIE, J. P., ET AL. : 2011. The Fossil Record of Two-phase Galaxy Assembly: Kinematics and Metallicities in the Nearest S0 Galaxy. ApJ, **736**, L26+.

ATHANASSOULA, E., FADY, E., LAMBERT, J. C., ET AL. : 2000. Optimal softening for force calculations in collisionless N-body simulations. MNRAS, **314**, 475–488.

AUGER, M. W., TREU, T., GAVAZZI, R., ET AL. : 2010. Dark Matter Contraction and the Stellar Content of Massive Early-type Galaxies: Disfavoring "Light" Initial Mass Functions. ArXiv e-prints.

AVILA-REESE, V., COLÍN, P., GONZÁLEZ-SAMANIEGO, A., ET AL. : 2011. The Specific Star Formation Rate and Stellar Mass Fraction of Low-mass Central Galaxies in Cosmological Simulations. ApJ, **736**, 134.

- BACON, R., COPIN, Y., MONNET, G., ET AL. : 2001. The SAURON project - I. The panoramic integral-field spectrograph. MNRAS, **326**, 23–35.
- BALSARA, D. S.: 1995. von Neumann stability analysis of smooth particle hydrodynamics—suggestions for optimal algorithms. Journal of Computational Physics, **121**, 357–372.
- BARNES, J. HUT, P.: 1986. A Hierarchical O(NlogN) Force-Calculation Algorithm. Nature, **324**, 446–449.
- BAUGH, C. M., COLE, S., FRENK, C. S.: 1996. Evolution of the Hubble sequence in hierarchical models for galaxy formation. MNRAS, **283**, 1361–1378.
- BEHROOZI, P. S., CONROY, C., WECHSLER, R. H.: 2010. A Comprehensive Analysis of Uncertainties Affecting the Stellar Mass-Halo Mass Relation for  $0 < z < 4$ . ApJ, **717**, 379–403.
- BELL, E. F., NAAB, T., MCINTOSH, D. H., ET AL. : 2006. Dry Mergers in GEMS: The Dynamical Evolution of Massive Early-Type Galaxies. ApJ, **640**, 241–251.
- BENDER, R., BURSTEIN, D., FABER, S. M.: 1992. Dynamically hot galaxies. I - Structural properties. ApJ, **399**, 462–477.
- BENDER, R., SAGLIA, R. P., GERHARD, O. E.: 1994. Line-of-Sight Velocity Distributions of Elliptical Galaxies. MNRAS, **269**, 785.
- BENDO, G. J. BARNES, J. E.: 2000. The line-of-sight velocity distributions of simulated merger remnants. MNRAS, **316**, 315–325.
- BENSON, A. J.: 2005. Orbital parameters of infalling dark matter substructures. MNRAS, **358**, 551–562.
- BERGER, M. J. OLIGER, J.: 1984. Adaptive Mesh Refinement for Hyperbolic Partial Differential Equations. Journal of Computational Physics, **53**, 484.
- BERTSCHINGER, E.: 1995. COSMICS: Cosmological Initial Conditions and Microwave Anisotropy Codes. ArXiv Astrophysics e-prints.
- BERTSCHINGER, E.: 2001. Multiscale Gaussian Random Fields and Their Application to Cosmological Simulations. ApJS, **137**, 1–20.
- BEZANSON, R., VAN DOKKUM, P. G., TAL, T., ET AL. : 2009. The Relation Between Compact, Quiescent High-redshift Galaxies and Massive Nearby Elliptical Galaxies: Evidence for Hierarchical, Inside-Out Growth. ApJ, **697**, 1290–1298.
- BINNEY, J. TREMAINE, S.: 1987. Galactic dynamics.

- BLUCK, A. F. L., CONSELICE, C. J., BOUWENS, R. J., ET AL. : 2009. A surprisingly high pair fraction for extremely massive galaxies at  $z \sim 3$  in the GOODS NICMOS survey. MNRAS, **394**, L51–L55.
- BLUMENTHAL, G. R., FABER, S. M., FLORES, R., ET AL. : 1986. Contraction of dark matter galactic halos due to baryonic infall. ApJ, **301**, 27–34.
- BOIS, M., BOURNAUD, F., EMSELLEM, E., ET AL. : 2010. Formation of slowly rotating early-type galaxies via major mergers: a resolution study. MNRAS, **406**, 2405–2420.
- BOIS, M., EMSELLEM, E., BOURNAUD, F., ET AL. : 2011. The ATLAS<sup>3D</sup> project - VI. Simulations of binary galaxy mergers and the link with fast rotators, slow rotators and kinematically distinct cores. MNRAS, **416**, 1654–1679.
- BOOTH, C. M. SCHAYE, J.: 2009. Cosmological simulations of the growth of super-massive black holes and feedback from active galactic nuclei: method and tests. MNRAS, **398**, 53–74.
- BOURNAUD, F., CHAPON, D., TEYSSIER, R., ET AL. : 2011. Hydrodynamics of High-redshift Galaxy Collisions: From Gas-rich Disks to Dispersion-dominated Mergers and Compact Spheroids. ApJ, **730**, 4–+.
- BOYLAN-KOLCHIN, M., MA, C.-P., QUATAERT, E.: 2005. Dissipationless mergers of elliptical galaxies and the evolution of the fundamental plane. MNRAS, **362**, 184–196.
- BOYLAN-KOLCHIN, M., MA, C.-P., QUATAERT, E.: 2006. Red mergers and the assembly of massive elliptical galaxies: the fundamental plane and its projections. MNRAS, **369**, 1081–1089.
- BROOK, C. B., GOVERNATO, F., ROŠKAR, R., ET AL. : 2011. Hierarchical formation of bulgeless galaxies: why outflows have low angular momentum. MNRAS, **415**, 1051–1060.
- BROWN, M. J. I., DEY, A., JANNUZI, B. T., ET AL. : 2007. The Evolving Luminosity Function of Red Galaxies. ApJ, **654**, 858–877.
- BUITRAGO, F., TRUJILLO, I., CONSELICE, C. J., ET AL. : 2008. Size Evolution of the Most Massive Galaxies at  $1.7 < z < 3$  from GOODS NICMOS Survey Imaging. ApJ, **687**, L61–L64.
- BULLOCK, J. S., DEKEL, A., KOLATT, T. S., ET AL. : 2001. A Universal Angular Momentum Profile for Galactic Halos. ApJ, **555**, 240–257.
- CAPPELLARI, M. COPIN, Y.: 2003. Adaptive spatial binning of integral-field spectroscopic data using Voronoi tessellations. MNRAS, **342**, 345–354.

- CAPPELLARI, M., DI SEREGO ALIGHIERI, S., CIMATTI, A., ET AL. : 2009. Dynamical Masses of Early-Type Galaxies at  $z \sim 2$ : Are they Truly Superdense? ApJ, **704**, L34–L39.
- CAPPELLARI, M., EMSELLEM, E., KRAJNOVIĆ, D., ET AL. : 2011a. The ATLAS<sup>3D</sup> project - I. A volume-limited sample of 260 nearby early-type galaxies: science goals and selection criteria. MNRAS, **413**, 813–836.
- CAPPELLARI, M., EMSELLEM, E., KRAJNOVIĆ, D., ET AL. : 2011b. The ATLAS<sup>3D</sup> project - VII. A new look at the morphology of nearby galaxies: the kinematic morphology-density relation. MNRAS, **416**, 1680–1696.
- CARRASCO, E. R., CONSELICE, C. J., TRUJILLO, I.: 2010. Gemini K-band NIRI Adaptive Optics Observations of massive galaxies at  $1 < z < 2$ . MNRAS, **405**, 2253–2259.
- CASSATA, P., GIAVALISCO, M., GUO, Y., ET AL. : 2011. The relative abundance of compact and normal massive early-type galaxies and its evolution from redshift  $z \sim 2$  to the present. ArXiv e-prints, arxiv: 1106.4308.
- CEN, R. CHISARI, N. E.: 2010. Star Formation Feedback and Metal Enrichment History Of The Intergalactic Medium. ArXiv e-prints.
- CEN, R. CHISARI, N. E.: 2011. Star Formation Feedback and Metal-enrichment History of the Intergalactic Medium. ApJ, **731**, 11.
- CEN, R. OSTRIKER, J. P.: 1999. Where Are the Baryons? ApJ, **514**, 1–6.
- CENARRO, A. J. TRUJILLO, I.: 2009. Mild Velocity Dispersion Evolution of Spheroid-Like Massive Galaxies Since  $z \sim 2$ . ApJ, **696**, L43–L47.
- CIMATTI, A., CASSATA, P., POZZETTI, L., ET AL. : 2008. GMASS ultradeep spectroscopy of galaxies at  $z \sim 2$ . II. Superdense passive galaxies: how did they form and evolve? A&A, **482**, 21–42.
- CIOTTI, L. OSTRIKER, J. P.: 2007. Radiative Feedback from Massive Black Holes in Elliptical Galaxies: AGN Flaring and Central Starburst Fueled by Recycled Gas. ApJ, **665**, 1038–1056.
- COCCATO, L., GERHARD, O., ARNABOLDI, M.: 2010. Distinct core and halo stellar populations and the formation history of the bright Coma cluster early-type galaxy NGC 4889. MNRAS, **407**, L26–L30.
- COCCATO, L., GERHARD, O., ARNABOLDI, M., ET AL. : 2011. Stellar population and the origin of intra-cluster stars around brightest cluster galaxies: the case of NGC 3311. ArXiv e-prints, arxiv: 1108.3834.

- COLE, S., LACEY, C. G., BAUGH, C. M., ET AL. : 2000. Hierarchical galaxy formation. MNRAS, **319**, 168–204.
- COLLESS, M., DALTON, G., MADDOX, S., ET AL. : 2001. The 2dF Galaxy Redshift Survey: spectra and redshifts. MNRAS, **328**, 1039–1063.
- CONROY, C. WECHSLER, R. H.: 2009. Connecting Galaxies, Halos, and Star Formation Rates Across Cosmic Time. ApJ, **696**, 620–635.
- COURANT, R., FRIEDRICHS, K., LEWY, H.: 1928. Über die partiellen Differenzengleichungen der mathematischen Physik. Mathematische Annalen, **100**, 32–74.
- COVINGTON, M. D., PRIMACK, J. R., PORTER, L. A., ET AL. : 2011. The Role of Dissipation in the Scaling Relations of Cosmological Merger Remnants. ArXiv e-prints.
- CROTON, D. J., SPRINGEL, V., WHITE, S. D. M., ET AL. : 2006. The many lives of active galactic nuclei: cooling flows, black holes and the luminosities and colours of galaxies. MNRAS, **365**, 11–28.
- DADDI, E., RENZINI, A., PIRZKAL, N., ET AL. : 2005. Passively Evolving Early-Type Galaxies at  $1.4 < z < 2.5$  in the Hubble Ultra Deep Field. ApJ, **626**, 680–697.
- DAMJANOV, I., ABRAHAM, R. G., GLAZEBROOK, K., ET AL. : 2011. Red Nuggets at High Redshift: Structural Evolution of Quiescent Galaxies Over 10 Gyr of Cosmic History. ArXiv e-prints, arxiv: 1108.0656.
- DAMJANOV, I., MCCARTHY, P. J., ABRAHAM, R. G., ET AL. : 2009. Red Nuggets at  $z \sim 1.5$ : Compact Passive Galaxies and the Formation of the Kormendy Relation. ApJ, **695**, 101–115.
- DAVÉ, R., HERNQUIST, L., KATZ, N., ET AL. : 1999. The Low-Redshift LYalpha Forest in Cold Dark Matter Cosmologies. ApJ, **511**, 521–545.
- DAVIS, T. A., BUREAU, M., YOUNG, L. M., ET AL. : 2011. The ATLAS<sup>3D</sup> project - V. The CO Tully-Fisher relation of early-type galaxies. MNRAS, **414**, 968–984.
- DE LUCIA, G. BLAIZOT, J.: 2007. The hierarchical formation of the brightest cluster galaxies. MNRAS, **375**, 2–14.
- DE LUCIA, G., SPRINGEL, V., WHITE, S. D. M., ET AL. : 2006. The formation history of elliptical galaxies. MNRAS, **366**, 499–509.
- DE ZEEUW, P. T., BUREAU, M., EMMELLEM, E., ET AL. : 2002. The SAURON project - II. Sample and early results. MNRAS, **329**, 513–530.

- DEBATTISTA, V. P., MOORE, B., QUINN, T., ET AL. : 2008. The Causes of Halo Shape Changes Induced by Cooling Baryons: Disks versus Substructures. ApJ, **681**, 1076–1088.
- DEBUHR, J., QUATAERT, E., MA, C., ET AL. : 2010. Self-regulated black hole growth via momentum deposition in galaxy merger simulations. MNRAS, **406**, L55–L59.
- DEHNEN, W.: 2000. A Very Fast and Momentum-conserving Tree Code. ApJ, **536**, L39–L42.
- DEHNEN, W.: 2001. Towards optimal softening in three-dimensional N-body codes - I. Minimizing the force error. MNRAS, **324**, 273–291.
- DEKEL, A. BIRNBOIM, Y.: 2006. Galaxy bimodality due to cold flows and shock heating. MNRAS, **368**, 2–20.
- DEKEL, A., BIRNBOIM, Y., ENGEL, G., ET AL. : 2009a. Cold streams in early massive hot haloes as the main mode of galaxy formation. Nature, **457**, 451–454.
- DEKEL, A., SARI, R., CEVERINO, D.: 2009b. Formation of Massive Galaxies at High Redshift: Cold Streams, Clumpy Disks, and Compact Spheroids. ApJ, **703**, 785–801.
- DEKEL, A. SILK, J.: 1986. The origin of dwarf galaxies, cold dark matter, and biased galaxy formation. ApJ, **303**, 39–55.
- DI MATTEO, P., JOG, C. J., LEHNERT, M. D., ET AL. : 2009. Generation of rotationally dominated galaxies by mergers of pressure-supported progenitors. A&A, **501**, L9–L13.
- DI MATTEO, T., COLBERG, J., SPRINGEL, V., ET AL. : 2008. Direct Cosmological Simulations of the Growth of Black Holes and Galaxies. ApJ, **676**, 33–53.
- DI MATTEO, T., SPRINGEL, V., HERNQUIST, L.: 2005. Energy input from quasars regulates the growth and activity of black holes and their host galaxies. Nature, **433**, 604–607.
- DI SEREGO ALIGHIERI, S., VERNET, J., CIMATTI, A., ET AL. : 2005. The evolution of early-type galaxies at  $z \sim 1$  from the K20 survey. A&A, **442**, 125–136.
- DOLAG, K., BORGANI, S., MURANTE, G., ET AL. : 2009. Substructures in hydrodynamical cluster simulations. MNRAS, **399**, 497–514.
- DUBINSKI, J.: 1994. The effect of dissipation on the shapes of dark halos. ApJ, **431**, 617–624.

- DUC, P.-A., CUILLANDRE, J.-C., SERRA, P., ET AL. : 2011. The ATLAS<sup>3D</sup> project - IX. The merger origin of a fast- and a slow-rotating early-type galaxy revealed with deep optical imaging: first results. MNRAS, **417**, 863–881.
- EFSTATHIOU, G., DAVIS, M., WHITE, S. D. M., ET AL. : 1985. Numerical techniques for large cosmological N-body simulations. ApJS, **57**, 241–260.
- EGGEN, O. J., LYNDEN-BELL, D., SANDAGE, A. R.: 1962. Evidence from the motions of old stars that the Galaxy collapsed. ApJ, **136**, 748.
- EMSELLEM, E., CAPPELLARI, M., KRAJNOVIĆ, D., ET AL. : 2011. The ATLAS<sup>3D</sup> project - III. A census of the stellar angular momentum within the effective radius of early-type galaxies: unveiling the distribution of fast and slow rotators. MNRAS, **414**, 888–912.
- EMSELLEM, E., CAPPELLARI, M., KRAJNOVIĆ, D., ET AL. : 2007. The SAURON project - IX. A kinematic classification for early-type galaxies. MNRAS, **379**, 401–417.
- EMSELLEM, E., CAPPELLARI, M., PELETIER, R. F., ET AL. : 2004. The SAURON project - III. Integral-field absorption-line kinematics of 48 elliptical and lenticular galaxies. MNRAS, **352**, 721–743.
- FABER, S. M., WILLMER, C. N. A., WOLF, C., ET AL. : 2007. Galaxy Luminosity Functions to  $z \sim 1$  from DEEP2 and COMBO-17: Implications for Red Galaxy Formation. ApJ, **665**, 265–294.
- FAN, L., LAPI, A., BRESSAN, A., ET AL. : 2010. Cosmic Evolution of Size and Velocity Dispersion for Early-type Galaxies. ApJ, **718**, 1460–1475.
- FAN, L., LAPI, A., DE ZOTTI, G., ET AL. : 2008. The Dramatic Size Evolution of Elliptical Galaxies and the Quasar Feedback. ApJ, **689**, L101–L104.
- FAROUKI, R. T. SHAPIRO, S. L.: 1982. Simulations of merging disk galaxies. ApJ, **259**, 103–115.
- FELDMANN, R., CAROLLO, C. M., MAYER, L.: 2011. The Hubble Sequence in Groups: The Birth of the Early-type Galaxies. ApJ, **736**, 88.
- FELDMANN, R., CAROLLO, C. M., MAYER, L., ET AL. : 2010. The Evolution of Central Group Galaxies in Hydrodynamical Simulations. ApJ, **709**, 218–240.
- FISHER, D.: 1997. Kinematic Profiles of SO Galaxies. AJ, **113**, 950.
- FORBES, D. A., SPITLER, L. R., STRADER, J., ET AL. : 2011. Evidence for two phases of galaxy formation from radial trends in the globular cluster system of NGC 1407. MNRAS, **413**, 2943–2949.

- FÖRSTER SCHREIBER, N. M., GENZEL, R., BOUCHÉ, N., ET AL. : 2009. The SINS Survey: SINFONI Integral Field Spectroscopy of  $z \sim 2$  Star-forming Galaxies. ApJ, **706**, 1364–1428.
- FÖRSTER SCHREIBER, N. M., GENZEL, R., LEHNERT, M. D., ET AL. : 2006. SINFONI Integral Field Spectroscopy of  $z \sim 2$  UV-selected Galaxies: Rotation Curves and Dynamical Evolution. ApJ, **645**, 1062–1075.
- FRANX, M., VAN DOKKUM, P. G., SCHREIBER, N. M. F., ET AL. : 2008. Structure and Star Formation in Galaxies out to  $z = 3$ : Evidence for Surface Density Dependent Evolution and Upsizing. ApJ, **688**, 770–788.
- GENEL, S., NAAB, T., GENZEL, R., ET AL. : 2010. Short-lived star-forming giant clumps in cosmological simulations of  $z \sim 2$  disks. ArXiv e-prints.
- GENZEL, R., TACCONI, L. J., EISENHAUER, F., ET AL. : 2006. The rapid formation of a large rotating disk galaxy three billion years after the Big Bang. Nature, **442**, 786–789.
- GERHARD, O. E.: 1981. N-body simulations of disc-halo galaxies - Isolated systems, tidal interactions and merging. MNRAS, **197**, 179–208.
- GERHARD, O. E.: 1993. Line-of-sight velocity profiles in spherical galaxies: breaking the degeneracy between anisotropy and mass. MNRAS, **265**, 213.
- GINGOLD, R. A. MONAGHAN, J. J.: 1977. Smoothed particle hydrodynamics - Theory and application to non-spherical stars. MNRAS, **181**, 375–389.
- GNEDIN, O. Y., KRAVTSOV, A. V., KLYPIN, A. A., ET AL. : 2004. Response of Dark Matter Halos to Condensation of Baryons: Cosmological Simulations and Improved Adiabatic Contraction Model. ApJ, **616**, 16–26.
- GOVERNATO, F., BROOK, C., MAYER, L., ET AL. : 2010. Bulgeless dwarf galaxies and dark matter cores from supernova-driven outflows. Nature, **463**, 203–206.
- GOVERNATO, F., BROOK, C. B., BROOKS, A. M., ET AL. : 2009. Forming a large disc galaxy from a  $z < 1$  major merger. MNRAS, **398**, 312–320.
- GOVERNATO, F., WILLMAN, B., MAYER, L., ET AL. : 2007. Forming disc galaxies in  $\Lambda$ CDM simulations. MNRAS, **374**, 1479–1494.
- GROGIN, N. A., KOCEVSKI, D. D., FABER, S. M., ET AL. : 2011. CANDELS: The Cosmic Assembly Near-infrared Deep Extragalactic Legacy Survey. ApJS, **197**, 35.
- GROSSI, M. SPRINGEL, V.: 2009. The impact of early dark energy on non-linear structure formation. MNRAS, **394**, 1559–1574.

- GUEDES, J., CALLEGARI, S., MADAU, P., ET AL. : 2011. Forming Realistic Late-type Spirals in a  $\Lambda$ CDM Universe: The Eris Simulation. ApJ, **742**, 76.
- GUO, Q., WHITE, S., BOYLAN-KOLCHIN, M., ET AL. : 2010a. From dwarf spheroidals to cDs: Simulating the galaxy population in a LCDM cosmology. ArXiv e-prints.
- GUO, Q., WHITE, S., BOYLAN-KOLCHIN, M., ET AL. : 2011. From dwarf spheroidals to cD galaxies: simulating the galaxy population in a  $\Lambda$ CDM cosmology. MNRAS, **413**, 101–131.
- GUO, Q., WHITE, S., LI, C., ET AL. : 2010b. How do galaxies populate dark matter haloes? MNRAS, **404**, 1111–1120.
- GUO, Q. WHITE, S. D. M.: 2008. Galaxy growth in the concordance  $\Lambda$ CDM cosmology. MNRAS, **384**, 2–10.
- GUO, Y., MCINTOSH, D. H., MO, H. J., ET AL. : 2009. Structural properties of central galaxies in groups and clusters. MNRAS, **398**, 1129–1149.
- GUTH, A. H.: 1981. Inflationary universe: A possible solution to the horizon and flatness problems. Phys. Rev. D, **23**, 347–356.
- HAARDT, F. MADAU, P.: 1996. Radiative Transfer in a Clumpy Universe. II. The Ultraviolet Extragalactic Background. ApJ, **461**, 20.
- HAMBRICK, D. C., OSTRIKER, J. P., JOHANSSON, P. H., ET AL. : 2011. The effects of X-ray and UV background radiation on the low-mass slope of the galaxy mass function. MNRAS, **413**, 2421–2428.
- HIRSCHMANN, M., NAAB, T., SOMERVILLE, R., ET AL. : 2011. Galaxy formation in semi-analytic models and cosmological hydrodynamic zoom simulations. ArXiv e-prints, arxiv: 1104.1626.
- HOFFMAN, L., COX, T. J., DUTTA, S., ET AL. : 2009. The Imprint of Dissipation on the Shapes of Merger Remnant LOSVDs. ApJ, **705**, 920–925.
- HOFFMAN, L., COX, T. J., DUTTA, S., ET AL. : 2010. Orbital Structure of Merger Remnants. I. Effect of Gas Fraction in Pure Disk Mergers. ApJ, **723**, 818–844.
- HOPKINS, P. F., BUNDY, K., CROTON, D., ET AL. : 2009a. Mergers and Bulge Formation in Lambda-CDM: Which Mergers Matter? ArXiv e-prints.
- HOPKINS, P. F., BUNDY, K., CROTON, D., ET AL. : 2010a. Mergers and Bulge Formation in  $\Lambda$ CDM: Which Mergers Matter? ApJ, **715**, 202–229.
- HOPKINS, P. F., BUNDY, K., HERNQUIST, L., ET AL. : 2010b. Discriminating between the physical processes that drive spheroid size evolution. MNRAS, **401**, 1099–1117.

- HOPKINS, P. F., BUNDY, K., MURRAY, N., ET AL. : 2009b. Compact high-redshift galaxies are the cores of the most massive present-day spheroids. *MNRAS*, **398**, 898–910.
- HOPKINS, P. F., HERNQUIST, L., COX, T. J., ET AL. : 2009c. Dissipation and Extra Light in Galactic Nuclei. IV. Evolution in the Scaling Relations of Spheroids. *ApJ*, **691**, 1424–1458.
- HOPKINS, P. F., QUATAERT, E., MURRAY, N.: 2011. Self-Regulated Star Formation in Galaxies via Momentum Input from Massive Stars. *ArXiv e-prints*.
- HYDE, J. B. BERNARDI, M.: 2009. Curvature in the scaling relations of early-type galaxies. *MNRAS*, **394**, 1978–1990.
- JENKINS, A.: 2010. Second-order Lagrangian perturbation theory initial conditions for resimulations. *MNRAS*, **403**, 1859–1872.
- JESSEIT, R., CAPPELLARI, M., NAAB, T., ET AL. : 2009. Specific angular momentum of disc merger remnants and the  $\lambda_R$ -parameter. *MNRAS*, **397**, 1202–1214.
- JESSEIT, R., NAAB, T., BURKERT, A.: 2002. The Validity of the Adiabatic Contraction Approximation for Dark Matter Halos. *ApJ*, **571**, L89–L92.
- JESSEIT, R., NAAB, T., PELETIER, R. F., ET AL. : 2007. 2D kinematics of simulated disc merger remnants. *MNRAS*, **376**, 997–1020.
- JOGEE, S., MILLER, S. H., PENNER, K., ET AL. : 2009. History of Galaxy Interactions and Their Impact on Star Formation Over the Last 7 Gyr from GEMS. *ApJ*, **697**, 1971–1992.
- JOHANSSON, P. H. EFSTATHIOU, G.: 2006. A model for the metallicity evolution of damped Lyman  $\alpha$  systems. *MNRAS*, **371**, 1519–1535.
- JOHANSSON, P. H., NAAB, T., BURKERT, A.: 2009a. Equal- and Unequal-Mass Mergers of Disk and Elliptical Galaxies with Black Holes. *ApJ*, **690**, 802–821.
- JOHANSSON, P. H., NAAB, T., OSTRIKER, J. P.: 2009b. Gravitational Heating Helps Make Massive Galaxies Red and Dead. *ApJ*, **697**, L38–L43.
- JOUNG, M. R., CEN, R., BRYAN, G. L.: 2009. Galaxy Size Problem at  $z = 3$ : Simulated Galaxies are too Small. *ApJ*, **692**, L1–L4.
- JUNEAU, S., GLAZEBROOK, K., CRAMPTON, D., ET AL. : 2005. Cosmic Star Formation History and Its Dependence on Galaxy Stellar Mass. *ApJ*, **619**, L135–L138.
- KATZ, N., WEINBERG, D. H., HERNQUIST, L.: 1996. Cosmological Simulations with TreeSPH. *ApJS*, **105**, 19.

- KAUFFMANN, G.: 1996. The age of elliptical galaxies and bulges in a merger model. MNRAS, **281**, 487–492.
- KAUFFMANN, G., COLBERG, J. M., DIAFERIO, A., ET AL. : 1999. Clustering of galaxies in a hierarchical universe - I. Methods and results at  $z=0$ . MNRAS, **303**, 188–206.
- KAVIRAJ, S., TAN, K.-M., ELLIS, R. S., ET AL. : 2011. A coincidence of disturbed morphology and blue UV colour: minor-merger-driven star formation in early-type galaxies at  $z \sim 0.6$ . MNRAS, **411**, 2148–2160.
- KENNICUTT, R. C.: 1998. The Global Schmidt Law in Star-forming Galaxies. ApJ, **498**, 541.
- KEREŠ, D., KATZ, N., DAVÉ, R., ET AL. : 2009a. Galaxies in a simulated  $\Lambda$ CDM universe - II. Observable properties and constraints on feedback. MNRAS, **396**, 2332–2344.
- KEREŠ, D., KATZ, N., FARDAL, M., ET AL. : 2009b. Galaxies in a simulated  $\Lambda$ CDM Universe - I. Cold mode and hot cores. MNRAS, **395**, 160–179.
- KEREŠ, D., KATZ, N., WEINBERG, D. H., ET AL. : 2005. How do galaxies get their gas? MNRAS, **363**, 2–28.
- KHOCHFAR, S. BURKERT, A.: 2003. The Importance of Spheroidal and Mixed Mergers for Early-Type Galaxy Formation. ApJ, **597**, L117–L120.
- KHOCHFAR, S. BURKERT, A.: 2006. Orbital parameters of merging dark matter halos. A&A, **445**, 403–412.
- KHOCHFAR, S., EMSELLEM, E., SERRA, P., ET AL. : 2011. The ATLAS<sup>3D</sup> project - VIII. Modelling the formation and evolution of fast and slow rotator early-type galaxies within  $\Lambda$ CDM. MNRAS, **417**, 845–862.
- KHOCHFAR, S. Ostriker, J. P.: 2008. Adding Environmental Gas Physics to the Semianalytic Method for Galaxy Formation: Gravitational Heating. ApJ, **680**, 54–69.
- KHOCHFAR, S. SILK, J.: 2006a. A Simple Model for the Size Evolution of Elliptical Galaxies. ApJ, **648**, L21–L24.
- KHOCHFAR, S. SILK, J.: 2006b. On the origin of stars in bulges and elliptical galaxies. MNRAS, **370**, 902–910.
- KHOCHFAR, S. SILK, J.: 2009. Dry mergers: a crucial test for galaxy formation. MNRAS, **397**, 506–510.

- KHOKHLOV, A.: 1998. Fully Threaded Tree Algorithms for Adaptive Refinement Fluid Dynamics Simulations. Journal of Computational Physics, **143**, 519–543.
- KOMATSU, E., SMITH, K. M., DUNKLEY, J., ET AL. : 2010. Seven-Year Wilkinson Microwave Anisotropy Probe (WMAP) Observations: Cosmological Interpretation. ArXiv e-prints.
- KOMATSU, E., SMITH, K. M., DUNKLEY, J., ET AL. : 2011. Seven-year Wilkinson Microwave Anisotropy Probe (WMAP) Observations: Cosmological Interpretation. ApJS, **192**, 18.
- KORMENDY, J., FISHER, D. B., CORNELL, M. E., ET AL. : 2009. Structure and Formation of Elliptical and Spheroidal Galaxies. ApJS, **182**, 216–309.
- KRAJNOVIĆ, D., BACON, R., CAPPELLARI, M., ET AL. : 2008. The SAURON project - XII. Kinematic substructures in early-type galaxies: evidence for discs in fast rotators. MNRAS, **390**, 93–117.
- KRAJNOVIĆ, D., EMSELLEM, E., CAPPELLARI, M., ET AL. : 2011. The ATLAS<sup>3D</sup> project - II. Morphologies, kinematic features and alignment between photometric and kinematic axes of early-type galaxies. MNRAS, **414**, 2923–2949.
- KRIEK, M., VAN DER WEL, A., VAN DOKKUM, P. G., ET AL. : 2008. The Detection of a Red Sequence of Massive Field Galaxies at  $z \sim 2.3$  and Its Evolution to  $z \sim 0$ . ApJ, **682**, 896–906.
- KRIEK, M., VAN DOKKUM, P. G., FRANX, M., ET AL. : 2006. Spectroscopic Identification of Massive Galaxies at  $z \sim 2.3$  with Strongly Suppressed Star Formation. ApJ, **649**, L71–L74.
- LACKNER, C. N. Ostriker, J. P.: 2010. Dissipational Versus Dissipationless Galaxy Formation and the Dark Matter Content of Galaxies. ApJ, **712**, 88–100.
- LARSON, R. B.: 1969. A model for the formation of a spherical galaxy. MNRAS, **145**, 405.
- LARSON, R. B.: 1974. Effects of supernovae on the early evolution of galaxies. MNRAS, **169**, 229–246.
- LARSON, R. B.: 1975. Models for the formation of elliptical galaxies. MNRAS, **173**, 671–699.
- LEAUTHAUD, A., TINKER, J., BEHROOZI, P. S., ET AL. : 2011. A Theoretical Framework for Combining Techniques that Probe the Link Between Galaxies and Dark Matter. ApJ, **738**, 45.
- Longair, M. S., editor: 1998. Galaxy formation.

- LONGHETTI, M., SARACCO, P., SEVERGNINI, P., ET AL. : 2007. The Kormendy relation of massive elliptical galaxies at  $z \sim 1.5$ : evidence for size evolution. MNRAS, **374**, 614–626.
- LOTZ, J. M., JONSSON, P., COX, T. J., ET AL. : 2011. The Major and Minor Galaxy Merger Rates at  $z < 1.5$ . ArXiv e-prints, arxiv: 1108.2508.
- LUCY, L. B.: 1977. A numerical approach to the testing of the fission hypothesis. AJ, **82**, 1013–1024.
- MAGORRIAN, J. BINNEY, J.: 1994. Predicting line-of-sight velocity distributions of elliptical galaxies. MNRAS, **271**, 949.
- MAKINO, J.: 1990. Comparison of Two Different Tree Algorithms. Journal of Computational Physics, **88**, 393.
- MAKINO, J. HUT, P.: 1997. Merger Rate of Equal-Mass Spherical Galaxies. ApJ, **481**, 83.
- MANDELBAUM, R., SELJAK, U., KAUFFMANN, G., ET AL. : 2006. Galaxy halo masses and satellite fractions from galaxy-galaxy lensing in the Sloan Digital Sky Survey: stellar mass, luminosity, morphology and environment dependencies. MNRAS, **368**, 715–731.
- MARCHESINI, D., VAN DOKKUM, P. G., FÖRSTER SCHREIBER, N. M., ET AL. : 2009. The Evolution of the Stellar Mass Function of Galaxies from  $z = 4.0$  and the First Comprehensive Analysis of its Uncertainties: Evidence for Mass-Dependent Evolution. ApJ, **701**, 1765–1796.
- MARTINEZ-MANSO, J., GUZMAN, R., BARRO, G., ET AL. : 2011. Velocity Dispersions and Stellar Populations of the Most Compact and Massive Early-type Galaxies at Redshift  $\sim 1$ . ApJ, **738**, L22+.
- MCCARTHY, I. G., SCHAYE, J., PONMAN, T. J., ET AL. : 2010a. The case for AGN feedback in galaxy groups. MNRAS, arxiv:n 740+.
- MCCARTHY, I. G., SCHAYE, J., PONMAN, T. J., ET AL. : 2010b. The case for AGN feedback in galaxy groups. MNRAS, **406**, 822–839.
- MCKEE, C. F. OSTRIKER, J. P.: 1977. A theory of the interstellar medium - Three components regulated by supernova explosions in an inhomogeneous substrate. ApJ, **218**, 148–169.
- MERRITT, D.: 1996. Optimal Smoothing for N-Body Codes. AJ, **111**, 2462.
- MEZA, A., NAVARRO, J. F., ABADI, M. G., ET AL. : 2005. Accretion relics in the solar neighbourhood: debris from  $\omega$ Cen’s parent galaxy. MNRAS, **359**, 93–103.

- MEZA, A., NAVARRO, J. F., STEINMETZ, M., ET AL. : 2003. Simulations of Galaxy Formation in a  $\Lambda$ CDM Universe. III. The Dissipative Formation of an Elliptical Galaxy. *ApJ*, **590**, 619–635.
- MO, H., VAN DEN BOSCH, F. C., WHITE, S.: 2010. Galaxy Formation and Evolution.
- MONAGHAN, J. J.: 1992. Smoothed particle hydrodynamics. *ARA&A*, **30**, 543–574.
- MONAGHAN, J. J.: 1997. SPH and Riemann Solvers. *Journal of Computational Physics*, **136**, 298–307.
- MONAGHAN, J. J. LATTANZIO, J. C.: 1985. A refined particle method for astrophysical problems. *A&A*, **149**, 135–143.
- MOSLEH, M., WILLIAMS, R. J., FRANX, M., ET AL. : 2011. The Evolution of the Mass-Size Relation to  $z = 3.5$  for UV-bright Galaxies and Submillimeter Galaxies in the GOODS-North Field. *ApJ*, **727**, 5–+.
- MOSTER, B. P., SOMERVILLE, R. S., MAULBETSCH, C., ET AL. : 2010. Constraints on the Relationship between Stellar Mass and Halo Mass at Low and High Redshift. *ApJ*, **710**, 903–923.
- NAAB, T., JOHANSSON, P. H., OSTRICKER, J. P.: 2009. Minor Mergers and the Size Evolution of Elliptical Galaxies. *ApJ*, **699**, L178–L182.
- NAAB, T., JOHANSSON, P. H., OSTRICKER, J. P., ET AL. : 2007. Formation of Early-Type Galaxies from Cosmological Initial Conditions. *ApJ*, **658**, 710–720.
- NAAB, T., KHOCHFAR, S., BURKERT, A.: 2006. Properties of Early-Type, Dry Galaxy Mergers and the Origin of Massive Elliptical Galaxies. *ApJ*, **636**, L81–L84.
- NAAB, T. OSTRICKER, J. P.: 2009. Are Disk Galaxies the Progenitors of Giant Ellipticals? *ApJ*, **690**, 1452–1462.
- NAGAMINE, K., CEN, R., HERNQUIST, L., ET AL. : 2005. Massive Galaxies and Extremely Red Objects at  $z = 1-3$  in Cosmological Hydrodynamic Simulations: Near-Infrared Properties. *ApJ*, **627**, 608–620.
- NAGAMINE, K., OSTRICKER, J. P., FUKUGITA, M., ET AL. : 2006. The History of Cosmological Star Formation: Three Independent Approaches and a Critical Test Using the Extragalactic Background Light. *ApJ*, **653**, 881–893.
- NAVARRO, J. F., FRENK, C. S., WHITE, S. D. M.: 1997. A Universal Density Profile from Hierarchical Clustering. *ApJ*, **490**, 493–+.
- NEGROPONTE, J. WHITE, S. D. M.: 1983. Simulations of mergers between disc-halo galaxies. *MNRAS*, **205**, 1009–1029.

- NEISTEIN, E., LI, C., KHOCHFAR, S., ET AL. : 2011. A tale of two populations: the stellar mass of central and satellite galaxies. *MNRAS*, **416**, 1486–1499.
- NELAN, J. E., SMITH, R. J., HUDSON, M. J., ET AL. : 2005. NOAO Fundamental Plane Survey. II. Age and Metallicity along the Red Sequence from Line-Strength Data. *ApJ*, **632**, 137–156.
- NEWMAN, A. B., ELLIS, R. S., TREU, T., ET AL. : 2010. Keck Spectroscopy of  $z > 1$  Field Spheroidals: Dynamical Constraints on the Growth Rate of Red "Nuggets". *ApJ*, **717**, L103–L107.
- NIPOTI, C., LONDRILLO, P., CIOTTI, L.: 2003. Galaxy merging, the fundamental plane of elliptical galaxies and the  $M_{BH}-\sigma_0$  relation. *MNRAS*, **342**, 501–512.
- NIPOTI, C., TREU, T., AUGER, M. W., ET AL. : 2009a. Can Dry Merging Explain the Size Evolution of Early-Type Galaxies? *ApJ*, **706**, L86–L90.
- NIPOTI, C., TREU, T., BOLTON, A. S.: 2009b. Dry Mergers and the Formation of Early-Type Galaxies: Constraints from Lensing and Dynamics. *ApJ*, **703**, 1531–1544.
- OPPENHEIMER, B. D. DAVÉ, R.: 2006. Cosmological simulations of intergalactic medium enrichment from galactic outflows. *MNRAS*, **373**, 1265–1292.
- OPPENHEIMER, B. D. DAVÉ, R.: 2008. Mass, metal, and energy feedback in cosmological simulations. *MNRAS*, **387**, 577–600.
- OPPENHEIMER, B. D., DAVÉ, R., KEREŠ, D., ET AL. : 2010a. Feedback and recycled wind accretion: assembling the  $z = 0$  galaxy mass function. *MNRAS*, arxiv:n 860–+.
- OPPENHEIMER, B. D., DAVÉ, R., KEREŠ, D., ET AL. : 2010b. Feedback and recycled wind accretion: assembling the  $z = 0$  galaxy mass function. *MNRAS*, **406**, 2325–2338.
- OSER, L., NAAB, T., OSTRIKER, J. P., ET AL. : 2012. The Cosmological Size and Velocity Dispersion Evolution of Massive Early-type Galaxies. *ApJ*, **744**, 63.
- OSER, L., OSTRIKER, J. P., NAAB, T., ET AL. : 2010. The Two Phases of Galaxy Formation. *ApJ*, **725**, 2312–2323.
- OSTRIKER, J. P., CHOI, E., CIOTTI, L., ET AL. : 2010. Momentum Driving: Which Physical Processes Dominate Active Galactic Nucleus Feedback? *ApJ*, **722**, 642–652.
- PADMANABHAN, T.: 2000. Theoretical Astrophysics - Volume 1, Astrophysical Processes.

- PARTRIDGE, R. B. PEEBLES, P. J. E.: 1967. Are Young Galaxies Visible? ApJ, **147**, 868.
- PEACOCK, J. A.: 1999. Cosmological Physics.
- PERLMUTTER, S., ALDERING, G., GOLDHABER, G., ET AL. : 1999. Measurements of Omega and Lambda from 42 High-Redshift Supernovae. ApJ, **517**, 565–586.
- PETKOVA, M. SPRINGEL, V.: 2009. An implementation of radiative transfer in the cosmological simulation code GADGET. MNRAS, **396**, 1383–1403.
- PETTINI, M., SHAPLEY, A. E., STEIDEL, C. C., ET AL. : 2001. The Rest-Frame Optical Spectra of Lyman Break Galaxies: Star Formation, Extinction, Abundances, and Kinematics. ApJ, **554**, 981–1000.
- PIONTEK, F. STEINMETZ, M.: 2009. The Modelling of Feedback Processes in Cosmological Simulations of Disk Galaxy Formation. ArXiv e-prints.
- PIONTEK, F. STEINMETZ, M.: 2011. The modelling of feedback processes in cosmological simulations of disc galaxy formation. MNRAS, **410**, 2625–2642.
- POWER, C., NAVARRO, J. F., JENKINS, A., ET AL. : 2003. The inner structure of  $\Lambda$ CDM haloes - I. A numerical convergence study. MNRAS, **338**, 14–34.
- PUCHWEIN, E., SPRINGEL, V., SIJACKI, D., ET AL. : 2010. Intracluster stars in simulations with active galactic nucleus feedback. MNRAS, **406**, 936–951.
- QUINN, T., KATZ, N., STADEL, J., ET AL. : 1997. Time stepping N-body simulations. ArXiv Astrophysics e-prints.
- RICCIARDELLI, E., TRUJILLO, I., BUITRAGO, F., ET AL. : 2010. The evolutionary sequence of submillimetre galaxies: from diffuse discs to massive compact ellipticals? MNRAS, **406**, 230–236.
- RIESS, A. G., FILIPPENKO, A. V., CHALLIS, P., ET AL. : 1998. Observational Evidence from Supernovae for an Accelerating Universe and a Cosmological Constant. AJ, **116**, 1009–1038.
- RYAN, JR., R. E., MCCARTHY, P. J., COHEN, S. H., YAN, H., ET AL. : 2010. The Size Evolution of Passive Galaxies: Observations from the Wide Field Camera 3 Early Release Science Program. ArXiv e-prints.
- SAGLIA, R. P., SÁNCHEZ-BLÁZQUEZ, P., BENDER, R., ET AL. : 2010. The fundamental plane of EDisCS galaxies. The effect of size evolution. A&A, **524**, A6+.
- SALES, L. V., NAVARRO, J. F., SCHAYE, J., ET AL. : 2010. Feedback and the structure of simulated galaxies at redshift  $z=2$ . MNRAS, **409**, 1541–1556.

- SALPETER, E. E.: 1955. The Luminosity Function and Stellar Evolution. ApJ, **121**, 161.
- SARACCO, P., LONGHETTI, M., ANDREON, S.: 2009. The population of early-type galaxies at  $1 < z < 2$  - new clues on their formation and evolution. MNRAS, **392**, 718–732.
- SAWALA, T., SCANNAPIECO, C., MAIO, U., ET AL. : 2010. Formation of isolated dwarf galaxies with feedback. MNRAS, **402**, 1599–1613.
- SAZONOV, S. Y., OSTRIKER, J. P., SUNYAEV, R. A.: 2004. Quasars: the characteristic spectrum and the induced radiative heating. MNRAS, **347**, 144–156.
- SCANNAPIECO, C., TISSERA, P. B., WHITE, S. D. M., ET AL. : 2008. Effects of supernova feedback on the formation of galaxy discs. MNRAS, **389**, 1137–1149.
- SCANNAPIECO, C., WHITE, S. D. M., SPRINGEL, V., ET AL. : 2009. The formation and survival of discs in a  $\Lambda$ CDM universe. MNRAS, **396**, 696–708.
- SCANNAPIECO, C., WHITE, S. D. M., SPRINGEL, V., ET AL. : 2011. Formation history, structure and dynamics of discs and spheroids in simulated Milky Way mass galaxies. MNRAS, **417**, 154–171.
- SCHAYE, J., DALLA VECCHIA, C., BOOTH, C. M., ET AL. : 2009. The physics driving the cosmic star formation history. ArXiv e-prints.
- SCHAYE, J., DALLA VECCHIA, C., BOOTH, C. M., ET AL. : 2010. The physics driving the cosmic star formation history. MNRAS, **402**, 1536–1560.
- SEARLE, L., SARGENT, W. L. W., BAGNUOLO, W. G.: 1973. The History of Star Formation and the Colors of Late-Type Galaxies. ApJ, **179**, 427–438.
- SHANKAR, F., LAPI, A., SALUCCI, P., ET AL. : 2006. New Relationships between Galaxy Properties and Host Halo Mass, and the Role of Feedbacks in Galaxy Formation. ApJ, **643**, 14–25.
- SHANKAR, F., MARULLI, F., BERNARDI, M., ET AL. : 2010a. Further constraining galaxy evolution models through the size function of SDSS early-type galaxies. MNRAS, **405**, 948–960.
- SHANKAR, F., MARULLI, F., BERNARDI, M., ET AL. : 2010b. Sizes and ages of SDSS ellipticals: comparison with hierarchical galaxy formation models. MNRAS, **403**, 117–128.
- SHANKAR, F., MARULLI, F., BERNARDI, M., ET AL. : 2011. Size Evolution of Spheroids in a Hierarchical Universe. ArXiv e-prints, arxiv: 1105.6043.

- SHETH, R. K., MO, H. J., TORMEN, G.: 2001. Ellipsoidal collapse and an improved model for the number and spatial distribution of dark matter haloes. *MNRAS*, **323**, 1–12.
- SIJACKI, D., SPRINGEL, V., HAEHNELT, M. G.: 2009. Growing the first bright quasars in cosmological simulations of structure formation. *MNRAS*, **400**, 100–122.
- SOMERVILLE, R. S. PRIMACK, J. R.: 1999. Semi-analytic modelling of galaxy formation: the local Universe. *MNRAS*, **310**, 1087–1110.
- SOMMER-LARSEN, J., GÖTZ, M., PORTINARI, L.: 2003. Galaxy Formation: Cold Dark Matter, Feedback, and the Hubble Sequence. *ApJ*, **596**, 47–66.
- SPERGEL, D. N., BEAN, R., DORÉ, O., ET AL. : 2007. Three-Year Wilkinson Microwave Anisotropy Probe (WMAP) Observations: Implications for Cosmology. *ApJS*, **170**, 377–408.
- SPERGEL, D. N., VERDE, L., PEIRIS, H. V., ET AL. : 2003. First-Year Wilkinson Microwave Anisotropy Probe (WMAP) Observations: Determination of Cosmological Parameters. *ApJS*, **148**, 175–194.
- SPRINGEL, V.: 2005. The cosmological simulation code GADGET-2. *MNRAS*, **364**, 1105–1134.
- SPRINGEL, V., DI MATTEO, T., HERNQUIST, L.: 2005a. Black Holes in Galaxy Mergers: The Formation of Red Elliptical Galaxies. *ApJ*, **620**, L79–L82.
- SPRINGEL, V. HERNQUIST, L.: 2002. Cosmological smoothed particle hydrodynamics simulations: the entropy equation. *MNRAS*, **333**, 649–664.
- SPRINGEL, V. HERNQUIST, L.: 2003. Cosmological smoothed particle hydrodynamics simulations: a hybrid multiphase model for star formation. *MNRAS*, **339**, 289–311.
- SPRINGEL, V., WHITE, S. D. M., JENKINS, A., ET AL. : 2005b. Simulations of the formation, evolution and clustering of galaxies and quasars. *Nature*, **435**, 629–636.
- STEIDEL, C. C., ADELBERGER, K. L., GIAVALISCO, M., ET AL. : 1999. Lyman-Break Galaxies at  $z > \sim 4$  and the Evolution of the Ultraviolet Luminosity Density at High Redshift. *ApJ*, **519**, 1–17.
- STEIDEL, C. C., ERB, D. K., SHAPLEY, A. E., ET AL. : 2010. The Structure and Kinematics of the Circumgalactic Medium from Far-ultraviolet Spectra of  $z \sim 2$ –3 Galaxies. *ApJ*, **717**, 289–322.
- STEINMETZ, M.: 1996. GRAPESPH: cosmological smoothed particle hydrodynamics simulations with the special-purpose hardware GRAPE. *MNRAS*, **278**, 1005–1017.

- SZOMORU, D., FRANX, M., VAN DOKKUM, P. G., ET AL. : 2010. Confirmation of the Compactness of a  $z = 1.91$  Quiescent Galaxy with Hubble Space Telescope's Wide Field Camera 3. ApJ, **714**, L244–L248.
- TAYLOR, E. N., FRANX, M., GLAZEBROOK, K., ET AL. : 2010. On the Dearth of Compact, Massive, Red Sequence Galaxies in the Local Universe. ApJ, **720**, 723–741.
- TEYSSIER, R., MOORE, B., MARTIZZI, D., ET AL. : 2011. Mass distribution in galaxy clusters: the role of Active Galactic Nuclei feedback. MNRAS, **414**, 195–208.
- THOMAS, D., MARASTON, C., BENDER, R., ET AL. : 2005. The Epochs of Early-Type Galaxy Formation as a Function of Environment. ApJ, **621**, 673–694.
- TIRET, O., SALUCCI, P., BERNARDI, M., ET AL. : 2011. The inner structure of very massive elliptical galaxies: implications for the inside-out formation mechanism of  $z \sim 2$  galaxies. MNRAS, **411**, 1435–1444.
- TOFT, S., VAN DOKKUM, P., FRANX, M., ET AL. : 2007. Hubble Space Telescope and Spitzer Imaging of Red and Blue Galaxies at  $z \sim 2.5$ : A Correlation between Size and Star Formation Activity from Compact Quiescent Galaxies to Extended Star-forming Galaxies. ApJ, **671**, 285–302.
- TOOMRE, A.: 1974. Gravitational Interactions Between Galaxies (invited Paper). In IAU Symp. 58: The Formation and Dynamics of Galaxies, arxiv: 347.
- TOOMRE, A.: 1977. Mergers and Some Consequences. In Evolution of Galaxies and Stellar Populations, arxiv: 401.
- TOOMRE, A. TOOMRE, J.: 1972. Galactic Bridges and Tails. ApJ, **178**, 623–666.
- TRUJILLO, I., CENARRO, A. J., DE LORENZO-CÁCERES, A., ET AL. : 2009. Super-dense Massive Galaxies in the Nearby Universe. ApJ, **692**, L118–L122.
- TRUJILLO, I., CONSELICE, C. J., BUNDY, K., ET AL. : 2007. Strong size evolution of the most massive galaxies since  $z \sim 2$ . MNRAS, **382**, 109–120.
- TRUJILLO, I., FERRERAS, I., DE LA ROSA, I. G.: 2011. Dissecting the size evolution of elliptical galaxies since  $z \sim 1$ : puffing-up versus minor-merging scenarios. MNRAS, **415**, 3903–3913.
- TRUJILLO, I., FÖRSTER SCHREIBER, N. M., RUDNICK, G., ET AL. : 2006. The Size Evolution of Galaxies since  $z \sim 3$ : Combining SDSS, GEMS, and FIRES. ApJ, **650**, 18–41.

- VAN DE SANDE, J., KRIEK, M., FRANX, M., ET AL. : 2011. The Stellar Velocity Dispersion of a Compact Massive Galaxy at  $z = 1.80$  Using X-Shooter: Confirmation of the Evolution in the Mass-Size and Mass-Dispersion Relations. *ApJ*, **736**, L9+.
- VAN DE VEN, G., VAN DEN BOSCH, R. C. E., VEROLME, E. K., ET AL. : 2006. The dynamical distance and intrinsic structure of the globular cluster  $\omega$  Centauri. *A&A*, **445**, 513–543.
- VAN DER MAREL, R. P. FRANX, M.: 1993. A new method for the identification of non-Gaussian line profiles in elliptical galaxies. *ApJ*, **407**, 525–539.
- VAN DER WEL, A., BELL, E. F., VAN DEN BOSCH, F. C., ET AL. : 2009. On the Size and Comoving Mass Density Evolution of Early-Type Galaxies. *ApJ*, **698**, 1232–1243.
- VAN DER WEL, A., FRANX, M., VAN DOKKUM, P. G., ET AL. : 2005. Mass-to-Light Ratios of Field Early-Type Galaxies at  $z \sim 1$  from Ultradeep Spectroscopy: Evidence for Mass-dependent Evolution. *ApJ*, **631**, 145–162.
- VAN DER WEL, A., HOLDEN, B. P., ZIRM, A. W., ET AL. : 2008. Recent Structural Evolution of Early-Type Galaxies: Size Growth from  $z = 1$  to  $z = 0$ . *ApJ*, **688**, 48–58.
- VAN DER WEL, A., RIX, H.-W., WUYTS, S., ET AL. : 2011. The Majority of Compact Massive Galaxies at  $z \sim 2$  are Disk Dominated. *ApJ*, **730**, 38+.
- VAN DOKKUM, P. G. BRAMMER, G.: 2010. Hubble Space Telescope WFC3 Grism Spectroscopy and Imaging of a Growing Compact Galaxy at  $z = 1.9$ . *ApJ*, **718**, L73–L77.
- VAN DOKKUM, P. G. CONROY, C.: 2010. A substantial population of low-mass stars in luminous elliptical galaxies. *Nature*, **468**, 940–942.
- VAN DOKKUM, P. G., FRANX, M., KRIEK, M., ET AL. : 2008. Confirmation of the Remarkable Compactness of Massive Quiescent Galaxies at  $z \sim 2.3$ : Early-Type Galaxies Did not Form in a Simple Monolithic Collapse. *ApJ*, **677**, L5–L8.
- VAN DOKKUM, P. G., KRIEK, M., FRANX, M.: 2009. A high stellar velocity dispersion for a compact massive galaxy at redshift  $z = 2.186$ . *Nature*, **460**, 717–719.
- VAN DOKKUM, P. G., QUADRI, R., MARCHESINI, D., ET AL. : 2006. The Space Density and Colors of Massive Galaxies at  $2 < z < 3$ : The Predominance of Distant Red Galaxies. *ApJ*, **638**, L59–L62.
- VAN DOKKUM, P. G., WHITAKER, K. E., BRAMMER, G., ET AL. : 2010. The Growth of Massive Galaxies Since  $z = 2$ . *ApJ*, **709**, 1018–1041.

- VITVITSKA, M., KLYPIN, A. A., KRAVTSOV, A. V., ET AL. : 2002. The Origin of Angular Momentum in Dark Matter Halos. ApJ, **581**, 799–809.
- WEINZIRL, T., JOGEE, S., CONSELICE, C. J., ET AL. : 2011. Insights on the Formation, Evolution, and Activity of Massive Galaxies From Ultra-Compact and Disky Galaxies at  $z=2-3$ . ArXiv e-prints, arxiv: 1107.2591.
- WHITE, S. D. M.: 1978. Simulations of merging galaxies. MNRAS, **184**, 185–203.
- WHITE, S. D. M.: 1979a. Can mergers make slowly rotating elliptical galaxies. ApJ, **229**, L9–L13.
- WHITE, S. D. M.: 1979b. Further simulations of merging galaxies. MNRAS, **189**, 831–852.
- WHITE, S. D. M.: 1980. Mixing processes in galaxy mergers. MNRAS, **191**, 1P–4P.
- WHITE, S. D. M. REES, M. J.: 1978. Core condensation in heavy halos - A two-stage theory for galaxy formation and clustering. MNRAS, **183**, 341–358.
- WIERSMA, R. P. C., SCHAYE, J., DALLA VECCHIA, C., ET AL. : 2010a. The enrichment history of cosmic metals. ArXiv e-prints.
- WIERSMA, R. P. C., SCHAYE, J., DALLA VECCHIA, C., ET AL. : 2010b. The enrichment history of cosmic metals. MNRAS, **409**, 132–144.
- WILLIAMS, R. E., BLACKER, B., DICKINSON, M., ET AL. : 1996. The Hubble Deep Field: Observations, Data Reduction, and Galaxy Photometry. AJ, **112**, 1335.
- WILLIAMS, R. J., QUADRI, R. F., FRANX, M., ET AL. : 2009. Detection of Quiescent Galaxies in a Bicolor Sequence from  $Z = 0-2$ . ApJ, **691**, 1879–1895.
- WILLIAMS, R. J., QUADRI, R. F., FRANX, M., ET AL. : 2010. The Evolving Relations Between Size, Mass, Surface Density, and Star Formation in  $3 \times 10^4$  Galaxies Since  $z = 2$ . ApJ, **713**, 738–750.
- WUYTS, S., COX, T. J., HAYWARD, C. C., ET AL. : 2010. On Sizes, Kinematics, M/L Gradients, and Light Profiles of Massive Compact Galaxies at  $z \sim 2$ . ApJ, **722**, 1666–1684.
- YORK, D. G., ADELMAN, J., ANDERSON, JR., ET AL. : 2000. The Sloan Digital Sky Survey: Technical Summary. AJ, **120**, 1579–1587.
- YOUNG, L. M., BUREAU, M., DAVIS, T. A., ET AL. : 2011. The ATLAS<sup>3D</sup> project - IV. The molecular gas content of early-type galaxies. MNRAS, **414**, 940–967.
- ZEL'DOVICH, Y. B.: 1970. Gravitational instability: An approximate theory for large density perturbations. A&A, **5**, 84–89.

- ZIRM, A. W., VAN DER WEL, A., FRANX, M., ET AL. : 2007. NICMOS Imaging of DRGs in the HDF-S: A Relation between Star Formation and Size at  $z \sim 2.5$ . ApJ, **656**, 66–72.
- ZOLOTOV, A., WILLMAN, B., BROOKS, A. M., ET AL. : 2010. The Dual Origin of Stellar Halos. II. Chemical Abundances as Tracers of Formation History. ApJ, **721**, 738–743.

## Acknowledgements

### Ich danke...

- an erster Stelle meinem Doktorvater, **Prof. Dr. Andreas Burkert**, für die Möglichkeit an der Universitätssternwarte in München promovieren zu können...
- **Dr. Thorsten Naab**, für die intensive Begleitung dieser Arbeit - so wie auch schon meiner Diplomarbeit. Er ist verantwortlich für die guten Teile dieser Arbeit.
- **Prof. Jerry P. Ostriker**, für seine Geduld wann immer ich seinen Gedankengängen nicht auf Anhieb folgen konnte.
- **Dr. Peter H. Johansson**, für den es wirklich keine dummen Fragen gibt, und mir so manchen Sachverhalt ausführlichst erklärt hat.
- **Prof. Simon D. M. White**, der es mir ermöglicht hat meine Promotion am MPA beenden zu können.
- der **CAST** Gruppe an der USM.
- den **Systemadministratoren**, im Besonderen **Dr. Tadziu Hoffmann**.
- Meinen Mitstreitern, allen voran **Simon und Michi** die mich seit dem ersten Semester begleiten. Aber auch **Micha, Steffi, Steffi, Mathias und Hanna**. Mit Euch hat das Arbeiten - und auch das Nicht-Arbeiten - immer sehr viel Spaß gemacht!
- und nicht zuletzt meinen **Eltern**, für die Unterstützung während meiner gesamten Ausbildung und im Besonderen gegen Ende meiner Promotion.



## Ehrenwörtliche Versicherung und Erklärung

des Doktoranden

**Ludwig Oser**

Mit der Abgabe dieser Doktorarbeit versichere ich, dass ich die Arbeit selbständig verfasst und keine anderen als die angegebenen Quellen und Hilfsmittel benutzt habe.

*Ort, Datum*

*Unterschrift*